LORENTZ-VIOLATING DARK MATTER

A Dissertation

by

ANTONIO R. MONDRAGON

Submitted to the Office of Graduate Studies of
Texas A&M University
in partial fulfillment of the requirements for the degree of

DOCTOR OF PHILOSOPHY

May 2007

Major Subject: Physics

LORENTZ-VIOLATING DARK MATTER

A Dissertation

by

ANTONIO R. MONDRAGON

Submitted to the Office of Graduate Studies of
Texas A&M University
in partial fulfillment of the requirements for the degree of

DOCTOR OF PHILOSOPHY

Approved by:

Chair of Committee,	Roland E. Allen
Committee Members,	Richard L. Arnowitt
	Stephen A. Fulling
	James T. White
Head of Department,	Edward S. Fry

May 2007

Major Subject: Physics

ABSTRACT

Lorentz-Violating Dark Matter. (May 2007)
Antonio R. Mondragon, B.S., Northwestern State University of Louisiana;
M.S., Texas A&M University
Chair of Advisory Committee: Dr. Roland E. Allen

Observations from the 1930s until the present have established the existence of dark matter with an abundance that is much larger than that of luminous matter. Because none of the known particles of nature have the correct properties to be identified as the dark matter, various exotic candidates have been proposed. The neutralino of supersymmetric theories is the most promising example. Such cold dark matter candidates, however, lead to a conflict between the standard simulations of the evolution of cosmic structure and observations. Simulations predict excessive structure formation on small scales, including density cusps at the centers of galaxies, that is not observed. This conflict still persists in early 2007, and it has not yet been convincingly resolved by attempted explanations that invoke astrophysical phenomena, which would destroy or broaden all small scale structure. We have investigated another candidate that is perhaps more exotic: Lorentz-violating dark matter, which was originally motivated by an unconventional fundamental theory, but which in this dissertation is defined as matter which has a nonzero minimum velocity. Furthermore, the present investigation evolved into the broader goal of exploring the properties of Lorentz-violating matter and the astrophysical consequences – a subject which to our knowledge has not been previously studied. Our preliminary investigations indicated that this form of matter might have less tendency to form small-scale structure. These preliminary calculations certainly established that

Lorentz-violating matter which always moves at an appreciable fraction of the speed of light will bind less strongly. However, the much more thorough set of studies reported here lead to the conclusion that, although the binding energy is reduced, the small-scale structure problem is not solved by Lorentz-violating dark matter. On the other hand, when we compare the predictions of Lorentz-violating dynamics with those of classical special relativity and general relativity, we find that differences might be observable in the orbital motions of galaxies in a cluster. For example, galaxies – which are composed almost entirely of dark matter – observed to have enlarged orbits about the cluster center of mass may be an indication of Lorentz violation.

To my parents, Alex Leroy Mondragon and Beverly Deichmueller Mondragon.

ACKNOWLEDGMENTS

I would like to thank the following people and affiliated organizations for their support and for contributions to this work: Dr. Roland E. Allen, Center for Theoretical Physics, Texas A&M University; Dr. Robert Brick, Division of Natural Sciences, Blinn College; Dr. Harry D. Downing, Department of Physics and Astronomy, Stephen F. Austin State University.

TABLE OF CONTENTS

CHAPTER Page

LIST OF TABLES

LIST OF FIGURES

FIGURE Page

FIGURE Page

FIGURE Page

FIGURE Page

FIGURE Page

FIGURE Page

FIGURE Page

CHAPTER I

INTRODUCTION: OBSERVATIONAL COSMOLOGY

A. Historical Development of Modern Cosmology

The twentieth century marked a transformation in our understanding of the universe comparable in magnitude to the transformation inspired by Nicolaus Copernicus, Johannes Kepler, Gallileo Galilei, and Isaac Newton during and following the Renaissance. Because of improvements in astrometry, the vast scale of the universe was revealed during the first quarter century. The discovery of the Cepheid variable period-luminosity relation by Henrietta Leavitt [1] (1907) and subsequent (although erroneous) calibration using statistical parallax by Harlow Shapley [2] (1924) provided a rough determination of the distance to the Large Magellanic Cloud – increasing the known size of the universe to be at least hundreds of kiloparsecs. This step out of the Milky Way galaxy was to become known as the first rung of the *extragalactic distance scale*. The *Great Debate* (1920) concerning the proximity of the Andromeda and Triangulum "nebulae" was put to rest in 1925 when faint Cepheid variables in Andromeda were resolved using the Mt. Wilson 100-inch telescope. Edwin Hubble [3, 4] confirmed that the "spiral nebulae" were actually "island universes" much like our own Milky Way – increasing the size of the known universe further to millions of kiloparsecs, and extending the extragalactic distance scale. Albert Einstein considered the cosmological implications of his radical new theory of gravity [5], first adjusting the theory with a cosmological constant to achieve a static universe, and then yielding to the more natural prediction of an expanding universe, in agreement with the unexpected observation of the recession of distant galaxies by

---

The journal model is Nuclear Physics B.

Edwin Hubble [6, 7]. The Hubble expansion, together with accurate calculations of the relative abundances of the light elements in an expanding universe [8] by Ralph Alpher, Hans Bethe, and George Gamow (1948), and discovery of the microwave background radiation [9] by Arno Penzias and Robert Wilson (1965) firmly established a new paradigm and standard cosmological model.

The Hubble expansion, primordial nucleosynthesis, and cosmic background radiation served as a stable tripod for later observational programs to understand the history and nature of the universe. The four decades following Allan Sandage's optimistic announcement, "The Ability of the 200-inch [Hale] Telescope to Discriminate Between Selected World Models" [10] (1961), were dedicated to the exhaustive task of determining the extragalactic distance scale – the primary source of errors in all measurements of cosmological parameters. In 1965, due to limitations in ground-based astrometry, the Space Science Board of the U.S. National Academy of Sciences recommended that the National Aeronautics and Space Administration build a large space-based telescope. The first of these *Great Telescopes* – the *Hubble Space Telescope* – was not launched until 1990, with design flaws that were corrected a few years later. Lacking a precise measurement of the distance to the Large Magellanic Cloud, which contains the closest large group of Cepheids, and consequently lacking an accurate calibration of the period-luminosity relation, observational cosmology waited until the final decade of the twentieth century for precision space-based instruments to provide confidence in cosmological models.

At the same time, the fast-paced revolution in quantum devices during the last four decades of the twentieth century provided charged-coupled devices, expanding the capabilities of ground-based telescopes, as well as computers capable of simulating star clusters, galaxies, and even the large-scale structure of the universe. Larger telescopes enabled the observation of large numbers of star clusters, galaxies, and

galaxy clusters at great distances, inspiring new relationships and novel methods of distance determination. Infrared and radio astronomy led to the development of the Tully-Fisher relation [11] between rotational velocity and total luminosity of spiral galaxies. A simple relationship between the luminosity of elliptical galaxies and constituent stellar velocity dispersions was also discovered [12–14]. This was the era of painstaking refinement of distance *indicators*, during which the fundamental tools of observational cosmology were developed, and many new questions arose. Lengthy optical time exposures of nearby galaxy clusters were used to determine mass-to-light ratios, which were much higher than expected. Computer simulations and precision spectroscopy suggested that the oldest stars are older than the age of the universe as inferred from the Hubble constant, and that spiral galaxy formation required much more mass than is visible. The rotation curves of nearby galaxies confirmed that more matter (*dark matter*) must reside in the outer regions (*halos*) of galaxies. Distance indicators depend heavily on large samples, so that distances to nearby galaxies, due to their limited numbers, remained plagued with uncertainties. Although telescopes were bringing large-redshift objects into view, resolution was still limited by atmospheric effects. Trigonometric parallaxes for even the nearest extragalactic objects could not be measured. Accurate calibration of the distance indicators would have to wait for space-based instruments.

The successes of the *Cosmic Background Explorer* (1989), *Hubble Space Telescope* (1990), and *Hipparcos* (1989), however, instilled a new optimism in the ability to discriminate between cosmological models [15–19]. The space-based instruments produced accurate measurements of distances to high-redshift objects, providing confidence in determinations of cosmological parameters, and challenging the aesthetically pleasing and long enduring (1932–1990) Einstein-de Sitter model [20]. The age and mass density of the universe, as predicted by the Einstein-de Sitter model,

could not be reconciled with observations. Specifically, the ages of globular cluster stars disagreed with the Hubble age; and galaxy cluster masses – even including dark matter – did not add up to the critical mass. In addition, the assumptions of homogeneity, isotropy, and flatness were reinforced by data from the *Cosmic Background Explorer* – reviving interest in the cosmological constant. The unexpected discovery and independent verification of an accelerating expansion by the High-Z Supernova Search Team [21] and Supernovae Cosmology Project [22] in 1998 definitely demonstrated the need for a cosmological constant or some other form of "dark energy", and spawned the modern era of precision cosmology.

B. Conventional Cosmologies

Conventional cosmologies are based on the Einstein-Hilbert action – which yields Einstein's field equations – together with an inflationary scenario [23]. The generalization of the Einstein-de Sitter model [20, 24] to include an inflationary scenario ($\Omega_{\rm m} \simeq 1$, $\Lambda = 0$) can be regarded as an extension of the old *standard cosmology* [25]. Further generalizations are a variety of cold dark matter (CDM) models, including ΛCDM ($\Omega_{\rm m} < 1$, $\Lambda \neq 0$) [26, 27].

Central to all cosmological measurements is the extragalactic distance scale. All distance determinations beyond the galaxy are model dependent. The most fundamental assumptions are those of homogeneity and isotropy of the universe, of which a direct consequence is the Robertson-Walker metric:

$$\mathrm{d}s^2 = -\mathrm{d}t^2 + a(t)^2 \left(\frac{\mathrm{d}r^2}{1 - kr^2} + r^2 \mathrm{d}\Omega \right) \tag{1.1}$$

where $\mathrm{d}\Omega = \mathrm{d}\theta^2 + \sin^2\theta\,\mathrm{d}\phi^2$, $a(t)$ is the cosmic scale factor, and the geometry is specified by $k = 1\,(\text{spherical})$, $0\,(\text{flat})$, or $-1\,(\text{hyperbolic})$. This metric, together

with the dynamics of the cosmic scale factor as determined from the Einstein field equations, provides the canonical model for determining distances beyond our galaxy. The Hubble parameter, deceleration parameter, and redshift are defined in terms of the cosmic scale factor:

$$H_0 \equiv \frac{\dot{a}_0}{a_0}, \tag{1.2}$$

$$q_0 \equiv -\frac{\ddot{a}_0}{\dot{a}_0^2} a_0, \tag{1.3}$$

$$1 + z \equiv \frac{\lambda_0}{\lambda} = \frac{a_0}{a}, \tag{1.4}$$

where $a_0 \equiv a\,(t_0)$ is the present value of the cosmic scale factor, λ_0 is the detected wavelength, and λ is the emitted wavelength of light from extragalactic sources. The equality of the ratio of wavelengths to the ratio of cosmic scale factors assumes that the sources participate strictly in the Hubble flow.

C. Luminosity Distance

An essential bridge between theory and observation is the relation between redshift and luminosity distance. The luminosity distance, measured by comparison of apparent with absolute luminosity [25], is given by $d_{\rm L} = r_z a_0 (1+z)$, where r_z is the comoving radial coordinate at redshift z. Within the framework of conventional cosmologies the comoving radial coordinate satisfies [24, 28]

$$\int_0^{r_z} \frac{{\rm d}r}{\sqrt{1-kr}} = \frac{H_0^{-1}}{a_0} \int_0^{z} \frac{{\rm d}z'}{(1+z')\sqrt{\Omega_{\rm m}(1+z') + \Omega_\Lambda (1+z')^{-2} + 1 - (\Omega_{\rm m} + \Omega_\Lambda)}}, \tag{1.5}$$

resulting in a redshift-distance relation sensitive to the energy density of the universe. The integral can be evaluated for the standard cosmology ($\Omega_\Lambda = 0$) giving [23]

$$d_{\rm L} = \frac{H_0^{-1}}{\Omega_{\rm m}^2} [2\Omega_{\rm m} z + (2\Omega_{\rm m} - 4)(\sqrt{\Omega_{\rm m} z + 1} - 1)], \tag{1.6}$$

or in terms of the deceleration parameter, $q_0 = \frac{1}{2}\Omega_{\rm m}$,

$$d_{\rm L} = \frac{H_0^{-1}}{q_0^2}[q_0 z + (q_0 - 1)(\sqrt{2q_0 z + 1} - 1)]. \tag{1.7}$$

For the case $\Omega_\Lambda = 2/3$ and $\Omega_{\rm m} = 1/3$, corresponding to $q_0 = -1/2$, one obtains an elliptic integral for the comoving radial coordinate (1.5) so that

$$d_{\rm L} = H_0^{-1}(1+z)\sqrt{\frac{3}{2}}\int_1^{1+z}\frac{{\rm d}u}{\sqrt{1+u^3/2}}. \tag{1.8}$$

The luminosity distance as a function of redshift for the standard and ΛCDM models is plotted in Fig. 1. As redshift surveys push toward and beyond $z = 1$, it is becoming possible to accurately discriminate between models like these [29, 30].

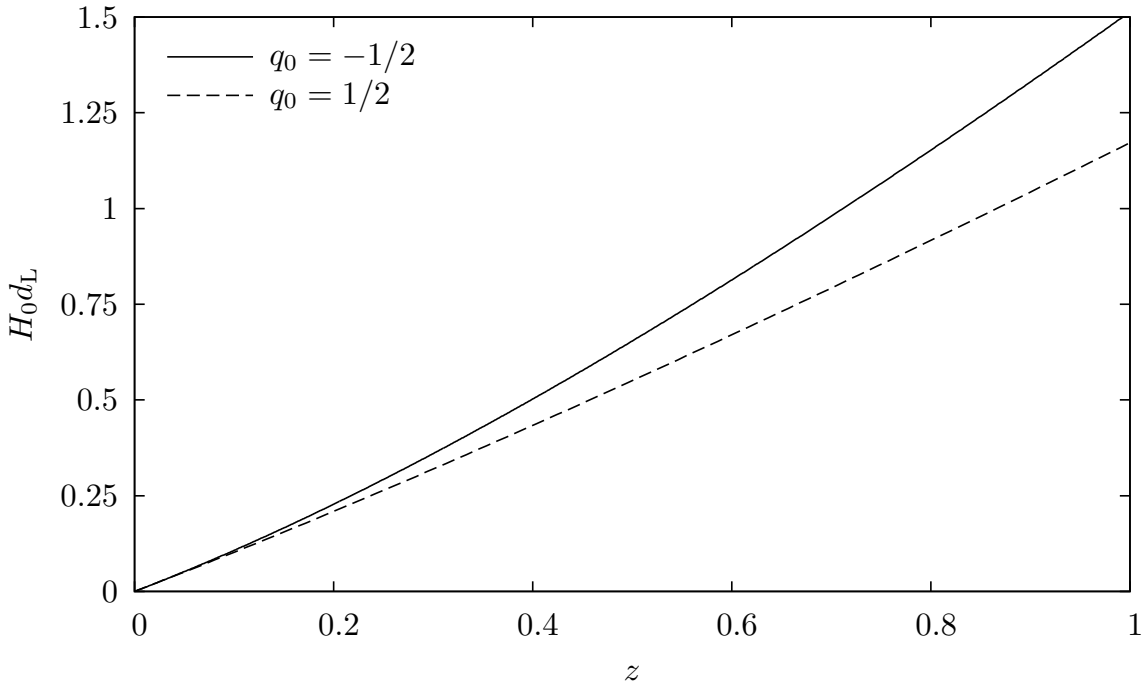

Fig. 1. The luminosity distance is shown as a function of redshift for two different models. The solid curve corresponds to an accelerating universe as predicted by ΛCDM Cosmology (1.8). The dashed curve corresponds to a decelerating universe with $\Lambda = 0$ (1.7).

D. Hubble Age

The Hubble age relation can be easily calculated from the definition of the Hubble parameter in the case of the standard cosmology. Integration of the Friedmann equation [23] gives the Hubble age relation for ΛCDM. For a flat universe (with $k = 0$ so that $\Omega_{\rm m} = 1 - \Omega_\Lambda$) the integration results in a Hubble age relation parameterized by the vacuum density parameter Ω_Λ, as shown in Fig. 2:

$$H_0 t_0 = \frac{2}{3}\Omega_\Lambda^{-\frac{1}{2}} \ln\left[\frac{1+\Omega_\Lambda^{\frac{1}{2}}}{(1-\Omega_\Lambda)^{\frac{1}{2}}}\right] \geq \frac{2}{3} \tag{1.9}$$

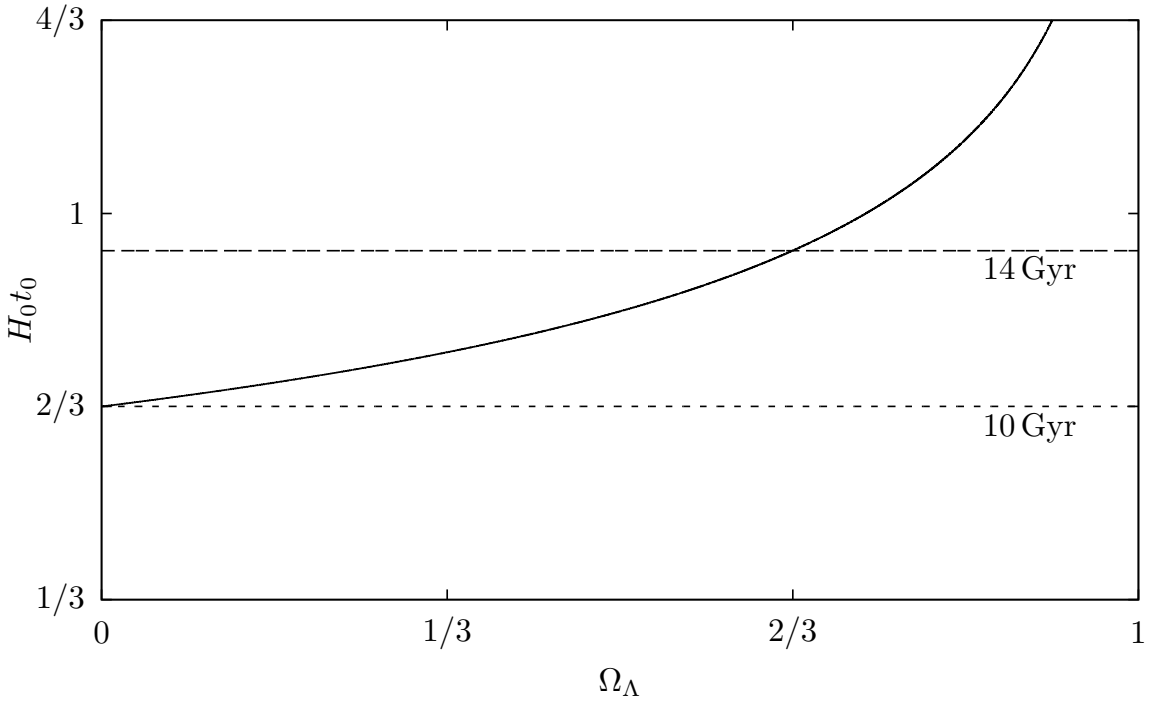

Fig. 2. Hubble age (1.9) is plotted as a function of vacuum energy density (solid curve) for a flat universe, with the specific times corresponding to $H_0^{-1} = 15\,\text{Gyr}$. The lower horizontal line (short dashes) marks the Hubble age, $t_0 = 10\,\text{Gyr}$, as predicted by the Standard Cosmology. The upper horizontal line (long dashes) marks a Hubble age, $t_0 = 14\,\text{Gyr}$, characteristic of ΛCDM.

and the equality holds in the limit $\Omega_\Lambda \to 0$. Table I summarizes the Hubble age relations and the Hubble age of the universe for a reasonable value of H_0 ($h = 0.65$).

Table I. Hubble age

Cosmological Model	**Hubble Age Relation**	**Hubble Age** ($h = 0.65$)
Standard Cosmology	$H_0 t_0 = 2/3$	$t_0 \simeq 10$ Gyr
ΛCDM Cosmology	$H_0 t_0 > 2/3$	(See Fig. 2)

1. Observations: Hubble Parameter

The early history of the Hubble parameter (1925–1975) was perhaps best expressed by Trimble in her review [31]: "...*The Incredible Shrinking Constant...*". Most notably, this period is marked by an order of magnitude drop in the measured value of the Hubble parameter ($H_0 \simeq 500\,\mathrm{km\,s^{-1}Mpc^{-1}} \longrightarrow H_0 \simeq 50\,\mathrm{km\,s^{-1}Mpc^{-1}}$) due to improvements in cosmography and telescope technology. The following decade (1975–1985) saw the division of measurements into the *long scale* ($H_0 \simeq 50$) or the *short scale* ($H_0 \simeq 100$); most published values of H_0 fell in the ranges 50–60 *or* 90–110 $\mathrm{km\,s^{-1}Mpc^{-1}}$. This discrepancy between the long and short scales evolved into the persistent "factor of two" uncertainty during the next decade (1985–1995): As of 1995, the published values of H_0 covered a nearly *continuous* range of 45–90 $\mathrm{km\,s^{-1}Mpc^{-1}}$. Several reviews are available recounting the early (1925–1975) improvements in cosmography [32]; sorting out the long and short scale division [33] in the following two decades (1975–1995); and describing the published values of H_0 over its entire history [33–35].

Table II. Hubble parameter as determined from SNe Ia, in some analyses of 1996-1998.

Method	H_0 ($\mathrm{km\,s^{-1}Mpc^{-1}}$)	(Year)
Cepheid calibrated	65 ± 7	(1998) [21]
Hubble diagram	60 ± 6	(1998) [36]
	67 ± 8	(1997) [37]
	$59 \pm 3, 62 \pm 4$	(1997) [38]
	58^{+7}_{-8}	(1997) [39]
	60 ± 5	(1997) [40]
	57 ± 4	(1996) [41]
	63 ± 7	(1996) [42]
	64 ± 6	(1996) [43]
	55 ± 3	(1996) [44]
Physical	56 ± 5	(1998) [45]
considerations	67 ± 9	(1996) [46]

Presently, the determination of the Hubble parameter through Cepheid-calibrated blue type Ia Supernovae (SNe Ia) and their Hubble diagram has the highest weight [47]. These determinations as well as physical determinations from SNe Ia have been reviewed by Branch [45]. Table II is largely due to this review. The Key Project [37, 48] reported a weighted mean of $H_0 = 73 \pm 10\,\mathrm{km\,s^{-1}Mpc^{-1}}$ resulting from several methods, a value which has been consistent for nearly a decade now. More recent observations and analyses, principally by Freedman and coworkers [49–51] give a value of about 70-72 $\mathrm{km\,s^{-1}Mpc^{-1}}$, and this approximate value is confirmed by the analysis of the Wilkinson Microwave Anisotropy Probe (WMAP) team [52, 53].

Gravitational lensing of quasars provides a geometric distance independent of

the standard extragalactic distance scale [54]. The possibility of testing cosmological theories using the difference in the travel time of light from multiply-imaged distant quasars by nearby galaxies was first proposed in 1964 by Sjur Refsdal [55, 56]. Specifically, Refsdal pointed out the connection between the delay in arrival time of multiple images of variable background sources (quasars) due to foreground galaxies, and the Hubble parameter. D. Walsh, R. F. Carswell, and R. J. Weymann announced the detection of Q0957+561 – the first gravitational lens (GL) system – in 1979 [57], stirring much excitement and establishing a new field of research.

To date, robust time delays for at least eleven lens systems have been measured, from which ten reliable estimates of the Hubble parameter are derived. A sample of determinations of H_0 from gravitational lensing are compiled in Table III. Distance determinations are strongly dependent on the astrophysical model of the GL as well as the cosmological model. Despite these model dependencies, however, determinations of the Hubble parameter from gravitational lensing are consistent with those from well established methods. GL system Q0957+561 is the most studied lens system to date, but recent findings render all measurements prior to 2000 inadmissible [58] due to the unique nature of the lens geometry. Kochaneck & Schechter [59] combine the GL systems PG1115+080, SBS1520+530, B1600+434, and HE2149-2745 to arrive at $H_0 = 48 \pm 3\,\mathrm{km\,s^{-1}Mpc^{-1}}$ for the isothermal (flat rotation curve) lens model, and $H_0 = 71 \pm 3\,\mathrm{km\,s^{-1}Mpc^{-1}}$ for the constant mass-to-light (no dark matter halo) lens model; Both models assume a flat universe with $\Omega_\mathrm{m} = 0.3$ and $\Omega_\Lambda = 0.7$. In general, recent determinations of the Hubble parameter from a single lens system usually fall into two categories: A low value corresponding to an isothermal lens model, and a high value corresponding to a lens model with constant mass-to-light (M/L) ratio. Also using $(\Omega_\mathrm{m}, \Omega_\Lambda) = (0.3, 0.7)$, Cardone et al. [60] determine $H_0 = 58^{+26}_{-22}\,\mathrm{km\,s^{-1}Mpc^{-1}}$ using a new method which makes only the most general assumptions concerning the

Table III. Hubble parameter as determined from gravitational lensing of quasars

Lens System	H_0 ($\mathrm{km\,s^{-1}Mpc^{-1}}$)	Ω_m	Ω_Λ	Year
Q0957+561	64 ± 13	1.0	0.0	1997 [61]
	64^{+17}_{-13}	0.25	0.75	1997 [61]
	77^{+29}_{-24}	1.0	0.0	1999 [62]
	51^{+14}_{-10}	1.0	0.0	1999 [63]
	55^{+14}_{-10}	0.3	0.0	1999 [63]
PG1115+080	52 ± 14	1.0	0.0	1997 [64]
	42 ± 12	1.0	0.0	1997 [65]
	51^{+14}_{-13}	1.0	0.0	1997 [66]
	51^{+21}_{-13}	0.2	0.8	1997 [66]
	68^{+25}_{-32}	0.3	0.7	2002 [60]
B0218+357	62^{+20}_{-10}	1.0	0.0	1996 [67]
	61 ± 7	0.3	0.7	2004 [68]
	70 ± 5	0.3	0.7	2004 [68]
B1422+231	47^{+31}_{-22}	0.3	0.7	2002 [60]
RXJ0911+0551	71 ± 4	0.3	0.7	2002 [69]
	49 ± 5	0.3	0.7	2003 [70]
	67 ± 5	0.3	0.7	2003 [70]
B1608+656	63 ± 15	0.3	0.7	2002 [71]
FBQ0951+2635	60^{+11}_{-9}	0.3	0.7	2004 [72]
	63^{+10}_{-8}	0.3	0.7	2004 [72]

lens model. York et al. [68] have obtained deep optical images of the lens system B0218+357 using the Advanced Camera for Surveys (ACS) installed on the Hubble Space Telescope (HST) in 2002, enabling the determination of the position of the lens galaxy accurately. They find high and low values for H_0 (see Table III) corresponding to the inclusion and exclusion, respectively, of the spiral arms in the lens model.

Currently, there are approximately seventy known cases of gravitational lensing by galaxies [73] of which only fifteen are candidates for time-delay monitoring, but the ability to bypass the standard piecewise extragalactic distance scale and associated uncertainties is a strong motivation. The recently formed group COSMOGRAIL (COSmological MOnitoring of GRAvitational Lenses) has embarked on a mission to help design future monitoring campaigns of lensed quasars, constructing and testing two hundred lens models for each of the fifteen GL candidates – for a total of three thousand lens models [74, 75]. Furthermore, Kochanek et al. [76] and others [77] have pointed out that it is possible to derive constraints on the rotation curve of the lens galaxy by assuming a reasonable value for the Hubble parameter.

2. Observations: Age of the Universe

A consistent model is one in which the expansion age, as inferred by measuring H_0 (and Ω_0), agrees with an independently estimated age of the universe. The most readily available independent estimate comes from the age of the oldest stars, as found in globular clusters. Another estimate may be made by making use of nuclear cosmochronometers based on the decay of long-lived radioactive elements. Recently, white dwarf cooling theory has also gained recognition as an indicator of the minimum age of the universe. Of course, all of these determinations depend on models of stellar and galactic evolution. The ages of the Sun and galaxy determined by various methods are compiled in Table IV. The recent results from WMAP [52] provide a very accurate

Table IV. Lower bounds on the age of the universe as indicated by the ages of the Sun and Milky Way galaxy. A recent accurate age determination using WMAP measurements is included.

	Method of Determination	Age (Gyr)	Year
Sun	Meteoritic Dating	4.53 ± 0.04	1997 [78]
	Helioseismology	4.5 ± 0.1	1997 [78]
Galaxy	White Dwarfs	8 ± 1.5	1998 [79]
	White Dwarfs	$10.5^{+2.5}_{-1.5}$	1996 [80]
	Globular Clusters	11.5 ± 1.3	1997 [81]
	Globular Clusters	$11.8^{+2.1}_{-2.5}$	1997 [82]
	Globular Clusters	12 ± 1.5	1998 [83]
	Nucleocosmochronology (^{232}Th/^{238}U)	12.8 ± 3	1997 [84]
	Nucleocosmochronology (Th/Eu)	15.2 ± 3.7	1997 [85]
Cosmography	Cosmic Background Radiation	$13.7^{+0.1}_{-0.2}$	2006 [52]

determination of the age of the universe, $13.7^{+0.1}_{-0.2}$ Gyr (flat universe).

E. Deceleration Parameter

Conventional cosmologies relate the deceleration parameter to the energy content of the universe according to $q_0 = \frac{1}{2}\left(\Omega_0 + 3\sum_i w_i \Omega_i\right)$, where the Ω_i represent the variety of non-luminous matter and the w_i are from the equations of state, $p_i = w_i \rho_i$, of the 'cosmic fluid'. Therefore, $q_0 = \frac{1}{2}$ and $q_0 = -\frac{1}{2}\left(3\Omega_\Lambda - 1\right) \sim -\frac{1}{2}$ for standard and ΛCDM cosmologies, respectively, since $w_i = 0$ for cold matter and $w_i = -1$ for the cosmological constant, with $\Omega_0 = 1$ corresponding to a flat universe, and $\Omega_\Lambda \sim \frac{3}{4}$ indicated by the observations.

The predictions for the deceleration parameter set the two models completely

apart from each other (Table V). The old standard cosmology predicts a decelerating universe, and ΛCDM predicts an accelerating universe, as indicated by the more recent observations described below.

Table V. Deceleration parameter.

Cosmological Model	**Deceleration Parameter**
Standard Cosmology	$q_0 = +1/2$
ΛCDM Cosmology	$q_0 \sim -1/2$

1. Observations

The main methods of determining cosmological deceleration fall into three groups. The first group determines q_0 by evaluating the mean mass density of the universe, whereas methods in groups two and three do so directly from the apparent magnitude-redshift $(m - z)$ and angular diameter-redshift $(\theta - z)$ relations. These methods, as well as the history of early attempts to measure the deceleration parameter, are reviewed by Fang et al. [86]

Table VI. Measurements of the deceleration parameter.

Method	q_0	(Year)
Supernovae Ia	$-1.0 \pm 0.4 \leq q_0 \leq 0$	(1998) [21]
	$q_0 = 0.7 \pm 0.5$	(1996) [46]
	$q_0 \geq 0$	(1996) [18]
	$q_0 = 0.1 \pm 0.85$	(1995) [87]
Redshift-Volume Test	$q_0 \leq 0.10$	(1998) [88]
Gravitational Lensing	$q_0 > -2.0$	(1997) [89]
Angular Diameter Distances	$q_0 = 0.85 \pm 0.29$	(1997) [90]

Some attempts to determine the deceleration parameter are tabulated in Table VI. Most remarkable is the observation of an *accelerating* universe in 1998 [21, 22]. This finding has drastically changed the understanding of the present state and future of cosmic expansion.

F. Energy Density

It is generally agreed that the total energy density of the universe (Ω_0) is dominated by baryonic matter (Ω_b), at least one non-luminous matter component (Ω_nl) such as cold dark matter, and some form of dark energy which is perhaps most likely a cosmological constant (Λ). Conventional cosmologies ($k = 0$) account for the energy densities as follows:

$$\underbrace{\Omega_\mathrm{b} + \Omega_\mathrm{nl}}_{\Omega_\mathrm{m}} + \Omega_\Lambda \simeq \Omega_0 \tag{1.10}$$

with $\Omega_\Lambda \equiv \frac{1}{3} H_0^{-2} \Lambda$. Table VII characterizes the different models in terms of the energy densities. Both the old standard and the ΛCDM cosmologies with an inflationary scenario require that $\Omega_\mathrm{m} + \Omega_\Lambda = 1$ to insure flatness [91].

Table VII. Energy density.

Cosmological Model	**Vacuum Density**	**Matter Density**	**Total Density**
Standard Cosmology	$\Omega_\Lambda = 0$	$\Omega_\mathrm{m} \simeq \Omega_0$	$\Omega_0 = 1$
ΛCDM Cosmology	$\Omega_\Lambda > 0$	$\Omega_\mathrm{m} \simeq 1 - \Omega_\Lambda$	$\Omega_0 = 1$

1. Observations

The Supernova Cosmology Project reported [22] $\Omega_{\rm m} = 0.28^{+0.09}_{-0.08}$ for a flat universe ($\Omega_\Lambda \simeq 0.7$) and $\Omega_{\rm m} = 0.2 \pm 0.4$ for $\Omega_\Lambda \simeq 0$. There is good agreement between this group and the High-Z Supernova Search Team, who obtained [21] $\Omega_{\rm m} = 0.32 \pm 0.10$, $\Omega_\Lambda = 0.68 \pm 0.10$ or $\Omega_{\rm m} = 0.16 \pm 0.09$, $\Omega_\Lambda = 0.84 \pm 0.09$ depending upon methodology. Both teams employ the redshift-distance relation together with multi-color light curve shapes and sophisticated statistical techniques to account for systematic uncertainties. The Canadian Network for Observational Cosmology (CNOC) report [92] $\Omega_{\rm m} = 0.19 \pm 0.06$ for $\Omega_\Lambda \simeq 0$ using mass-to-light ratios of galaxy clusters. Efstathiou et al. [93] combine the results of Perlmutter et al. [22] with cosmic microwave background data to find $\Omega_{\rm m} = 0.25^{+0.18}_{-0.12}$ and $\Omega_\Lambda = 0.63^{+0.17}_{-0.23}\,(2\sigma)$. The 2dF collaboration [94] apply a power spectrum analysis based on nearly a quarter million galaxies, resulting in $\Omega_{\rm m} = 0.231 \pm 0.021$.

Upper bounds have also been placed on the vacuum energy density. The CNOC find [92] $\Omega_\Lambda < 1.5$. Independent upper bounds have been determined by gravitational lensing statistics. Chiba and Yoshi report [95] $\Omega_\Lambda \lesssim 0.9$. Kochanek reports [96] the further constraint $\Omega_\Lambda \lesssim 0.66$. Virtually all recent observations, including those from the WMAP collaboration [52], the SDSS collaboration [97], the High-Z Supernova Search Team [21], and the Supernova Cosmology Project [22], are consistent with $\Omega_{\rm m} \approx 0.3$ and $\Omega_\Lambda \approx 0.7$. Independent estimates of galaxy cluster masses using velocity dispersion (virial mass), X-ray emission temperature, and gravitational lensing are in agreement with each other and provide firm evidence of a large dark matter component of the total energy density of the universe [98].

G. Discussion

It is already evident that the old standard cosmology will come to be known as an idealized historical model. ΛCDM holds great promise, as it is a well-founded conventional cosmological model that is consistent with observations. If correct, the implications of this new paradigm are dramatic: The present state of cosmic acceleration is reversed; the age of the universe is significantly larger; and Einstein gravity in the traditional sense (involving only matter), is weak and becoming negligible. Although the matter density $\Omega_{\rm m} \approx 0.3$ is measured to be much lower than the preferred $\Omega_{\rm m} = 1$ of the old standard cosmology, it remains in disagreement with the observed luminous matter, yet general relativity continues to pass the strictest tests [99]. This discrepancy defines – in the broadest sense – the dark matter problem. The details of this discrepancy are discussed in the following chapter.

Observations in the forseeable future should introduce yet more precision into cosmological modelling. New satellite experiments are planned to map the relic cosmic microwave background radiation with an angular resolution of 0.01°: These measurements will provide an independent determination of a number of cosmological parameters [15, 100] including the total energy density (Ω_0), the fraction of the critical density contributed by matter ($\Omega_{\rm m}$), the vacuum energy density (Ω_Λ), the neutrino density (Ω_ν), and the baryon density ($\Omega_{\rm b}$), as well as the Hubble parameter (H_0).

CHAPTER II

THE NATURE OF GALACTIC DARK MATTER

A. Galaxy Clusters

The first indications of some form of missing mass date to 1933 with the suggestion by Fritz Zwicky [101, 102] that additional (dark) matter could explain the anomalous line-of-sight velocity dispersions in the Coma cluster. This cluster was determined anomalously to be two orders of magnitude larger than the accepted value.

> Es ist natürlich möglich, dass leuchtende plus dunkle (kalte) Materie zusammengenommen eine bedeutend höhere Dichte ergeben, und der Wert $\bar{\rho} \sim 10^{-28}\,\mathrm{gr/cm^3}$ erscheint daher nicht unvernünftig.
>
> Translation: It is, of course, possible that luminous plus dark (cold) matter, taken together, result in a significatly greater density, and the value $\bar{\rho} \sim 10^{-28}\,\mathrm{gr/cm^3}$ seems therefore unsatisfactory.

Zwicky also suggested that this problem extends to other rich clusters. Three years later (1936) Sinclair Smith [103] used similar methods to determine an anomalously high mass for the Virgo cluster. Smith derived a mass for this cluster which was also two orders of magnitude larger than the accepted value. Referring to the masses derived for Coma and Virgo, Smith suggested:

> It is also possible that both values are essentially correct, the difference representing internebular material, either uniformly distributed or in the form of great clouds of low luminosity surrounding the nebulae, as suggested by the recent great extension of M31. Whatever the correct answer, it cannot be given with certainty at this time.

It should be noted that the large estimates of the total mass of the Coma and Virgo clusters by Zwicky and Smith were partly due to the overestimate of the Hubble constant [7, 104], then thought to be $H_0 \approx 558\,\mathrm{km\,s^{-1}Mpc^{-1}}$. The Hubble constant was later measured to be an order of magnitude smaller [31], the effect of which was to decrease the discrepancy between luminous and total matter in the Coma and Virgo clusters to a single order of magnitude.

B. Galactic Rotation Curves

Observations of the nearby Andromeda galaxy by Babcock [105, 106] indicated the necessity for additional mass within individual galaxies as early as 1939. Babcock was the first to interpret the optical rotation curve of the outer regions of the Andromeda galaxy as an indication of the presence of non-luminous matter within a galaxy.

> The period of the outer arms, on the other hand, is about 9.2×10^7 years, and the obvious interpretation of the nearly constant angular velocity from a radius of 20 minutes of arc outward is that a very great proportion of the mass of the nebula [Andromeda galaxy] must lie in the outer regions.

Jan Oort [107, 108] derived the distribution of luminous matter in the edge-on Spindle galaxy (NGC 3115) by measuring peculiar velocities and compared this to the distribution of matter derived using Humason's unpublished rotational velocites. He states that cleary: the distribution of matter is very different than that of light; the additional matter is not absorbing light; a program to measure rotational velocities at greater distances from the center of spiral galaxies is needed.

> It may be concluded that the distribution of mass in the system must be considerably different from that of light. A study of the light-distribution

> does not, therefore, enable us to draw conclusions regarding such problems as stability or the total mass of the system.
>
> The strongly condensed luminous system appears imbedded in a large and more or less homogeneous mass of great density.
>
> For, if the great density in the nebula [NGC 3115] were due to such absorbing matter, the transparency would be so low that we could not penetrate more than a very few parsecs into the system.
>
> There cannot be any doubt that an extension of the measures of rotation to greater distances from the nucleus would be of exceptional interest.

Precise measurements of the optical (H_α) rotation curve of Andromeda galaxy by Ruben and Ford [109] in 1970 extended Babcock's curve to a radial distance of 24 kpc, well beyond the luminous disk.

> Beyond $R = 4\,\mathrm{kpc}$ the total mass of the galaxy increases approximately linearly to $R = 14\,\mathrm{kpc}$, and more slowly thereafter. The total mass is $M = (1.85 \pm 0.1) \times 10^{11}\,M_\odot$; one-half of it is located in the disk interior to $R = 9\,\mathrm{kpc}$.

Roberts and Whitehurst [110] made a detailed study of the geometry of Andromeda galaxy and further extended the rotation curve to 30 kpc using 21-cm observations in 1975. They constructed a rotation curve for Andromeda galaxy using their 21-cm observations combined with the optical observations of Ruben and Ford, and stated decisively:

> New 21-cm observations of the southern end of M31 indicate (1) that the plane of HI is bent away from the conventional plane by up to $\sim 5\,\mathrm{kpc}$ and (2) that the rotational velocity is essentially constant over the outer

> 10 kpc, i.e., from 20 to 30 kpc radius. The latter implies a mass that increases linearly with R over this range and a mass-to-luminosity ratio of $\gtrsim 200$ for this outer region.

They also mention that they had found similar results in six other galaxies. It was evident that the usual Keplerian prediction of declining rotational velocity had to be abandoned. An HI region in the galactic halo is expected to have circular orbits described by (adopting the notation of the authors under discussion [109, 110])

$$\frac{GM(R)}{R^2} = \frac{V^2(R)}{R} \quad \Longrightarrow \quad \begin{cases} V(R) \sim R & \text{for } R \longrightarrow 0, \\ V(R) \sim \dfrac{1}{\sqrt{R}} & \text{for } R \longrightarrow \infty, \end{cases} \tag{2.1}$$

where $M(R)$ is the mass interior to R. It was observed that velocities in the inner region of a galaxy increase linearly, as expected. In the outer regions, however, the velocities were observed to increase to a maximum value and remain constant, independent of the radial coordinate. This latter observation suggests that the mass increases linearly with galactic radial coordinate. That is,

$$V(R) = V_{\max} \quad \Longrightarrow \quad M(R) \sim R \ \text{ or } \ \rho(R) \sim \frac{1}{R^2} \quad \text{for large } R. \tag{2.2}$$

It was inferred from this simple dynamical argument that large amounts of non-luminous matter exist in galactic halos.

By 1980 Ruben, Ford, and Thonnard [111] had made precise measurements of the rotation curves of 21 spiral (Sc) galaxies of varying size, including velocities at radial distances $4\,\text{kpc} \leq R \leq 84\,\text{kpc}$. It was observed in the outer regions of every galaxy in the sample that rotational velocities either increased or remained constant with increasing R. The authors were undoubtedly surprised by this result and the degree of universality:

> Beyond the nucleus, all galaxies, big and small alike, share a surprisingly similar pattern of velocity variation with R (R on a linear scale). Velocities rise rapidly within about 5 kpc, and more slowly thereafter; rotation curves are flat only at very large R.
>
> The conclusion is inescapable that non-luminous matter exists beyond the optical galaxy.

The results were rigorous and without exception. The authors included the image tube spectra for all 21 galaxies as well as photographs for 17 of the 21 galaxies, perhaps to emphasize the astonishing results. (Also included was a point-by-point identification of the problems inherent in virtually all previous works that resulted in rotation curves deviating significantly from their findings.) They reported the same characteristic flat rotation curves for 60 Sa, Sb, and Sc galaxies of varying Hubble type and luminosity in 1985 [112, 113].

> These observations suggest that the forms of the distributions of mass within the more extended halos are similar except for radial and/or density scale factors, independent of the morphology of the optical galaxy.
>
> The form of mass distribution is not strongly dependent on either Hubble type or intrinsic luminosity, so the 'average' form of rotation curve should be of similar shape for all galaxies, Sa through Sc.
>
> Some mechanism unrelated to the global property of a galaxy determines the form of mass distribution; we suggest that this mechanism is the intital environment of the protogalaxy.

C. Cosmological Structure and Dark Matter

Arno Penzias and Robert Wilson of Bell Labs discovered the cosmic microwave background (CMB) radiation in 1964, measuring the temperature to be $3.5 \pm 1.0\,\mathrm{K}$ [9]:

> This excess temperature is, within the limits of our observations, isotropic, unpolarized, and free from seasonal variation (July, 1964 - April, 1965). A possible explanation for the observed excess noise temperature is the one given by Dicke, Peebles, Roll, and Wilkinson (1965) in a companion letter in this issue.

The companion letter by Dicke, Peebles, Roll, and Wilkinson [114], appropriately titled "Cosmic Black-Body Radiation", and previous predictions of this radiation in the context of an expanding universe model by Gamow [115] and by Alpher and Herman [116, 117], correctly identified this radiation as a relic from the thermal decoupling of matter and radiation at large redshift. Other cosmological models could not provide a satisfying explanation for the observed isotropic, near-perfect blackbody spectrum, which could only have been produced in a universe described by extreme homogeneity – the early universe. By 1967 the CMB blackbody temperature had accurately been measured to be $2.7 \pm 0.2\,\mathrm{K}$ [118–120].

An immediate test of the consistency of the interpretation of the CMB was considered in a brilliant paper by Wagoner, Fowler, and Hoyle [121], also in 1967. Following up on earlier attempts [8, 115, 122, 123] to calculate the primordial abundances of the light elements, precise calculations of the relative abundances of D, He^3, He^4, and Li^7 formed in the early universe were found to be in agreement with observed abundances and with the recently measured CMB blackbody temperature. It is ironic that this paper is the source of the precise convergence of primordial nucleosynthesis and CMB physics. Indeed, the authors were not advocating the

expanding universe model as is stated clearly in their original paper, uncommittingly titled "On the Synthesis of Elements at Very High Temperatures":

> A detailed calculation of element production in the early stages of a homogeneous and isotropic expanding universe as well as within imploding-exploding supermassive stars has been made. If the recently measured microwave background radiation is due to primeval photons, then significant quantities of D, He^3, He^4, and Li^7 can be produced in the universal fireball. Reasonable agreement with solar-system abundances for these nuclei is obtained if the present temperature is 3 K and if the present density is $\sim 2 \times 10^{-31}\,\mathrm{gm\,cm^{-3}}$, ...
>
> We conclude that D, He^3, He^4, and Li^7 in solor-system abundances could well have been produced during some early stage of a universe with $h \approx 7 \times 10^{-6}$ and with $q_0 \approx 5{\times}10^{-3}$, $T_0 \approx 3\,\mathrm{K}$, and $\rho_\mathrm{b} \approx 2{\times}10^{-31}\,\mathrm{gm\,cm^{-3}}$ at the present time. However, there are a number of attractive alternative explanations for the solar-system abundances of the light nuclei.

The "attractive alternative explanations" referred to models involving stellar production of the entire observable abundance of helium, later found to be insufficient. Nonetheless, this work provided the solution to the 'mass gap' problem, definitively proving that Big Bang nucleosythesis (BBN) can account for the abundances of the light elements. Having successfully incorporated the newly discovered muon-neutrino [124] into the nuclear reactions which governed the primordial element production, this was also a success for the emerging Standard Model of particle interactions. (The electron and muon neutrinos had only recently been detected: in 1956 and 1962, respectively.) In modern times the discrepancy between the upper limit on baryonic matter density derived from BBN [15], $\Omega_\mathrm{b} \lesssim 0.05$, and the lower limit

on total matter density found from observations, $\Omega_{\rm m} \approx 0.3$, is the most compelling evidence for the nonbaryonic nature of dark matter. This discrepancy is reinforced by the extremely accurate measurements of the CMB [52]: $\Omega_{\rm b} \approx 0.04$ and $\Omega_{\rm m} \approx 0.24$.

Also motivated by the discovery of the CMB (and also in 1967) was the work by Sachs and Wolfe describing the general relativistic mechanism for the production of large scale structure in an expanding universe model and the predicted signature in the CMB [125]:

> The models are used to estimate the anisotropy of the microwave radiation, assuming the radiation is cosmological. It is estimated that density fluctuations now of order 10 per cent with characteristic lengths now of order 1000 Mpc would cause anisotropies of order 1 per cent in the observed microwave temperature due to the gravitational redshift and other general-relativistic effects.

Matter overdensities and underdensities present at the time that electrons and protons formed neutral hydrogen (epoch of last scattering) caused inhomogeneities in the intensity of radiation through their gravitational perturbations (Sachs-Wolfe effect [125, 126]), and are observed as small temperature fluctuations (anisotropies) in the CMB in the present epoch. The small temperature fluctuations in the CMB revealed the distribution and density of matter in the early universe, before any complex structures were formed. It was immediately recognized that observations of structure in the form of galaxies, clusters, and superclusters in the present epoch could be compared to the distribution and density of matter derived from these small temperature fluctuations to gain an understanding of cosmological structure formation and evolution.

In 1978, a two-stage bottom-up view of structure formation was proposed by White and Rees [127]:

> We suggest that this material constitutes the so-called 'missing mass' in clusters and the extensive halos of isolated galaxies; we further suggest that *all* the luminous matter seen in galaxies formed from residual gas that settled within the potential wells provided by the dark material at each stage of the clustering process and then collapsed to form stars.

D. Dark Matter Candidates

1. Hot Dark Matter

Hot dark matter was inspired by the premature claim of a measurment for the electron neutrino mass [128]. The 30 eV rest mass was attractive in that it could possibly make up for the missing mass and solve the small-scale structure problem [129]. In a "top-down" fragmentation theory of structure formation superclusters would form first, and then fragment into clusters and then galaxies. The temperature variations in the CMB in the present epoch would have to be large unless they were washed out by free-streaming. It was later found that the mass measurment turned out to be incorrect. The unnatural top-down theory was later replaced by the "bottom-up" hierarchical model. Computer simulation proved that neutrinos did not form enough small-scale structure.

2. Warm Dark Matter

Warm dark matter particles are simply cold dark matter particles with initial (relativistic) velocities and have been described as *fast CDM* or *cooled-down HDM* [130]. Indeed, WDM models appear to be the "best of both worlds" by

design. Initial velocities have been attributed to the particles having decoupled as thermal relics, or having been formed via non-equilibrium decay; these processes have been studied in detail [130]. N-body simulations [131] indicate that WDM behaves as expected and, in many respects, similar to CDM. Despite their large velocities (relative to CDM), WDM particles bind to form sub-galactic-scale structure due to their large masses $\sim 1\,\mathrm{keV}$ (relative to HDM). In fact, the large velocities result in lower halo concentrations and core densities, and increased core radii (relative to CDM). Accordingly, large-scale structure also emerges, but with fewer low-mass satellites. It is easy to overstate the success of WDM models. For example, structure on the smallest scales is lost due to free streaming, so that dwarf spheroidal galaxies would be under-represented. Recent indications from WMAP combine temperature-temperature "TT" and temperature-polarization "TE" data indicating early re-ionization [132]. This implies that structure formation began at large redshifts, contrary to warm dark matter models which suppress structure formation until much later times [133].

3. Cold Dark Matter

High resolution N-body simulations have ruled out hot dark matter (HDM) and have shown cold dark matter (CDM) models to be most consistent with observations [134, 135]. The simulations indicate that HDM fails to form small-scale structure, while CDM forms too much small-scale structure, as well as central cusps in the density profile. It is possible that complex astrophysical processes are responsible for the smoothing out of this small-scale structure [136], and that existing cosmological simulations do not represent the extreme environments at the centers of galaxies accurately. The lightest supersymmetric particle of the supersymmetric extension of the Standard Model is currently the most likely candidate [137–139].

Modern high resolution N-body simulations have achieved successful recreation of small-scale and large-scale structure over cosmological distances and times. Sophisticated particle-mesh, hierarchical-tree, and particle-particle routines [140–142] prove the ability of CDM to form galactic and sub-galactic scale structures in approximate agreement with the structure observed through galaxy counts and microlensing. Problems with the CDM model at both scales are also revealed: CDM simulations predict overdensities on both scales, and cusps in the density profiles at galactic centers [143–145]. A systematic study of halo density profiles for a wide range of halo masses and cosmologies was carried out by Navarro, Frenk, and White (NFW) [134, 135], who argue that an analytical profile of the form

$$\rho(r) \propto \frac{1}{(r/r_s)(1+r/r_s)^2} \propto r^{-1} \text{ as } r \to 0 \tag{2.3}$$

provides a good description of all CDM halos within the current limits of resolution.

CHAPTER III

LORENTZ VIOLATION

We begin this section with a brief review of Lorentz violation that follows the introductory material in a paper by Allen and Yokoo [146]: During the past few years there has been increasingly widespread interest in possible violations of Lorentz invariance [146–185]. There are several motivations for this interest.

Theoretical: Every current candidate for a superunified theory contains some potential for Lorentz violation, and the same is true for more restricted theories which attempt to treat quantum gravity alone. (By a "superunified theory" we mean one which includes all known physical phenomena, and which is valid up to the Planck energy.) Theories with potential for Lorentz violation include superstring/M/brane theories, canonical and loop quantum gravity, noncommutative spacetime geometry, nontrivial spacetime topology, discrete spacetime structure at the Planck length, a variable speed of light or variable physical constants, various other *ad hoc* theories, including one that specifically addresses the GZK cutoff [148], and a fundamental theory which is described elsewhere [147]. Even in a theory which has Lorentz invariance at the most fundamental level, this symmetry can be spontaneously broken if some field acquires a vacuum expectation value which breaks rotational invariance or invariance under a boost. (It should be mentioned that cosmology already provides a preferred frame of reference – namely a comoving frame, in which the cosmic background radiation does not have a dipole anisotropy – but this is not considered to be a breaking of Lorentz symmetry.) A second mechanism for Lorentz violation is the "quantum foam" of Hawking and Wheeler, originally envisioned in the context of canonical or path-integral quantization of Einstein gravity, but now generalized to other theories with quantum gravity. A third possibility is a theory

in which Lorentz invariance is not postulated to be an exact fundamental symmetry, but instead emerges as a low-energy symmetry [147].

Experimental: Both terrestrial [148–159] and space-based [160–165] experiments have been designed with exquisite precision which would permit detection of even tiny deviations from certain aspects of Lorentz invariance. The systems include atoms, charged particles in traps, masers, cavity-stabilized oscillators, muons, neutrons, kaons, and other neutral mesons.

Observational: Particles traveling over cosmological distances from bright sources (including pulsars, supernovae, blazars, and gamma ray bursters) allow long-baseline tests which are again sensitive to even tiny deviations from standard physics resulting from particular forms of Lorentz violation [166–171].

Recall that Lorentz invariance in the context of general relativity means *local* Lorentz invariance, or an invariance of the action under rotations and boosts involving locally inertial frames of reference. There is clearly a connection with the equivalence principle, which can also be tested in, e.g., space-based experiments. There is a close connection with CPT invariance as well: According to the CPT theorem, Lorentz invariance implies CPT invariance (with the supplementary assumptions of unitarity and locality). It follows that CPT violation implies Lorentz violation, although the reverse is not necessarily true [172]. Finally, there is a connection to the spin-statistics theorem, which follows from Lorentz invariance and microcausality.

We know that P (in the 1950s) and CP (in the 1960s) have previously been found not to be inviolate symmetries, for reasons that are now understood in terms of the standard electroweak theory and the CKM matrix. Perhaps CPT and Lorentz symmetry are also not inviolate.

The most extensive theoretical program for systematizing potential forms of Lorentz violation and their experimental signals is that of Kostelecký and

coworkers [148, 149, 154–163, 165, 171]. Their philosophy is to add small phenomenological Lorentz-violating terms to the Lagrangian of the Standard Model, and then interact with a wide variety of experiments that can detect such deviations from exact Lorentz or CPT invariance. The point of view of this group is rather conservative: The fundamental theory (e.g., string theory) is pictured as Lorentz-invariant, with Lorentz or CPT violation arising from some form of symmetry-breaking – for example, with a vector field or more general tensor field acquiring a vacuum expectation value. Their work has stimulated a considerable amount of experimental activity, with further experiments planned for both terrestrial and space-based laboratories.

So far there is no undisputed evidence for Lorentz violation, and the only solid results from both experiment and observation are strong constraints on particular ways in which this symmetry might be broken. As an example of an astrophysical constraint, we mention a recent paper by Stecker and Glashow [169], in which they conclude

> We use the recent reanalysis of multi-TeV [up to $\sim 20\,\mathrm{TeV}$] gamma-ray observations of [the blazar] Mrk 501 to constrain the Lorentz invariance breaking parameter involving the maximum electron velocity. Our limit is two orders of magnitude better than that obtained from the maximum observed cosmic-ray electron energy.

Their analysis involves the processes

$$\gamma + \gamma_{\mathrm{infrared}} \to e^+ + e^- \quad \text{if} \quad c_e > c_\gamma, \tag{3.1}$$

which can lead to inconsistency with the observation of 20 TeV photons, and

$$\gamma \to e^+ + e^- \quad \text{if} \quad c_e < c_\gamma, \tag{3.2}$$

which can lead to inconsistency with the observation of 50 TeV photons.

Another example of astrophysical constraints is the series of analyses by Jacobson et al. [166–169]. In Ref. [167], Jacobson, Liberati, Mattingly, and Stecker state

> We strengthen the constraints on possible Lorentz symmetry violation (LV) of order E/M_{Planck} for electrons and photons in the framework of effective field theory (EFT). The new constraints use (i) the absence of vacuum birefringence in the recently observed polarization of MeV emission from a gamma ray burst and (ii) the absence of vacuum Čerenkov radiation from the synchrotron electrons in the Crab nebula, improving the previous bounds by eleven and four orders of magnitude respectively.

Jacobson, Liberati, and Mattingly [167] have obtained a very strong constraint on a dispersion relation with a cubic term in the expression for E^2:

$$E^2 = p^2 + p^3/M. \tag{3.3}$$

However, the constraint is less stringent for what may be the more natural form with a quartic term:

$$E^2 = p^2 + p^4/M^2. \tag{3.4}$$

Coleman and Glashow [148] proposed that the limiting velocity of protons, electrons, etc. may be very slightly different from the speed of light. (See also Ref. [169].) This is an *ad hoc* proposal, motivated by the apparent absence of a Greisen-Zatsepin-Kuz'min (GZK) cutoff: Ultrahigh energy cosmic ray protons colliding with the cosmic microwave background radiation should produce pions,

$$p + \gamma_{\text{CMB}} \to p + \pi^0. \tag{3.5}$$

There should consequently be a cutoff in the spectrum of observed protons at about

50 EeV (or 5×10^7 TeV), if they were created in processes at distances of more than about 100 Mpc. But up to 300 EeV cosmic rays (presumably protons) appear to be observed, although this is not entirely certain [183], and there are also theoretical ideas for a closer origin [185].

We conclude by mentioning some reviews of terrestrial and space-based experiments.

Two reviews of atomic experiments to test both Lorentz and CPT symmetries, by Bluhm [160], describe the following: (1) Penning trap experiments with electrons and positrons, and with protons and antiprotons, which look for differences in frequencies or sidereal time variations; (2) clock comparison experiments, with clock frequencies typically those of hyperfine or Zeeman transitions; (3) hydrogen and antihydrogen experiments involving ground-state Zeeman hyperfine transitions (at Harvard) or 1S-2S transitions (proposed at CERN); (4) a spin-polarized torsion pendulum experiment (at the University of Washington); (5) muon and muonium experiments.

Two reviews by Russell [164] discuss clock-based experiments to test Lorentz and CPT invariance in space. Such experiments will probe the effects of variations in both orientation and velocity. Among the systems are H masers, laser-cooled Cs and Rb clocks, and superconducting microwave cavity oscillators. A number of specific space missions have been planned or proposed.

Finally, a review by Kostelecký [173] contains a discussion of experiments involving neutral meson (e.g. kaon) oscillations, a dual nuclear Zeeman He-Xe maser, and cosmological birefringence, in addition to the systems mentioned above.

CHAPTER IV

LORENTZ-VIOLATING DARK MATTER

An alternative to more conventional dark matter candidates might conceivably be particles that violate Lorentz invariance [147, 148, 150, 175, 186]. Here we present arguments indicating that Lorentz-violating dark matter (LVDM) particles with a minimum velocity experience weaker gravitational binding [187, 188] and, perhaps, less tendency to form small-scale structure as compared to CDM. It is worthwhile to ask if these particles will bind at all on the galactic scale.

A modified description of dark matter particles is a natural consequence of a new fundamental theory [147, 175] which is founded on a new form of supersymmetry and in which Lorentz invariance does not hold in general: This dark matter candidate is a supersymmetric, weakly-interacting massive particle, equivalent in all respects to the neutralino of standard supersymmetry aside from its equation of motion, which does not obey Lorentz invariance. Although we have suggested that the particles emerging from this fundamental theory have weaker gravitational binding than that of CDM candidates, it is enlightening to approach the problem from a purely phenomenological viewpoint including a large class of Lorentz-violating candidates [187, 188].

A. Gravitational Binding

Since the dark matter almost certainly consists of particles of a new kind, let us allow for the possibility that $v_0 \neq 0$, where v_0 is the limiting value of the particle velocity $v(p)$ as the 3-momentum $\mathbf{p}$ goes to zero. Suppose that the particle energy ε is expanded as a Taylor series in the magnitude p of the 3-momentum:

$$\varepsilon = \varepsilon(p) = \varepsilon_0 + pv_0 + p^2/2\widetilde{m} + \cdots. \tag{4.1}$$

(For conventional nonrelativistic particles, $\widetilde{m}$ is the particle mass, ε_0 is the rest mass energy, and $v_0 = 0$.) The particle velocity is then

$$v = \mathrm{d}\varepsilon/\mathrm{d}p = v_0 + p/\widetilde{m} + \cdots \tag{4.2}$$

and the kinetic energy is

$$T = \int v\,\mathrm{d}p = \varepsilon(p) - \varepsilon_0 = pv_0 + p^2/2\widetilde{m} + \cdots. \tag{4.3}$$

The virial theorem implies that

$$\langle pv\rangle = \langle \mathbf{p}\cdot\mathbf{v}\rangle = -\langle \mathbf{F}\cdot\mathbf{r}\rangle = \langle r\mathrm{d}U/\mathrm{d}r\rangle = -\langle U\rangle, \tag{4.4}$$

where it has been assumed that $U = -GMm/r$ with M constant. Since (4.3) can also be written as

$$T = pv - \int p\,\mathrm{d}v, \tag{4.5}$$

the binding energy $-E$ of a particle with 3-momentum p is given by

$$-E = -\langle T + U\rangle = \left\langle \int p\,\mathrm{d}v \right\rangle = \langle p^2\rangle/2\widetilde{m} + \cdots \approx \langle p^2\rangle/2\widetilde{m}. \tag{4.6}$$

If $v_0 = 0$ (as for a conventional nonrelativistic particle), the momentum is determined by

$$-\langle U\rangle = \langle pv\rangle = \langle pv_0 + p^2/\widetilde{m} + \cdots\rangle \approx \langle p^2\rangle/\widetilde{m} \text{ or } \langle p^2\rangle \approx \langle GMm\widetilde{m}/r\rangle \tag{4.7}$$

and the energy has the familiar form

$$E \approx \langle U\rangle/2. \tag{4.8}$$

On the other hand, if $v_0 \neq 0$, the momentum is determined by

$$-\langle U\rangle = \langle pv\rangle = \langle pv_0 + p^2/\widetilde{m} + \cdots\rangle \approx \langle p\rangle v_0 \text{ or } \langle p\rangle \approx \langle GMm/v_0 r\rangle \tag{4.9}$$

and the binding energy is much smaller:

$$E \sim -\frac{1}{2\widetilde{m}v_0^2}\langle U\rangle^2. \tag{4.10}$$

It is interesting that a general model with $v_0 \neq 0$ leads to the weaker binding (4.10), suggesting a weaker tendency to form both small-scale structure and cusps within galactic halos.

The specific form of $\varepsilon(p)$ in the fundamental theory of Refs. [147, 175, 187] yields

$$v(p) = \mathrm{d}\varepsilon/\mathrm{d}p = \left[1 + \left(\frac{p}{m} + b^{-1}\right)^{-2}\right]^{-1/2}, \tag{4.11}$$

where $b = 2m/\overline{m}$, m is the mass of the particle, and $\overline{m}$ is taken to be a parameter. (Here we have taken $c = 1$.) The usual expression (4.5) for the kinetic energy may be integrated by parts,

$$T = \int_0^p v(p')\,\mathrm{d}p' = vp - \int_{v_0}^v p(v')\,\mathrm{d}v', \tag{4.12}$$

where $v_0 \equiv v(p=0) = 1/\sqrt{1+b^2}$ and $p(v) = \gamma mv - \gamma_0 m v_0$ are found from (4.11) with the definitions: $\gamma \equiv 1/\sqrt{1-v^2}$ and $\gamma_0 \equiv \gamma(v_0) = 1/\sqrt{1-v_0^2}$. The result of the integration is

$$T = vp + \gamma_0 m v_0(v - v_0) + m(\gamma^{-1} - \gamma_0^{-1}). \tag{4.13}$$

For a circular orbit,

$$\frac{pv}{r} = \frac{GMm}{r^2} \quad \text{or} \quad \frac{\bar{r}_\mathrm{s}}{r} = v\left(\frac{p}{m}\right), \tag{4.14}$$

where $\bar{r}_\mathrm{s} = GM$. Then $vp = -U$, and the total energy is

$$E = T + U = \gamma_0 m v_0(v - v_0) + m(\gamma^{-1} - \gamma_0^{-1}). \tag{4.15}$$

The total energy may be expressed as a function of momentum with $v(p)$ given by

(4.11) and

$$\gamma^{-1} = \left[1 + \left(\frac{p}{m} + b^{-1}\right)^2\right]^{-1/2}. \tag{4.16}$$

We may expand the velocity (4.11) in powers of momentum to get

$$v(p) \approx v_0 + v_0^3 b^3 \left(\frac{p}{m}\right) - \frac{3}{2} v_0^5 b^4 \left(\frac{p}{m}\right)^2 \tag{4.17}$$

so that (4.14) becomes

$$\frac{\bar{r}_\mathrm{s}}{r} \approx v_0 \left(\frac{p}{m}\right) + v_0^3 b^3 \left(\frac{p}{m}\right)^2 - \frac{3}{2} v_0^5 b^4 \left(\frac{p}{m}\right)^3. \tag{4.18}$$

This result may be inverted to find the momentum in terms of radius. If we let

$$\frac{p}{m} \approx a_1 \left(\frac{\bar{r}_\mathrm{s}}{r}\right) + a_2 \left(\frac{\bar{r}_\mathrm{s}}{r}\right)^2 + a_3 \left(\frac{\bar{r}_\mathrm{s}}{r}\right)^3, \tag{4.19}$$

then the coefficients are found to be $a_1 = v_0^{-1}$, $a_2 = b^3$, and $a_3 = \frac{3}{2} v_0 b^4 (1 + \frac{4}{3} b^2)$. Substituting this into the expression for the total energy (4.15) and expanding in $\bar{r}_\mathrm{s}/r$ results in

$$\frac{E}{m} \approx -\frac{1}{2} v_0 b^3 \left(\frac{\bar{r}_\mathrm{s}}{r}\right)^2 + b^4 \left(\frac{\bar{r}_\mathrm{s}}{r}\right)^3. \tag{4.20}$$

The first term on the right-hand side is immediately verified by instead expressing the total energy (4.15) as a function of v, expanding about v_0, and recursively substituting the first order terms from the expansions for v (4.17) and p/m (4.19):

$$\left.\begin{aligned} \frac{E}{m} &\approx -\frac{1}{2}\gamma_0^3 (v - v_0)^2 \\ v - v_0 &\approx v_0^2 b^3 \left(\frac{p}{m}\right) \\ \frac{p}{m} &\approx v_0^{-1} \left(\frac{\bar{r}_\mathrm{s}}{r}\right) \end{aligned}\right\} \Longrightarrow \frac{E}{m} \approx -\frac{1}{2} v_0 b^3 \left(\frac{\bar{r}_\mathrm{s}}{r}\right)^2 (\gamma_0 v_0 b)^3 = -\frac{1}{2} v_0 b^3 \left(\frac{\bar{r}_\mathrm{s}}{r}\right)^2, \tag{4.21}$$

where $\gamma_0 v_0 b = 1$ (with $c = 1$) was used in the last step. This inverse-square binding

energy is the same as that of (4.10) with $\widetilde{m} = \gamma_0^3 m$. (Note: $v_0^{-2}\gamma_0^{-3} = v_0^{-2}v_0^3 b^3 = v_0 b^3$.) It appears that an orbiting LVDM particle would be less bound than an ordinary CDM particle having the standard $1/r$-dependent binding energy.

B. Constraints on Orbital Velocities

The kinetic energy (4.3) may be calculated by direct integration of (4.11):

$$T = \int_0^p v(p')\,\mathrm{d}p' = mc^2(\gamma - \gamma_0), \tag{4.22}$$

where $\gamma \equiv 1/\sqrt{1-(v/c)^2}$ and $\gamma_0 = \gamma(v_0)$. Consider a model in which the total energy of a LVDM particle in orbit about a central mass is given by

$$E = mc^2\,(\gamma - \gamma_0) - GMm/r. \tag{4.23}$$

A condition for bound states is that the total energy must be negative so that

$$-r_\mathrm{s}/r \le (mc^2)^{-1}E < 0, \tag{4.24}$$

where $r_\mathrm{s} \equiv GM/c^2$ is half the Schwarzschild radius. The maximum momentum p_max and velocity $u_\mathrm{max} = v_\mathrm{max}/c$ may be calculated by setting the total energy (4.23) equal to zero, resulting in

$$(mc)^{-1}p_\mathrm{max} = \left[(\gamma_0 + r_\mathrm{s}/r)^2 - 1\right]^{1/2} - \gamma_0 u_0, \tag{4.25}$$

$$u_\mathrm{max} = \left\{\left[(\gamma_0 + r_\mathrm{s}/r)^2 - 1\right]^{-1} + 1\right\}^{-1/2}. \tag{4.26}$$

Expanding in $r_{\rm s}/r$, the ranges of the maximum momentum and velocity may be expressed as

$$0 \leq \frac{p_{\rm max}}{mc} < \gamma_0 b \left(\frac{r_{\rm s}}{r}\right) - \frac{1}{2} b^3 \left(\frac{r_{\rm s}}{r}\right)^2, \tag{4.27}$$

$$u_0 \leq u_{\rm max} < u_0 + u_0^2 b^3 \left(\frac{r_{\rm s}}{r}\right). \tag{4.28}$$

For example, consider a LVDM particle with $b = 1$ in the halo of the Milky Way galaxy, for which $\sigma_{\rm s} \equiv r_{\rm s}/r \sim 10^{-5}\,{\rm kpc}/10\,{\rm kpc} = 10^{-6}$. The maximum velocity corresponding to negative total energy (4.26) for this choice of parameters is plotted in Fig. 3. Notice that $u_0 = 1/\sqrt{2}$ and $\gamma_0 = \sqrt{2}$ so that (4.27) and (4.28) may be expressed simply as (with $\sigma_{\rm s} \approx 5 \times 10^{-6}$)

$$0 \leq (mc^2)^{-1} p_{\rm max} < \sqrt{2}\sigma_{\rm s} - \sigma_{\rm s}^2, \tag{4.29}$$

$$1/\sqrt{2} \leq u_{\rm max} < 1/\sqrt{2} + \sigma_{\rm s}/2, \tag{4.30}$$

over an entire reasonably chosen range of orbital radius: $10\,{\rm kpc} \leq r \leq 100\,{\rm kpc}$. For this choice of parameters the LVDM particle is constrained to a very narrow range of velocities if it is to remain bound. For any choice of parameters the particle is constrained from below due to the minimum velocity imposed by Lorentz-violation, v_0, and from above due to the finite mass of the galaxy. The range of allowed velocities may be increased by choosing a larger value for b (smaller value for v_0).

In the limit that $b \to \infty$ ($v_0 \to 0$ and $\gamma_0 \to 1$) a similar model for relativistic particles is recovered. Consider standard relativistic dark matter (SRDM) in orbit about a central mass to be described by:

$$E = mc^2(\gamma - 1) - GMm/r. \tag{4.31}$$

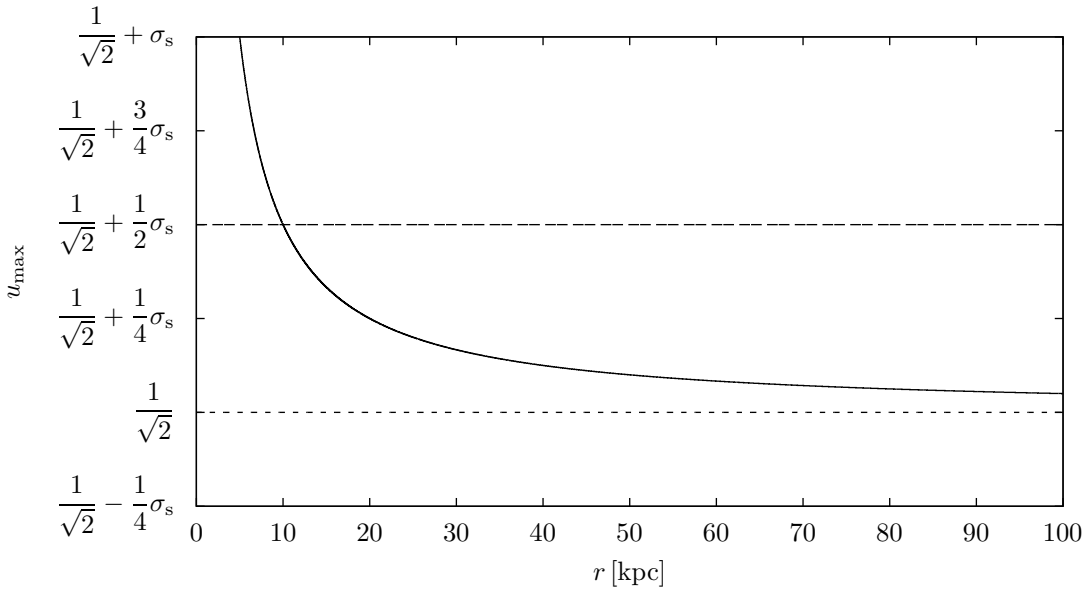

Fig. 3. Maximum velocity corresponding to negative total energy as a function of radial coordinate (4.26). ($\sigma_s = 5 \times 10^{-6}$.) The lower horizontal line (short dashes) marks the minimum velocity allowed for the example LVDM model in which $b = 2m/\overline{m} = 1$, corresponding to $u_0 = 1/\sqrt{2}$ and $\gamma_0 = \sqrt{2}$. The upper horizontal line (long dashes) corresponds to $r = 10\,\mathrm{kpc}$. The particle is assumed to be orbiting a central mass equivalent to that of the Milky Way galaxy, for which $r_s \approx 5 \times 10^{-5}\,\mathrm{kpc}$. In this case, the particle is constrained to a very narrow range of velocities if it is to remain bound. For any choice of parameters the LVDM particle is constrained from below due to the minimum velocity imposed by Lorentz-violation, v_0, and from above due to the finite mass of the galaxy. The range of allowed velocities may be increased by choosing a smaller value for v_0 (larger value for b).

For bound states, the total energy must be negative:

$$-r_s/r \leq (mc^2)^{-1}E < 0, \tag{4.32}$$

as in (4.24). The maximum velocity $u_{\mathrm{max}}^{\mathrm{SRDM}} = v_{\mathrm{max}}^{\mathrm{SRDM}}/c$ may be calculated by setting

the total energy (4.31) equal to zero, resulting in

$$u_{\max}^{\text{SRDM}} = \left[1 - (1 + r_{\text{s}}/r)^{-2}\right]^{1/2}. \tag{4.33}$$

Expanding in r_{s}/r, the range of the maximum velocity may be expressed as

$$0 \leq u_{\max}^{\text{SRDM}} < 2\left(\frac{r_{\text{s}}}{2r}\right)^{1/2} - 3\left(\frac{r_{\text{s}}}{2r}\right)^{3/2}. \tag{4.34}$$

For a SRDM particle orbiting the Milky Way galaxy, this may be expressed as

$$0 \leq u_{\max}^{\text{SRDM}} \lesssim \sigma_{\text{s}}^{1/2} - \sigma_{\text{s}}^{3/2}, \tag{4.35}$$

where σ_{s} is defined in the example leading to (4.30). (The result for nonrelativistic cold dark matter is recovered if the $\sigma_{\text{s}}^{3/2} \sim 10^{-10}$ term is ignored.) When compared to the example LVDM model, the constraint on the particle velocity from below is removed, and the constraint from above is relaxed, thereby widening the range of maximum velocities by three orders of magnitude. This emphasizes the narrow range of allowed velocities for the example LVDM model.

C. Effective Potential

A Lagrangian may be defined as $\mathcal{L} = T - U$:

$$\mathcal{L} = mc^2(\gamma - \gamma_0) + GMm/r, \tag{4.36}$$

where the kinetic energy is given by (4.22) and the gravitational potential energy is that of a central mass. The conserved angular momentum is found from Lagrange's equation,

$$\frac{\mathrm{d}}{\mathrm{d}t}\left(\frac{\partial \mathcal{L}}{\partial \dot{\varphi}}\right) - \frac{\partial \mathcal{L}}{\partial \varphi} = 0 \quad \Longrightarrow \quad \frac{\mathrm{d}}{\mathrm{d}t}\left(\gamma^3 m r^2 \dot{\varphi}\right) = 0. \tag{4.37}$$

Then $\ell \equiv \gamma^3 m r^2 \dot{\varphi}$ may be used to eliminate $\dot{\varphi}$ in the effective force: $F_{\rm e} \equiv F_r + p_\varphi \dot{\varphi}$. Due to the nonstandard momentum-velocity relation of LVDM,

$$\mathbf{p}/p = \dot{\mathbf{r}}/v \quad \Longrightarrow \quad p_\varphi \dot{\varphi} = \frac{r\dot{\varphi}}{v} p(v; v_0) \dot{\varphi}, \tag{4.38}$$

where $p(v; v_0) = \gamma m v - \gamma_0 m v_0$, or, after eliminating $\dot{\varphi}$:

$$p_\varphi \dot{\varphi} = \frac{\ell^2}{m r^3} \left(\gamma^{-6} m^{-1} v^{-1} p \right). \tag{4.39}$$

As described in the example in the previous section ((4.28), (4.30), and Fig. 3), LVDM is constrained to move with velocity very near the minimum velocity ($v \approx v_0$), so that we may expand about v_0: $\gamma^{-6} m^{-1} v^{-1} p \approx \gamma_0^{-4} v_0^{-1} (v - v_0)$. Assuming $r\dot{\varphi} \gg \dot{r}$, we may use the first-order approximations summarized in (4.21) to eliminate $v - v_0$: $v - v_0 \approx \gamma_0^{-3} v_0^{-2} c^3 r_{\rm c}^{-1} r_{\rm s}$, where $r_{\rm c}$ is a characteristic galactic distance (kiloparsecs), so that $\gamma^{-6} m^{-1} v^{-1} p \approx \gamma_0^{-7} u_0^{-3} r_{\rm c}^{-1} r_{\rm s}$. (Recall: $u_0 \equiv v_0/c$.) Because $v \approx v_0$, we may take $\gamma \approx \gamma_0$ so that $\ell \approx \gamma_0^3 r_{\rm c} v_0$, where we have assumed $r\dot{\varphi} \gg \dot{r}$ in this definition of the angular momentum. The effective force may now be expressed as (with $F_r = -GMm/r^2$)

$$F_{\rm e} \approx -mc^2 \cdot \frac{r_{\rm s}}{r^2} + mc^2 \cdot \frac{r_{\rm s} r_{\rm c}}{r^3} \cdot \gamma_0^{-1} u_0^{-1}. \tag{4.40}$$

The effective potential $V \equiv (mc^2)^{-1} U_{\rm e}$ follows immediately:

$$V \approx -\frac{r_{\rm s}}{r} + \frac{r_{\rm s} r_{\rm c}}{2r^2} \cdot \gamma_0^{-1} u_0^{-1}. \tag{4.41}$$

If the scaling $\overline{V} = \gamma_0^{-1} u_0^{-1} (r_{\rm c}/r_{\rm s}) V$ is applied, then

$$\overline{V} = -\frac{1}{\bar{r}} + \frac{1}{2\bar{r}^2}, \tag{4.42}$$

where $\bar{r} \equiv \gamma_0 u_0 r_{\rm c}^{-1} r$, and it becomes apparent that LVDM would reside in a larger volume than CDM. A similar treatment for CDM again results in (4.42), but with

the scalings: $\overline{V}_{\rm CDM} = (r_{\rm c}/r_{\rm s})V_{\rm CDM}$ and $\bar{r}_{\rm CDM} \equiv r_{\rm c}^{-1} r$.

The natural scalings for LVDM suggest both a suppressed effective potential and enlarged radial coordinate, when compared to a similar treatment for CDM. Notice that $\overline{V}/V \sim \gamma_0^{-1}$, so that the LVDM scaled effective potential is small due to the limiting behavior: $\gamma_0^{-1} \to 0$ as $u_0 \to 1$. Also, $\bar{r}/r \sim \gamma_0$, so that the LVDM scaled radial coordinate is large due to the limiting behavior: $\gamma_0 \to \infty$ as $u_0 \to 1$. Indeed, the effects are enormous as $u_0 \to 1$.

D. Discussion

This initial inspection of the problem results in a clear prediction of reduced binding, as expressed in (4.10), (4.20), and (4.21). On the other hand, the constraints on orbital velocites expressed in (4.28), (4.30), and in Fig. 3, and the scaled effective potential (4.42) indicate that LVDM may not be stable on galactic scales. In all of these initial calculations approximations are made assuming $b \sim 1$ ($v_0/c \lesssim 1$ and $\gamma_0 \gtrsim 1$) because it is a convenient choice – allowing for an initial impression as to the nature of LVDM. The fact that many of these initial results do not reduce to those of CDM in the appropriate limit is a hint that the chosen parameter space results in a LVDM which is very different than CDM. However, these initial calculations indicate that LVDM is likely to be less bound and occupy a larger volume than CDM, suggesting a possible solution to the overdensity and cusp problems outlined in the previous chapter.

A detailed analysis revealing the relevant parameter space was carried out in the context of two different models: (1) an empirical model density profile as reported in Chapter V, and (2) a central-mass model as reported in Chapter VI. In Chapter VII, it is then understood that the relevant parameter space has already been established, and a Lagrangian formulation of LVDM dynamics is developed.

It should be mentioned that the Lagrangian defined in (4.36) is not as broadly useful as the effective Lagrangian which will be defined in Chapter VII. This effective Lagrangian results in more precise, and in principle observable, predictions concerning the dynamics of LVDM.

CHAPTER V

MODEL DENSITY PROFILE

A model density profile will now be constructed, resulting in scalable galactic rotation curves for both cold dark matter and Lorentz-violating dark matter. Consider four regions with boundaries $0 \leq r_{\mathrm{c}} \leq r_{\mathrm{d}} \leq r_{\mathrm{h}}$, where $r_{\mathrm{c}} = 1\,\mathrm{kpc}$ is an inner cutoff radius, $r_{\mathrm{d}} = 10\,\mathrm{kpc}$ is the radius of the disk component, and $r_{\mathrm{h}} = 100\,\mathrm{kpc}$ is the radius of the halo component. Consider the matter density to be a superposition of baryonic and nonbaryonic matter densities. The baryonic matter density is taken to be constant. This baryonic matter is restricted to the disk:

$$\rho_{\mathrm{b}}(r) = \frac{m_{\mathrm{b}}}{\frac{4}{3}\pi r_{\mathrm{d}}^3}, \quad 0 \leq r \leq r_{\mathrm{d}}, \tag{5.1}$$

where m_{b} is the total baryonic matter in the disk. The nonbaryonic matter density is taken to reach well within the baryonic disk, but with no nonbaryonic matter inside the cutoff radius, r_{c}. This cutoff radius is defined to ensure a finite gravitational potential, and represents the maximum resolution of the model near the galactic center. This nonbaryonic matter is taken to be confined to the region $r_{\mathrm{c}} \leq r \leq r_{\mathrm{h}}$:

$$m_{\mathrm{nb}}(r) = \lambda(r - r_{\mathrm{c}}), \quad \text{and} \quad \rho_{\mathrm{nb}}(r) = \frac{1}{4\pi r^2}\frac{\mathrm{d}m_{\mathrm{nb}}}{\mathrm{d}r} = \frac{\lambda}{4\pi r^2}. \tag{5.2}$$

The total nonbaryonic matter is $M_{\mathrm{nb}} = \lambda(r_{\mathrm{h}} - r_{\mathrm{c}})$, so that

$$\lambda = \frac{M_{\mathrm{nb}}}{r_{\mathrm{h}}}\left(1 - \frac{r_{\mathrm{c}}}{r_{\mathrm{h}}}\right)^{-1}. \tag{5.3}$$

The total matter density is thus given over four regions by:

$$\rho(r) = \begin{cases} \rho_{\rm b}, & 0 \le r \le r_{\rm c}, \\ \dfrac{\lambda}{4\pi r^2} + \rho_{\rm b}, & r_{\rm c} \le r \le r_{\rm d}, \\ \dfrac{\lambda}{4\pi r^2}, & r_{\rm d} \le r \le r_{\rm h}, \\ 0, & r > r_{\rm h}. \end{cases} \tag{5.4}$$

Figure 4 illustrates the superposition (top) of nonbaryonic and baryonic matter. The nonbaryonic (bottom left) and baryonic (bottom right) components are also displayed. The nonbaryonic matter is confined to the interval $r_{\rm c} \le r \le r_{\rm d}$, where $r_{\rm c}$ is a cutoff radius, and has a density which declines like $\rho_{\rm nb} \sim r^{-2}$. The baryonic matter is confined to the interval $0 \le r \le r_{\rm d}$, and has constant density. Superposition of (green) nonbaryonic and (white) baryonic components results in four distinct regions (top): (1) The gray circle in the center has radius $r_{\rm c} = 1\,{\rm kpc}$ and represents the (black) absence of matter superposed with low-density baryonic matter. (2) The low-density baryonic matter extends outward to $r_{\rm d} = 10\,{\rm kpc}$ with constant density, $\rho_{\rm b}$, and represents the galactic disk. Nonbaryonic and baryonic matter are superposed in the (light-green) region $r_{\rm c} \le r \le r_{\rm d}$, wherein the nonbaryonic matter density declines like $\rho_{\rm nb} \sim r^{-2}$. (3) Though the nonbaryonic matter density continues to decline, $M_{\rm nb} \approx 100\, m_{\rm b}$ so that dark matter extends well beyond the disk to the halo radius, $r_{\rm h} = 100\,{\rm kpc}$, (4), beyond which no matter exists. (As noted in the figure, distances are not to scale.)

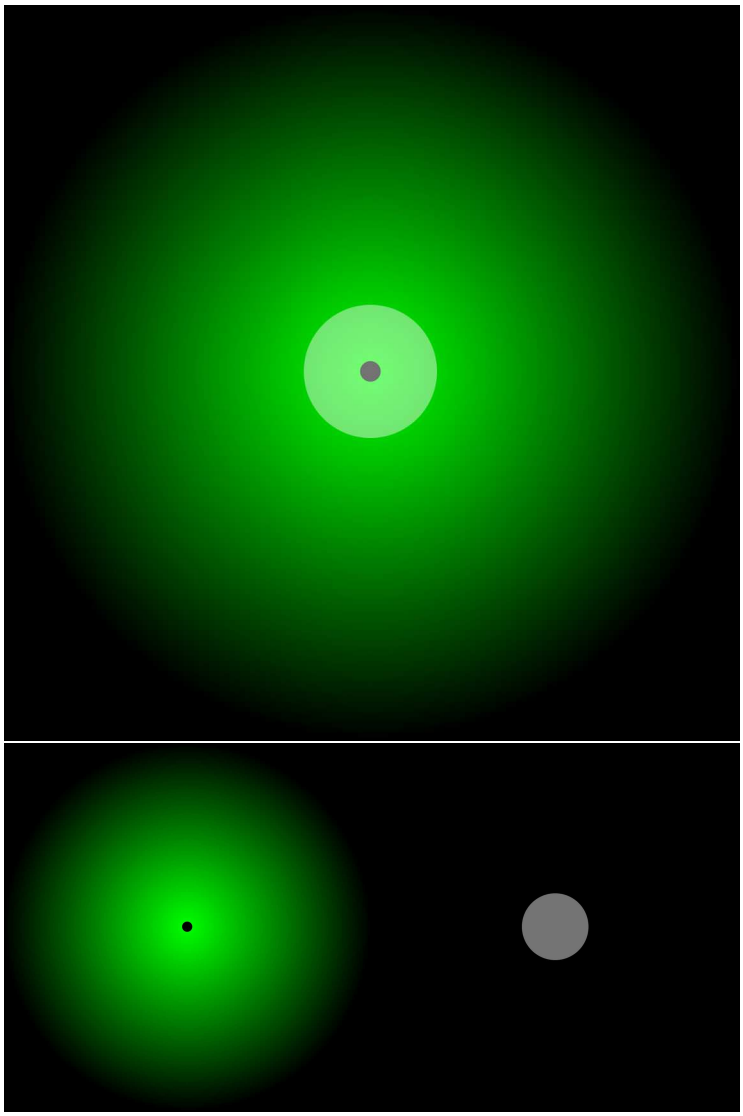

Fig. 4. Graphical representation of the model density profile in which the galactic matter density (top) is the superposition of nonbaryonic (bottom left) and baryonic (bottom right) matter densities. In the colored version of this figure, green and white represent nonbaryonic and baryonic matter, respectively. The baryonic matter density is taken to be $\rho_{\rm b} \sim m_{\rm b}/r_{\rm d}^3$ over the interval $0 \leq r \leq r_{\rm d}$, and zero thereafter. The nonbaryonic matter density varies as $\rho_{\rm nb} \sim r^{-2}$ over the interval $r_{\rm c} \leq r \leq r_{\rm h}$, where $r_{\rm c} = 1\,{\rm kpc}$ is an inner cutoff radius, and is zero elsewhere. (Distances are not to scale. The correct scale corresponds to $r_{\rm h}/r_{\rm c} \gtrsim 10^2$ and $r_{\rm h}/r_{\rm d} \gtrsim 10$.)

A. Gravitational Field and Rotation Curves

The gravitational field is found using Gauss' law, $\oint \boldsymbol{g} \cdot \mathrm{d}\boldsymbol{A} = -4\pi G \int \rho \, \mathrm{d}V$:

$$g(r) = \begin{cases} -\left(\dfrac{Gm_{\mathrm{b}}}{r_{\mathrm{d}}^3}\right) r, & 0 \le r \le r_{\mathrm{c}}, \\ -\dfrac{G\lambda}{r}\left(1 - \dfrac{r_{\mathrm{c}}}{r}\right) - \left(\dfrac{Gm_{\mathrm{b}}}{r_{\mathrm{d}}^3}\right) r, & r_{\mathrm{c}} \le r \le r_{\mathrm{d}}, \\ -\dfrac{G\lambda}{r}\left(1 - \dfrac{r_{\mathrm{c}}}{r}\right) - \dfrac{Gm_{\mathrm{b}}}{r^2}, & r_{\mathrm{d}} \le r \le r_{\mathrm{h}}, \\ -\dfrac{GM_{\mathrm{g}}}{r^2}, & r > r_{\mathrm{h}}, \end{cases} \tag{5.5}$$

where $M_{\mathrm{g}} = M_{\mathrm{nb}} + m_{\mathrm{b}}$ is the mass of the galaxy. The ratio of baryonic matter to nonbaryonic matter is fixed using observed galactic rotation curves of neutral hydrogen clouds near the edge of the disk. Consider a hydrogen cloud in a circular orbit of radius equal to the radius of the disk. Then $p_{\mathrm{H}} v_{\mathrm{H}} / r_{\mathrm{d}} = m_{\mathrm{H}} g(r_{\mathrm{d}})$, so that together with (5.3) we have

$$\frac{v_{\mathrm{H}}^2}{G} = \frac{M_{\mathrm{nb}}}{r_{\mathrm{h}}} \left(1 - \frac{r_{\mathrm{c}}}{r_{\mathrm{h}}}\right)^{-1} \left(1 - \frac{r_{\mathrm{c}}}{r_{\mathrm{d}}}\right) + \frac{m_{\mathrm{b}}}{r_{\mathrm{d}}}. \tag{5.6}$$

Observations indicate that speeds of hydrogen clouds orbiting beyond the edge of the galactic disk remain constant for orbital radii extending up to and beyond 100 kpc. Then, $p_{\mathrm{H}} v_{\mathrm{H}} / r_{\mathrm{h}} \approx m_{\mathrm{H}} g(r_{\mathrm{h}})$, so that

$$\frac{v_{\mathrm{H}}^2}{G} \approx \frac{M_{\mathrm{nb}}}{r_{\mathrm{h}}} + \frac{m_{\mathrm{b}}}{r_{\mathrm{h}}}. \tag{5.7}$$

Equations (5.6) and (5.7) may be solved simultaneously for M_{nb} and m_{b}. Neglecting $r_{\mathrm{c}}/r_{\mathrm{h}}$ when compared to $r_{\mathrm{c}}/r_{\mathrm{d}}$ and $r_{\mathrm{d}}/r_{\mathrm{h}}$, and neglecting $m_{\mathrm{b}}/r_{\mathrm{h}}$ when compared to

$m_{\rm b}/r_{\rm d}$ and $M_{\rm nb}/r_{\rm h}$, we find

$$M_{\rm nb} \approx \left(\frac{v_{\rm H}^2}{G}\right) r_{\rm h} \approx 10^{12} m_\odot \quad \text{and} \quad \frac{m_{\rm b}}{M_{\rm nb}} \approx \frac{r_{\rm c}}{r_{\rm h}} = 10^{-2}, \tag{5.8}$$

where $v_{\rm H} = 225\,{\rm km/s}$ is the speed of hydrogen clouds in the halo of the Milky Way galaxy and $m_\odot = 1.99 \times 10^{30}\,{\rm kg}$ is the mass of the Sun. The mass parameter, λ, is estimated to be

$$\lambda = \frac{M_{\rm nb}}{r_{\rm h}} \left(1 - \frac{r_{\rm c}}{r_{\rm h}}\right)^{-1} \approx \frac{v_{\rm H}^2}{G} \approx 10^{10}\, m_\odot/{\rm kpc}. \tag{5.9}$$

The resulting rotation curves for hydrogen clouds or CDM particles are derived using (5.5). Then, $pv/r = mg(r)$ so that

$$v(r) = \begin{cases} \left(\dfrac{G m_{\rm b}}{r_{\rm d}^3}\right)^{1/2} r, & 0 \le r \le r_{\rm c}, \\ \left[G\lambda\left(1 - \dfrac{r_{\rm c}}{r}\right) + \left(\dfrac{G m_{\rm b}}{r_{\rm d}^3}\right) r^2\right]^{1/2}, & r_{\rm c} \le r \le r_{\rm d}, \\ \left[G\lambda\left(1 - \dfrac{r_{\rm c}}{r}\right) + \dfrac{G m_{\rm b}}{r}\right]^{1/2}, & r_{\rm d} \le r \le r_{\rm h}. \end{cases} \tag{5.10}$$

Using (5.8) and (5.9), (5.10) may be expressed as

$$v(r) \approx \begin{cases} v_{\rm H}\left(r_{\rm c}/r_{\rm d}\right)^{3/2} (r/r_{\rm c})\,, & 0 \le r \le r_{\rm c}, \\ v_{\rm H}\sqrt{r g_2(r)}, & r_{\rm c} \le r \le r_{\rm d}, \\ v_{\rm H}, & r_{\rm d} \le r \le r_{\rm h}, \end{cases} \tag{5.11}$$

where $v_{\rm H} = 225\,{\rm km/s}$, and

$$r g_2(r) \equiv 1 - r_{\rm c}/r + (r_{\rm c}/r_{\rm d})^3 (r/r_{\rm c})^2. \tag{5.12}$$

The orbital speed is plotted for the region $r_{\rm c} \le r \le r_{\rm d}$ in Fig. 5. The resulting rotation curve has, by construction, general characteristics similar to those measured from

21 cm lines of neutral hydrogen in the galactic halo. That is, $v(r) \sim r$ for small radii, and $v(r) \approx v_{\text{H}}$ for large radii. Notice that (5.8) together with an appropriate choice of $r_{\text{c}}/r_{\text{d}}$ results in a scalable model described by (5.11) and (5.12).

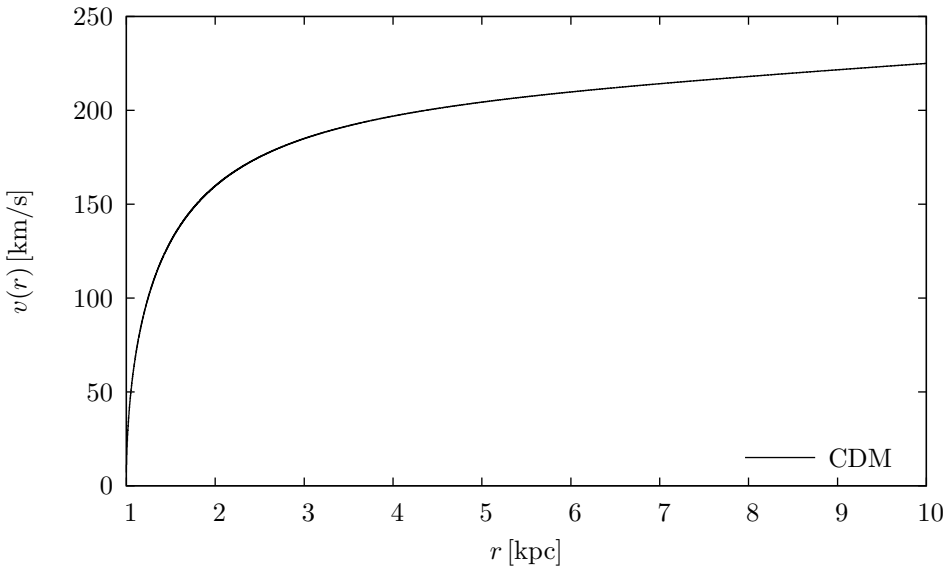

Fig. 5. Orbital speed of hydrogen cloud or CDM particle in circular orbit of radius r, as predicted by the model density profile and resulting gravitational field. See (5.11), with $r_{\text{c}} \leq r \leq r_{\text{d}}$, for which the parameters are taken to be $r_{\text{d}} = 10\,\text{kpc}$, $r_{\text{c}} = 1\,\text{kpc}$, and $v_{\text{H}} = 225\,\text{km/s}$.

Rotation curves can also be derived for LVDM under the influence of an identical gravitational field (5.5). Recall that $p(v) = \gamma m v - \gamma_0 m v_0$ for LVDM particles. Then $pv/r = mg(r)$, so that

$$\big(\gamma(v)v - \gamma(v_0)v_0\big)\, v = G\lambda\left(1 - \frac{r_{\text{c}}}{r}\right) - \left(\frac{Gm_{\text{b}}}{r_{\text{d}}^3}\right) r^2, \quad r_{\text{c}} \leq r \leq r_{\text{d}}, \tag{5.13}$$

which is quartic in $v(r)$. For purposes of numerical computation, this may be expressed as

$$\phi(u, u_0) \approx u_{\text{H}}^2 r g_2(r), \tag{5.14}$$

where $u = v/c$, $u_{\rm H} = v_{\rm H}/c$, and

$$\phi(u, u_0) \equiv \big(\gamma(u)u - \gamma(u_0)u_0\big)\, u. \tag{5.15}$$

Numerical solutions to (5.14) are provided in Fig. 6 for several large values of $m/\overline{m}$, which result in LVDM rotation curves of about the same magnitude as those for CDM. The minimum velocity, $u_0 = 1/\sqrt{1 + (2m/\overline{m})^2}$, may be considered a small perturbation to CDM for $m/\overline{m} \gtrsim 10^4$. Larger values of $m/\overline{m}$ result in rotation curves that are almost indistinguishable from those of CDM. A curve representing the orbital speed of a CDM particle would be indistinguishable from the bottom (red) curve, for which $m/\overline{m} = 10^6$. For $m/\overline{m} \lesssim 10^3$, rotational velocities are very large. The relative error

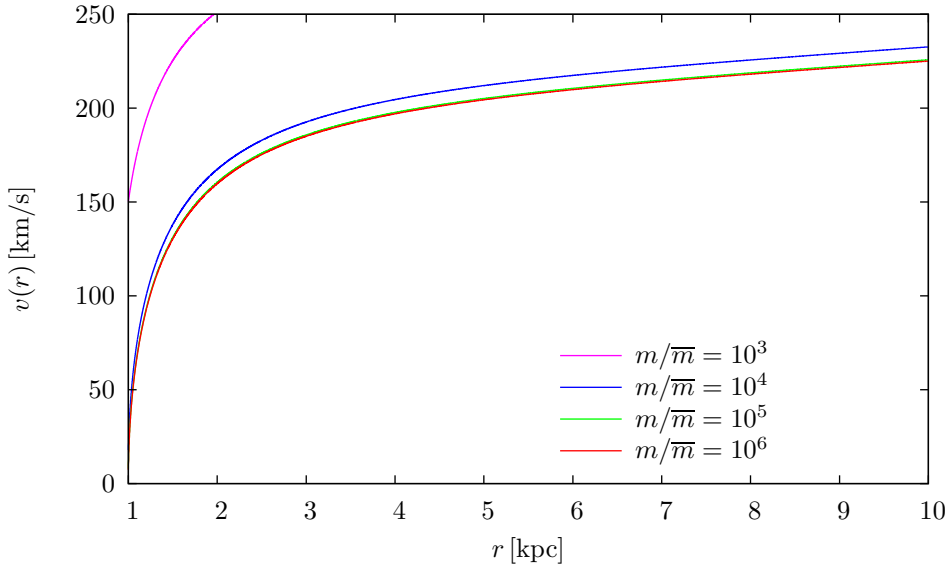

Fig. 6. Orbital speed of LVDM particle in circular orbit of radius r, as predicted by the model density profile and resulting gravitational field. Numerical solutions to (5.14) are presented for values of $m/\overline{m}$ which result in LVDM rotation curves comparable in magnitude to those of CDM. A curve representing the orbital speed of a CDM particle would be indistinguishable (on this scale) from the bottom (red) curve, for which $m/\overline{m} = 10^6$.

in the numerical solution of (5.14) may be expressed as:

$$\frac{\delta\bar{\phi}}{\bar{\phi}_r} \equiv \frac{\bar{\phi}_r - \bar{\phi}_u}{\bar{\phi}_r}, \tag{5.16}$$

where $\bar{\phi}_r \equiv r g_2(r)$ and $\bar{\phi}_u \equiv \phi(u)/u_{\rm H}^2$ are the exact and approximate values of $\phi/u_{\rm H}^2$ at galactic radius $r_{\rm c} \leq r \leq r_{\rm d}$, respectively. Then,

$$\frac{\delta\bar{\phi}}{\bar{\phi}_r} = 2\frac{\delta u}{u}\left[1 + \frac{u}{2\bar{\phi}_r}\left(\gamma_0 u_0 + \gamma^3 u^3\right)\right], \tag{5.17}$$

so that

$$\frac{\delta u}{u} = \frac{1}{2}\frac{\delta\bar{\phi}}{\bar{\phi}_r}\left(1+\epsilon\right)^{-1}, \tag{5.18}$$

where $\epsilon \equiv \dfrac{u}{2\bar{\phi}_r}\left(\gamma_0 u_0 + \gamma^3 u^3\right)$ is a small correction: $u_0^2 \leq \epsilon \leq u_{\rm H} u_0 \left(r_{\rm c}/r_{\rm d}\right)^{-3}$. The relative error for each curve in Fig. 6 is $\delta u/u \sim \delta\bar{\phi}/\bar{\phi}_r \sim 10^{-6}$. The relative error (5.18) for the case in which $m/\overline{m} = 10^4$ is plotted in Fig. 7. The radius r corresponding to each value of u is included along the top border of the figure.

Approximate analytical solutions to (5.14) are found to be just as accurate. For LVDM particles bound on galactic scales, u is small when compared to unity, and $u_0 \leq u$, so that u_0 is also small when compared to unity. Then (5.15) may be expressed as:

$$\phi(u,u_0) = u\sum_{\rm n=0}^{\infty}(-1)^{\rm n}\binom{-\frac{1}{2}}{\rm n}\left(u^{2{\rm n}+1} - u_0^{2{\rm n}+1}\right), \tag{5.19}$$

$$= u\left[(u-u_0) + \tfrac{1}{2}(u^3-u_0^3) + \tfrac{3}{8}(u^5-u_0^5) + \cdots\right], \tag{5.20}$$

$$\approx u(u-u_0), \tag{5.21}$$

where $\binom{\rm m}{\rm n}$ is the binomial coefficient. It is a reasonable approximation to keep only

the first order term in this expansion (5.21), which may then be rewritten as:

$$\phi(u, u_0) \approx u(u - u_0) = u_0(u - u_0) + (u - u_0)^2. \tag{5.22}$$

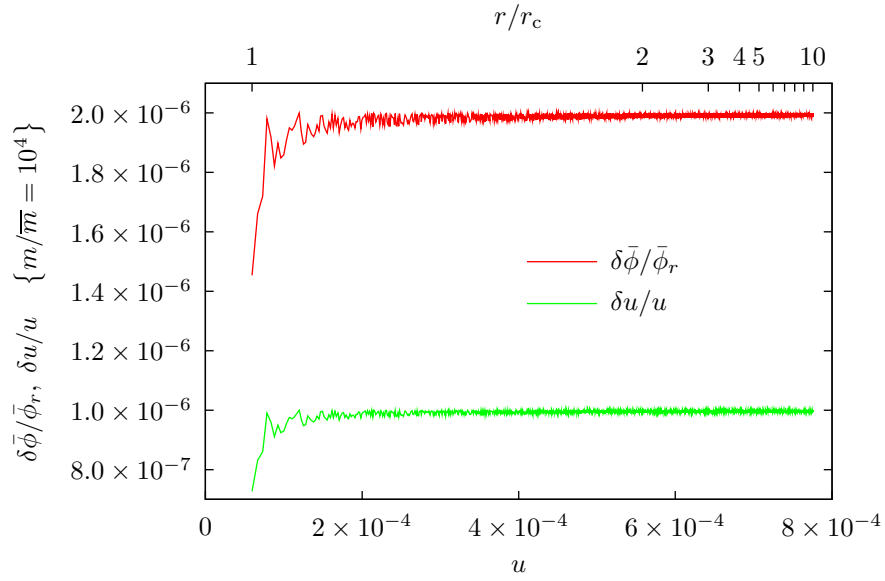

Fig. 7. Relative error in the rotation curve of Fig. 6 corresponding to $m/\overline{m} = 10^4$. The radius, r, corresponding to each value of u is included along the top border. This curve is representative of the relative error for each rotation curve in Fig. 6: $\delta u/u \sim \delta\bar{\phi}/\bar{\phi}_r \sim 10^{-6}$ for $m/\overline{m} = 10^3,\ 10^4,\ 10^5,\ 10^6$.

Alternatively, because LVDM particles are constrained to move with speeds very near the minimum speed ((4.28), (4.30), and Fig. 3), (5.22) may be thought of as arising from further expanding (5.20) in powers of $u - u_0$:

$$\begin{aligned}
\phi(u, u_0) &\approx u_0\,(u - u_0) + (u - u_0)^2 + 2u_0\,(u - u_0)^3 + \tfrac{1}{2}\,(u - u_0)^4 + \cdots \\
&\approx u_0\,(u - u_0)\left[1 + 2\,(u - u_0)^2 + \mathcal{O}(u - u_0)^4\right] \\
&\quad + (u - u_0)^2\left[1 + \tfrac{1}{2}\,(u - u_0)^2 + \mathcal{O}(u - u_0)^4\right], \\
&\approx u_0\,(u - u_0) + (u - u_0)^2,
\end{aligned} \tag{5.23}$$

where u_0 and $u - u_0$ are taken to be of equal order. Formally, $\phi(u, u_0)$, as given in

(5.14), is expanded to second order about the point $(0,0)$, resulting in:

$$\phi(u,u_0) \approx \frac{1}{2}\left[\phi_{uu}(0,0)u^2 + 2\phi_{uu_0}(0,0)uu_0\right] \tag{5.24}$$

$$\approx \frac{1}{2}\left[2u^2 + 2(-1)uu_0\right], \tag{5.25}$$

again leading to (5.22). This approximation is accurate in all regions centered on $(u-u_0) \sim u_0$ so that (5.14) may be approximated as

$$\phi_1(u,u_0) + \phi_2(u,u_0) \approx u_{\rm H}^2 r g_2(r), \tag{5.26}$$

where $\phi_1(u,u_0) \equiv u_0(u-u_0)$ and $\phi_2(u,u_0) \equiv (u-u_0)^2$. The accuracy of this approximation is displayed in Fig. 8, in which $\bar{\phi}_1 = \phi_1/u_{\rm H}^2$ and $\bar{\phi}_2 = \phi_2/u_{\rm H}^2$ are plotted separately against u_0, subject to $\bar{\phi}_1 + \bar{\phi}_2 = r g_2(r)$ for $r = 1\,\mathrm{kpc}$ and $r = 10\,\mathrm{kpc}$. The intersecting magenta and blue curves correspond to $r = 10\,\mathrm{kpc}$, for which $\bar{\phi}_1 + \bar{\phi}_2 = 1$. The intersecting green and red curves correspond to $r = 1\,\mathrm{kpc}$, for which $\bar{\phi}_1 + \bar{\phi}_2 = 10^{-3}$. The black curve displays the points of intersection, for which $\bar{\phi}_1 = \bar{\phi}_2 = r g_2(r)/2$, over the entire range $1 \le r/r_{\rm c} \le 10$. This intersection curve corresponds to $u_0^* = u - u_0^*$, or $u = 2u_0^*$, so that $\bar{\phi}_1 = \bar{\phi}_2 = (u_0^*/u_{\rm H})^2$. Then, for a given radial distance, $u_0^* = u_{\rm H}\sqrt{r g_2(r)/2}$ defines a crossover point. For example, $u_0^* = (r_{\rm c}/r_{\rm d})^{3/2} u_{\rm H}/\sqrt{2} \approx 2\times 10^{-5}$ $(m/\overline{m} \approx 3\times 10^4)$ for $r/r_{\rm c} = 1$, and $u_0^* = u_{\rm H}/\sqrt{2} \approx 5\times 10^{-4}$ $(m/\overline{m} \approx 10^3)$ for $r/r_{\rm c} = 10$. In the region $u_0 \ll u_0^*$, $\bar{\phi}_1 \ll \bar{\phi}_2$, and in the region $u_0 \gg u_0^*$, $\bar{\phi}_2 \ll \bar{\phi}_1$.

Equivalently, the regions divided by u_0^* may be described in terms of the relative magnitudes of v_0 and $v - v_0$. In the region defined by $v_0 \ll v - v_0$, (5.26) may be expressed as $(v-v_0)^2 \approx v_{\rm H}^2 r g_2(r)$, so that

$$v(r) \approx v_{\rm H}\sqrt{r g_2(r)} + v_0, \quad v_0 \ll v - v_0, \tag{5.27}$$

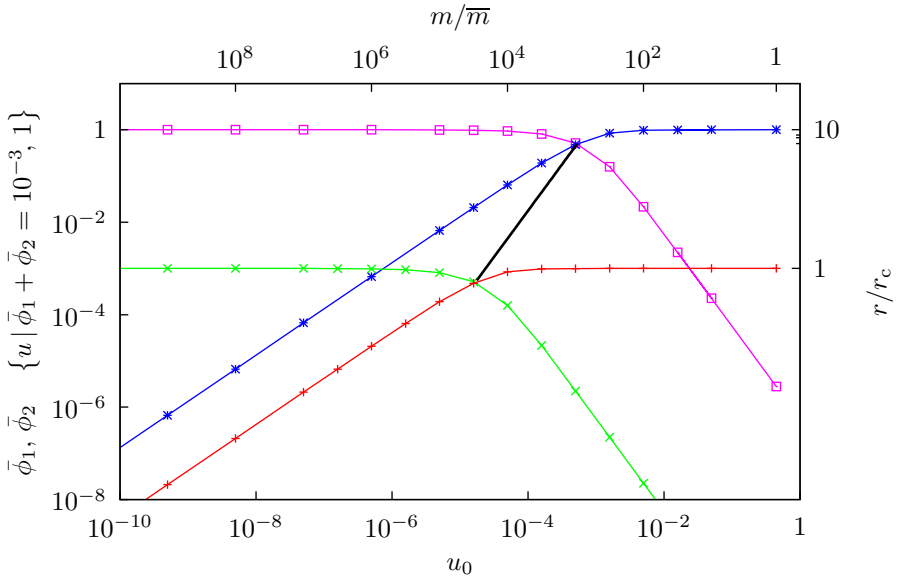

Fig. 8. The accuracy of (5.26) is displayed by plotting $\bar{\phi}_1 = \phi_1/u_{\rm H}^2$ and $\bar{\phi}_2 = \phi_2/u_{\rm H}^2$ separately against u_0, subject to $\bar{\phi}_1 + \bar{\phi}_2 = rg_2(r)$ for $r = 10\,\text{kpc}$ (upper, intersecting magenta and blue curves) and $r = 1\,\text{kpc}$ (lower, intersecting green and red curves). The points of intersection, for which $\bar{\phi}_1 = \bar{\phi}_2 = rg_2(r)/2$, are plotted (black curve) for the entire range $1 \leq r/r_{\rm c} \leq 10$, and serve as points of reference – to the left of which $\bar{\phi}_2$ is dominant (magenta and green, horizontal curves), and to the right of which $\bar{\phi}_1$ is dominant (blue and red, horizontal curves). From these results, in conjunction with detailed analysis given in the text, it is evident that (5.26) is an accurate, approximate analytical solution to (5.14). In addition, further simplifications may be made in regions for which either $\bar{\phi}_1$ or $\bar{\phi}_2$ is dominant.

or $v_{\rm LVDM} = v_{\rm CDM} + v_0$, where $v_{\rm CDM} = v_{\rm H}\sqrt{rg_2(r)}$. (Recall (5.11), $r_{\rm c} \leq r \leq r_{\rm d}$.) Then,

$$v_{\rm LVDM}(r) \xrightarrow[m/\overline{m}\to\infty]{v_0\to 0} v_{\rm CDM}(r), \tag{5.28}$$

as expected; CDM rotation curves represent the lower limit of LVDM rotation curves. In the region defined by $v_0 \gg v - v_0$, (5.26) may instead be expressed as $v_0\,(v - v_0) \approx v_{\rm H}^2 rg_2(r)$, so that

$$v(r) \approx v_0 + v_{\text{H}}^2 r g_2(r)/v_0, \quad v_0 \gg v - v_0, \tag{5.29}$$

or $v_{\text{LVDM}} = v_0 + v_{\text{CDM}}^2/v_0$. Then,

$$v_{\text{LVDM}}(r) \xrightarrow[m/\overline{m}\to 0]{v_0 \to c} v_0 \tag{5.30}$$

represents the upper limit of LVDM rotation curves. In the crossover region, wherein $v_0 \sim v - v_0$, (5.26) must be solved without further approximation, resulting in $(v - v_0)^2 + v_0(v - v_0) \approx v_{\text{H}}^2 r g_2(r)$. Then,

$$v(r) \approx v_0 + \frac{1}{2}\left(\sqrt{v_0^2 + 4v_{\text{H}}^2 r g_2(r)} - v_0\right), \quad v_0 \sim v - v_0. \tag{5.31}$$

This approximation is plotted in Fig. 9 along with numerical solutions to (5.14).

In summary, (5.14) is accurately approximated as:

$$v_{\text{H}}^2 r g_2(r) \approx \begin{cases} v_0\,(v - v_0)\,, & v - v_0 \ll v_0, \\ v_0\,(v - v_0) + (v - v_0)^2, & v - v_0 \sim v_0, \\ (v - v_0)^2, & v - v_0 \gg v_0. \end{cases} \tag{5.32}$$

and the solutions are:

$$v(r) \approx \begin{cases} v_0 + v_{\text{H}}^2 r g_2(r)/v_0, & v - v_0 \ll v_0, \\ v_0 + \frac{1}{2}\left(\sqrt{v_0^2 + 4v_{\text{H}}^2 r g_2(r)} - v_0\right), & v - v_0 \sim v_0, \\ v_{\text{H}}\sqrt{r g_2(r)} + v_0, & v - v_0 \gg v_0. \end{cases} \tag{5.33}$$

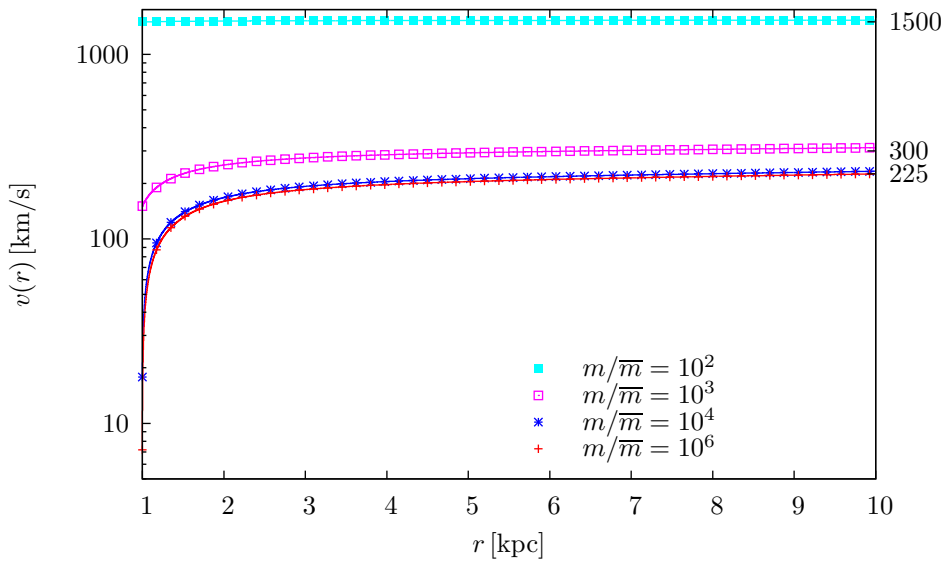

Fig. 9. Orbital speed of LVDM particle in circular orbit of radius r, as predicted by the model density profile and resulting gravitational field. Data points from the numerical solution to (5.14) are represented by points and labeled according to $m/\overline{m}$ (inset key). The analytical solution (5.31) is superimposed using corresponding line colors. A curve representing the orbital speed of a CDM particle would be indistinguishable (on this scale) from the bottom (red) curve, for which $m/\overline{m} = 10^6$. The case $m/\overline{m} = 10^5$ lies properly between the $m/\overline{m} = 10^4$ and $m/\overline{m} = 10^6$ curves and has been omitted for legibility.

B. Model Potential and Binding Energy

The potential corresponding to the gravitational field (5.5) is calculated to be:

$$\Phi = \begin{cases} -\frac{1}{2}\left(\frac{Gm_{\rm b}}{r_{\rm d}}\right)\left[3-\left(\frac{r}{r_{\rm d}}\right)^2\right] - G\lambda\left(\ln\frac{r_{\rm h}}{r_{\rm c}} - 1 + \frac{r_{\rm c}}{r_{\rm h}}\right) - \frac{GM_{\rm nb}}{r_{\rm h}}, & 0 \le r \le r_{\rm c}, \\ -\frac{1}{2}\left(\frac{Gm_{\rm b}}{r_{\rm d}}\right)\left[3-\left(\frac{r}{r_{\rm d}}\right)^2\right] - G\lambda\left(\ln\frac{r_{\rm h}}{r} - \frac{r_{\rm c}}{r} + \frac{r_{\rm c}}{r_{\rm h}}\right) - \frac{GM_{\rm nb}}{r_{\rm h}}, & r_{\rm c} \le r \le r_{\rm d}, \\ -G\lambda\left(\ln\frac{r_{\rm h}}{r} - \frac{r_{\rm c}}{r} + \frac{r_{\rm c}}{r_{\rm h}}\right) - \frac{Gm_{\rm b}}{r} - \frac{GM_{\rm nb}}{r_{\rm h}}, & r_{\rm d} \le r \le r_{\rm h}, \\ -\frac{GM_{\rm g}}{r}, & r \ge r_{\rm h}, \end{cases} \tag{5.34}$$

where $M_{\rm g} = M_{\rm nb} + m_{\rm b}$ is the mass of the galaxy. It is convenient to recast the approximations of (5.7)–(5.9) as:

$$G\lambda \approx \frac{GM_{\rm g}}{r_{\rm h}} \approx \frac{Gm_{\rm b}}{r_{\rm c}} \approx v_{\rm H}^2, \tag{5.35}$$

so that the potential in the region $r_{\rm c} \le r \le r_{\rm d}$ is approximately

$$\Phi_2(r) \approx -\frac{1}{2}v_{\rm H}^2\left(\frac{r_{\rm c}}{r_{\rm d}}\right)\left[3-\left(\frac{r_{\rm c}}{r_{\rm d}}\right)^2\left(\frac{r}{r_{\rm c}}\right)^2\right] - v_{\rm H}^2\left(\ln\frac{r_{\rm h}/r_{\rm c}}{r/r_{\rm c}} - \frac{1}{r/r_{\rm c}} + 1\right),\ r_{\rm c} \le r \le r_{\rm d}. \tag{5.36}$$

The binding energy for CDM is given by

$$\varepsilon_{\rm CDM} = \tfrac{1}{2}u_{\rm CDM}^2(r) + c^{-2}\Phi_2(r), \tag{5.37}$$

where $\varepsilon_{\rm CDM} \equiv (mc^2)^{-1}E_{\rm CDM}$ represents the total energy of a CDM particle in a circular orbit in the model potential (5.34), $u_{\rm CDM}^2(r) \approx u_{\rm H}^2 r g_2(r)$, and $r g_2(r)$ is given by (5.12). The binding energy for the LVDM candidate is given by:

$$\varepsilon_{\rm LVDM} = \gamma(r) - \gamma_0 + c^{-2}\Phi_2(r), \tag{5.38}$$

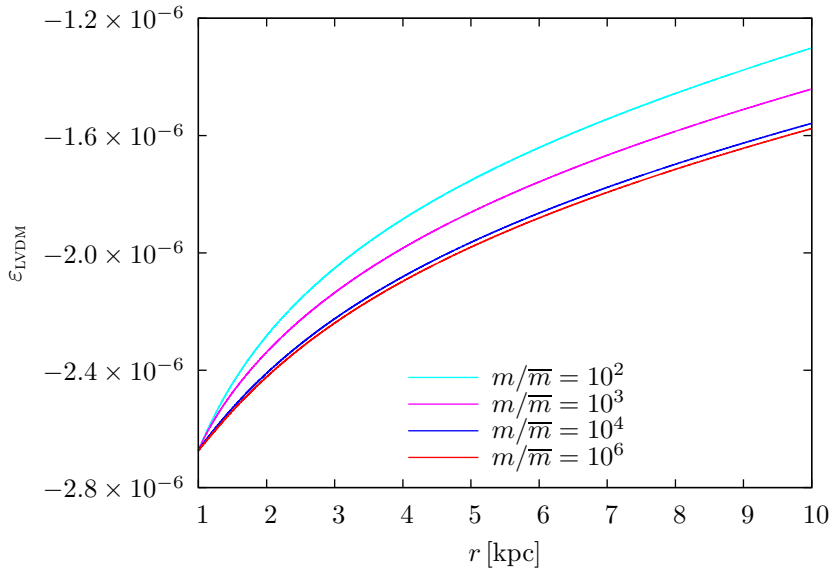

Fig. 10. Binding energy for LVDM particles in circular orbits of radius r (5.38) as predicted by the model potential (5.34) corresponding to the model density profile (5.4). A curve representing CDM binding energy would be indistinguishable from the $m/\overline{m} = 10^6$ (bottom, red) curve. Smaller values of $m/\overline{m}$ result in less binding, with the $m/\overline{m} = 10^2$ (top, cyan) curve representing a limiting value: Curves representing $m/\overline{m} \lesssim 10^2$ would be indistinguishable from this (top) curve. In effect, the entire range $0 \leq m/\overline{m} \leq \infty$ is represented.

where $\varepsilon_{\rm LVDM} = (mc^2)^{-1} E_{\rm LVDM}$ represents the total energy of a LVDM particle in a circular orbit in the model potential (5.34),

$$\gamma(r) - \gamma_0 = \sum_{\rm n=0}^{\infty} (-1)^{\rm n} \binom{-\frac{1}{2}}{\rm n} \left(u^{2\rm n}(r) - u_0^{2\rm n}\right), \tag{5.39}$$

$$\approx \tfrac{1}{2} \left(u^2(r) - u_0^2\right), \tag{5.40}$$

and $u(r) = v(r)/c$ is given by (5.33). This binding energy is plotted in Fig. 10 for several values of $m/\overline{m}$. The $m/\overline{m} = 10^6$ (bottom, red) curve would be indistinguishable from a plot of the binding energy for a CDM particle in the model potential (5.34). The $m/\overline{m} = 10^2$ (top, cyan) curve represents an upper limit to the LVDM binding energy. This limit corresponds to an LVDM particle with exactly

twice the kinetic energy of a CDM particle in an identical orbit, occurring when $v \approx v_0 \approx c$, as shown below.

In the regime for which $v - v_0 \ll v_0$, v_{LVDM} differs only slightly from v_0. The LVDM binding energy is compared to that of CDM using the relative difference

$$\frac{\Delta\varepsilon}{|\varepsilon_{\text{CDM}}|} = \frac{\tau_{\text{CDM}}}{|\varepsilon_{\text{CDM}}|}\left[1 + \left(\frac{v_{\text{CDM}}}{v_0}\right)^2\right] \xrightarrow[m/\overline{m}\to 0]{v_0 \to c} \frac{\tau_{\text{CDM}}}{|\varepsilon_{\text{CDM}}|}, \quad v - v_0 \ll v_0, \tag{5.41}$$

where $\Delta\varepsilon \equiv \varepsilon_{\text{LVDM}} - \varepsilon_{\text{CDM}}$, and $\tau_{\text{CDM}} \equiv (mc^2)^{-1}T_{\text{CDM}} = \frac{1}{2}u_{\text{CDM}}^2$ represents the kinetic energy of a CDM particle in the model potential (5.34). (See also (5.37).) The ratio of kinetic energy to total energy for CDM particles (5.41) in the model potential (5.34), as a function of radial coordinate, is given by

$$\frac{\tau_{\text{CDM}}}{|\varepsilon_{\text{CDM}}|} = \frac{1 - 1/(r/r_{\text{c}}) + (r_{\text{c}}/r_{\text{d}})^3(r/r_{\text{c}})^2}{1 - 1/(r/r_{\text{c}}) + 3(r_{\text{c}}/r_{\text{d}}) - 2(r_{\text{c}}/r_{\text{d}})^3(r/r_{\text{c}})^2 + 2\ln\left[(r_{\text{h}}/r_{\text{c}})/(r/r_{\text{c}})\right]}. \tag{5.42}$$

The kinetic energy of a LVDM particle in the model potential (5.34) is represented by $\tau_{\text{LVDM}} \equiv (mc^2)^{-1}T_{\text{LVDM}} = \gamma - \gamma_0 \approx \frac{1}{2}(u^2 - u_0^2)$. (See (5.38) and (5.40).) Substituting $u \approx u_0 + u_{\text{CDM}}^2/u_0$ ((5.29) and (5.33)) into the expression for kinetic energy results in relationships among energies of very high-speed LVDM and ordinary CDM particles, in identical orbits:

$$\tau_{\text{LVDM}} \approx 2\tau_{\text{CDM}} \quad \text{and} \quad \frac{\tau_{\text{LVDM}}}{|\varepsilon_{\text{LVDM}}|} \approx \frac{2\tau_{\text{CDM}}}{|\varepsilon_{\text{CDM}}|}\left(1 + \frac{\tau_{\text{CDM}}}{|\varepsilon_{\text{CDM}}|}\right), \quad v - v_0 \ll v_0. \tag{5.43}$$

In the regime for which $v - v_0 \gg v_0$, v_{LVDM} differs only slightly from v_{CDM}. (See (5.27) and (5.28).) The LVDM binding energy is again compared to that of CDM using the relative difference:

$$\frac{\Delta\varepsilon}{|\varepsilon_{\text{CDM}}|} = \frac{\tau_{\text{CDM}}}{|\varepsilon_{\text{CDM}}|}\left(\frac{2v_0}{v_{\text{CDM}}}\right) \xrightarrow[m/\overline{m}\to\infty]{v_0 \to 0} 0, \quad v - v_0 \gg v_0. \tag{5.44}$$

This represents what we will call the classical limit, wherein the dynamics of LVDM is expected to be nearly identical to that of CDM. Substituting $u = u_{\text{CDM}} + u_0$

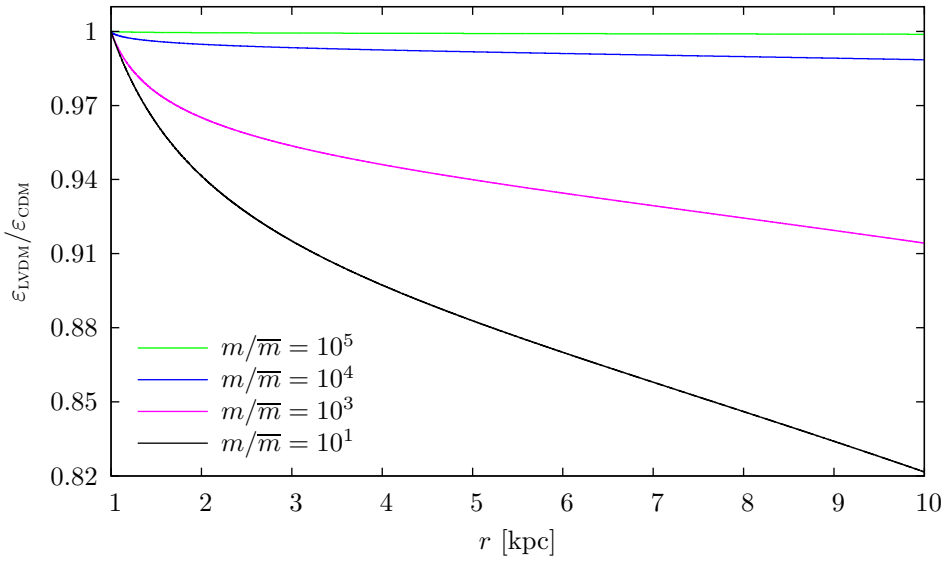

Fig. 11. Ratio of LVDM to CDM binding energies (5.46) for particles in circular orbits of radius r, as predicted by the model potential (5.34). Curves representing $m/\overline{m} > 10^5$ would be indistinguishable from the straight line $\varepsilon_{\rm LVDM}/\varepsilon_{\rm CDM} = 1$, over the entire domain $1\,{\rm kpc} \leq r \leq 10\,{\rm kpc}$. All values of $m/\overline{m} < 10^1$ result in curves which are indistinguishable from the $m/\overline{m} = 10^1$ (bottom, black) curve on this scale. A curve representing $m/\overline{m} = 10^2$ would lie above and be almost coincident with the $m/\overline{m} = 10^1$ curve, and has been omitted for legibility.

((5.27) and (5.33) with $u = v/c$) into the expression for kinetic energy results in relationships among energies of LVDM particles in the classical limit and ordinary CDM particles (in identical orbits):

$$\tau_{\rm LVDM} \approx \tau_{\rm CDM} + u_0 u_{\rm CDM} \quad \text{and} \quad \frac{\tau_{\rm LVDM}}{|\varepsilon_{\rm LVDM}|} \approx \frac{\tau_{\rm CDM}}{|\varepsilon_{\rm CDM}|}\left(1 + \frac{2u_0}{u_{\rm CDM}}\right), \quad v - v_0 \gg v_0. \quad (5.45)$$

In the regime for which $v - v_0 \sim v_0$ it is convenient to compare the LVDM binding

energy to that of CDM, by taking the ratio

$$\frac{\varepsilon_{\text{LVDM}}}{\varepsilon_{\text{CDM}}} = 1 - \frac{\frac{1}{4}u_0\left(\sqrt{u_0^2 + 4u_{\text{CDM}}^2} - u_0\right)}{|\varepsilon_{\text{CDM}}|}, \quad v - v_0 \sim v_0. \tag{5.46}$$

This binding energy ratio is plotted in Fig. 11 for several values of $m/\overline{m}$, and is valid for all values of u_0 consistent with the approximations of (5.21) and (5.40). A curve representing $m/\overline{m} = 10^6$ would be indistinguishable on this scale from the straight line $\varepsilon_{\text{LVDM}}/\varepsilon_{\text{CDM}} = 1$ over the entire domain $1\,\text{kpc} \le r \le 10\,\text{kpc}$, and can thus be regarded as representing the classical limit. Also, values of $m/\overline{m} < 10$ result in curves which are indistinguishable from the $m/\overline{m} = 10$ curve. In this limit

$$\frac{\varepsilon_{\text{LVDM}}}{\varepsilon_{\text{CDM}}} \to 1 - \frac{\tau_{\text{CDM}}}{|\varepsilon_{\text{CDM}}|}, \quad m/\overline{m} \le 10, \tag{5.47}$$

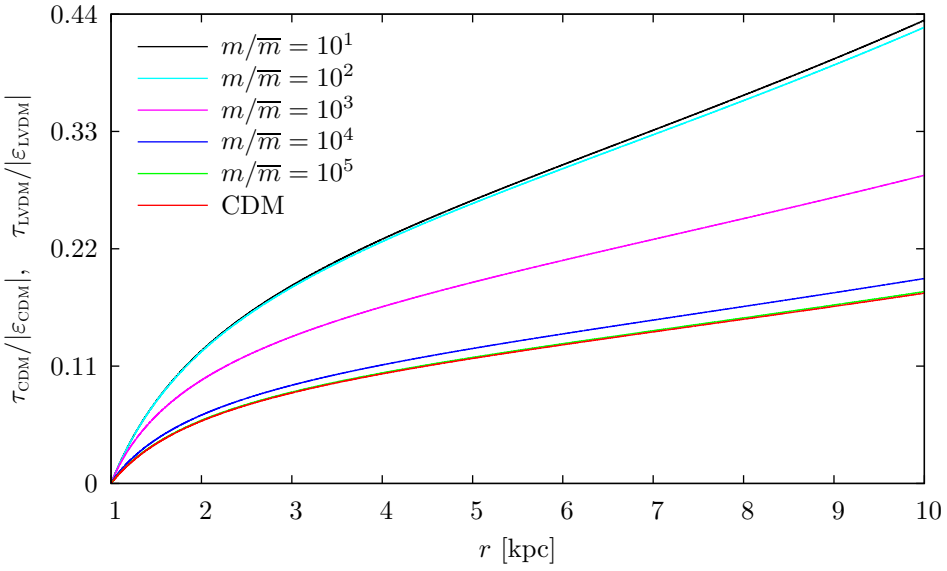

Fig. 12. Ratio of kinetic energy to total energy for both CDM (5.42) and LVDM (5.48) particles in identical circular orbits of radius r in the model potential (5.34). Curves representing $m/\overline{m} > 10^5$ would be indistinguishable from the CDM (bottom, red) curve over the entire domain $1\,\text{kpc} \le r \le 10\,\text{kpc}$. Values of $m/\overline{m} < 10^1$ result in curves which are indistinguishable from the $m/\overline{m} = 10^1$ (top, black) curve on this scale.

where $\tau_{\rm CDM}/|\varepsilon_{\rm CDM}|$ is given by (5.42) and is plotted in Fig. 12. The ratio of kinetic energy to total energy for LVDM particles may be expressed as

$$\frac{\tau_{\rm LVDM}}{|\varepsilon_{\rm LVDM}|} = \frac{\tau_{\rm CDM} + \frac{1}{4}u_0\sqrt{u_0^2 + 8\tau_{\rm CDM}} - \frac{1}{4}u_0^2}{|\varepsilon_{\rm CDM}| - \frac{1}{4}u_0\sqrt{u_0^2 + 8\tau_{\rm CDM}} + \frac{1}{4}u_0^2}, \quad v - v_0 \sim v_0, \tag{5.48}$$

and is shown in Fig. 12 for several values of $m/\overline{m}$. This expression is valid for all values of u_0 consistent with the approximations of (5.21) and (5.40), and correctly reduces to (5.43) and (5.45) in the appropriate limits. The ratio of kinetic energy to total energy for CDM particles (5.42) in the model potential (5.34) is very nearly zero near $r = 1\,\mathrm{kpc}$, as shown in Fig. 12, so that $\varepsilon_{\rm LVDM}/\varepsilon_{\rm CDM} \to 1$ as $r \to 1\,\mathrm{kpc}$. (See (5.47).) This is illustrated in Fig. 11. (Recall that we have taken $r_{\rm c} = 1\,\mathrm{kpc}$ in the model density profile (5.4).) More precisely, $\tau_{\rm CDM}/|\varepsilon_{\rm CDM}| = 1/(298 + 10^3 \ln 10^4) \approx 10^{-4}$ when $r = 1\,\mathrm{kpc}$ so that, for values $m/\overline{m} < 10^2$, $\varepsilon_{\rm LVDM}/\varepsilon_{\rm CDM} \approx 1 - 10^{-4}$. Figure 13 includes a closeup of $\varepsilon_{\rm LVDM}/\varepsilon_{\rm CDM}$ near $r = 1\,\mathrm{kpc}$, illustrating, precisely, the maximum reduction of LVDM binding compared to that of CDM near $r = 1\,\mathrm{kpc}$ over the entire relevant parameter space $m/\overline{m} \gg 1$ ($u_0 \ll 1$). On larger scales LVDM binding is much more reduced. Near $r = 10\,\mathrm{kpc}$, $\tau_{\rm CDM}/|\varepsilon_{\rm CDM}| = 1/(1 + 2\ln 10) \approx 0.18$ as $r \to 10\,\mathrm{kpc}$ so that for values $m/\overline{m} < 10^2$, $\varepsilon_{\rm LVDM}/\varepsilon_{\rm CDM} \approx 0.82$. Figure 13 also includes a close-up of $\varepsilon_{\rm LVDM}/\varepsilon_{\rm CDM}$ near $r = 10\,\mathrm{kpc}$. The LVDM binding energy is significantly smaller than that of CDM near $r = 10\,\mathrm{kpc}$. The preceding analysis emphasizes that, when compared to CDM, LVDM (1) is slighlty less bound on small scales, (2) is much less bound on large scales, and (3) has a well-defined limit as to how much weaker its binding is on large and small scales.

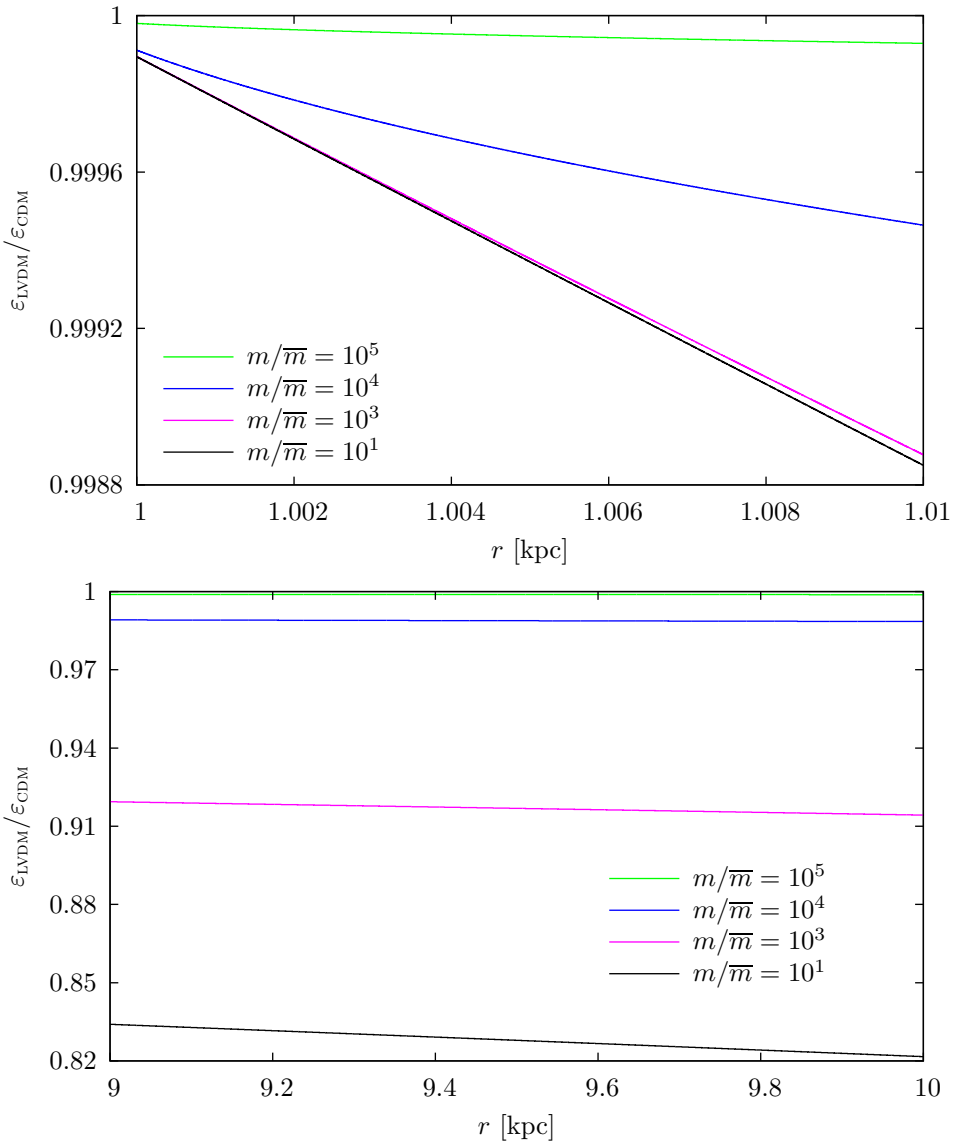

Fig. 13. Closeup of Fig. 11; Ratio of LVDM to CDM binding energies (5.46) for particles in circular orbits of radius r near $r = 1\,\mathrm{kpc}$ (top) and $r = 10\,\mathrm{kpc}$ (bottom). Top ($r = 1\,\mathrm{kpc}$): LVDM binding is not identical to that of CDM on the smallest scales; LVDM binding is smaller, but has a lower limit expressed as $\varepsilon_{\rm LVDM}/\varepsilon_{\rm CDM} \geq 1 - 10^{-4}$, over the entire relevant parameter space $m/\overline{m} \gg 1$. Bottom ($r = 10\,\mathrm{kpc}$): LVDM binding is significantly smaller on larger scales, but has a well defined lower limit of $\varepsilon_{\rm LVDM}/\varepsilon_{\rm CDM} \geq 0.82$, over the entire relevant parameter space $m/\overline{m} \gg 1$.

CHAPTER VI

CENTRAL MASS MODEL

For a central-mass model, it will be shown below that one can find approximate analytical solutions for the gravitational binding energy of the LVDM candidate, which can then be compared to that for CDM. Under reasonable circumstances the binding energy and equation of motion may each be approximated, and then solved simultaneously. The resulting expressions indicate the deviation of LVDM gravitational binding from that of standard CDM. In addition, simple arguments are given below to determine the effective potential for LVDM and compare it to that for CDM.

A. Binding Energy Velocity Dependence

Consider a LVDM particle under the gravitational influence of a central mass. The binding energy, with $\varepsilon_{\text{LVDM}} \equiv (mc^2)^{-1} E_{\text{LVDM}}$, and the equation governing the motion are given respectively by

$$\varepsilon_{\text{LVDM}} = \gamma - \gamma_0 - \frac{r_{\text{S}}}{r} \tag{6.1}$$

$$\frac{r_{\text{S}}}{r} = (\gamma u - \gamma_0 u_0)\, u, \tag{6.2}$$

where $\tau_{\text{LVDM}} \equiv (mc^2)^{-1} T_{\text{LVDM}} = \gamma - \gamma_0$ represents the kinetic energy, $-r_{\text{S}}/r = c^{-2}\Phi$ is the gravitational potential, $u = v/c$ is the orbital speed, and $r_{\text{S}} \equiv GM_{\text{g}}/c^2 \approx 10^{-5}\,\text{kpc}$ is half the Schwarzschild radius for a galaxy of $10^{11}\, m_{\odot}$. Direct elimination of the radial coordinate is then trivial, yielding

$$\varepsilon_{\text{LVDM}} = \gamma - \gamma_0 - (\gamma u - \gamma_0 u_0)\, u. \tag{6.3}$$

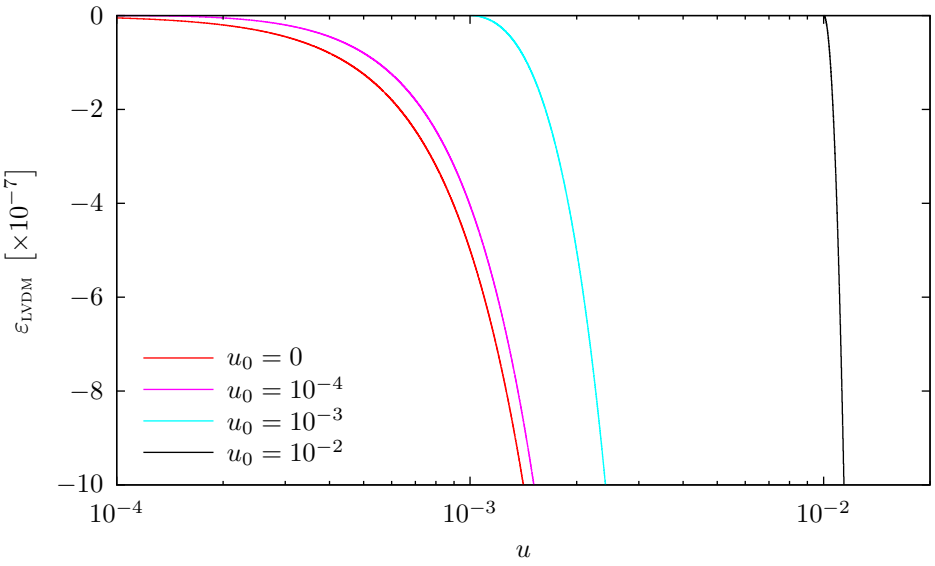

Fig. 14. Binding energy for LVDM particles as a function of orbital speed (6.3) in the central-mass model. The $u_0 = 0$ curve (red, leftmost) represents the lower limit, for which $\varepsilon_{\rm LVDM}(u, u_0 = 0) = \varepsilon_{\rm CDM}(u)$. A curve representing $u_0 = 10^{-5}$ lies to the right of, and is nearly coincident with, the $u_0 = 0$ curve, and has been omitted for legibility. Values of $u_0 \ll 10^{-4}$ result in binding energies differing only slightly from those of CDM. Values of $u_0 \gg 10^{-3}$ indicate behavior substantially different from that of CDM. Values of $u < u_0$ are nonphysical and are not included, so that the curves are truncated along the top of the figure, at their maxima: $\varepsilon_{\rm LVDM}(u_0, u_0) = 0$.

This binding energy is plotted as a function of orbital speed in Fig. 14 for several values of u_0. The curve for $u_0 = 0$ represents CDM with the same orbital speeds, and is plotted (red, leftmost) for comparison: $\varepsilon_{\rm LVDM}(u, u_0 = 0) = \varepsilon_{\rm CDM}(u)$. A point of reference is the CDM binding energy for a particle in orbit with radius $r \approx 50\,\mathrm{kpc}$, for which $\varepsilon_{\rm CDM} \equiv (mc^2)^{-1} E_{\rm CDM} = -\frac{1}{2}u^2 \approx -10^{-7}$. Recall that $u_0 \equiv 1/\sqrt{1 + (2m/\overline{m})^2}$, so that $u_0 \approx 1/(2m/\overline{m})$ for $m/\overline{m} \gg 1$. Values of $u_0 \ll 10^{-4}$ result in binding energies differing only slightly from those of CDM. Values of $u_0 \gg 10^{-3}$ indicate behavior substantially different from that of CDM. Values of $u < u_0$ are nonphysical, and are not included, so that the curves are truncated along the top of the figure, at

their maxima: $\varepsilon_{\text{LVDM}}(u_0, u_0) = 0$. A detailed comparison of LVDM and CDM binding energies is possible using approximate analytical solutions.

Recall that LVDM orbital speeds are constrained both (1) from above, due to the finite mass distribution of the galaxy, so that u, and therefore u_0, must be nonrelativistic; and (2) from below, due to the minimum speed set by $m/\overline{m}$, so that u must be greater than or equal to u_0. The result is that u is always very nearly equal to u_0. (E.g., see (4.28), (4.30) and Fig. 3.) Under these circumstances it was found that (see (5.22)–(5.26))

$$(\gamma u - \gamma_0 u_0)\, u \approx \phi_1 + \phi_2, \tag{6.4}$$

where $\{\phi_1, \phi_2\} \equiv \left\{u_0\,(u-u_0)\,, (u-u_0)^2\right\}$. Similarly, the kinetic energy may be expanded in powers of u and u_0 (5.40), and then expressed in terms of ϕ_1 and ϕ_2, resulting in

$$\gamma - \gamma_0 \approx \tfrac{1}{2}\left(u^2 - u_0^2\right) \tag{6.5}$$

$$\approx u_0\,(u-u_0) + \tfrac{1}{2}\,(u-u_0)^2 \tag{6.6}$$

$$\approx \phi_1 + \tfrac{1}{2}\phi_2. \tag{6.7}$$

Applying the approximations of (6.4) and (6.7) to the binding energy and equation of motion ((6.1), and (6.2)), a simple expression for the binding energy is found:

$$\left.\begin{aligned} \varepsilon_{\text{LVDM}} + \frac{r_{\text{S}}}{r} &\approx \phi_1 + \tfrac{1}{2}\phi_2 \\ \frac{r_{\text{S}}}{r} &\approx \phi_1 + \phi_2 \end{aligned}\right\} \implies \varepsilon_{\text{LVDM}} \approx -\tfrac{1}{2}\phi_2 = -\tfrac{1}{2}\,(u-u_0)^2. \tag{6.8}$$

This expression is valid for all regions centered on $u_0 \sim u - u_0$. The same result is obtained if ϕ_1 is neglected altogether. This corresponds to the region for which $u_0 \ll u - u_0$ (large $m/\overline{m}$), in which the LVDM binding energy is expected to be very

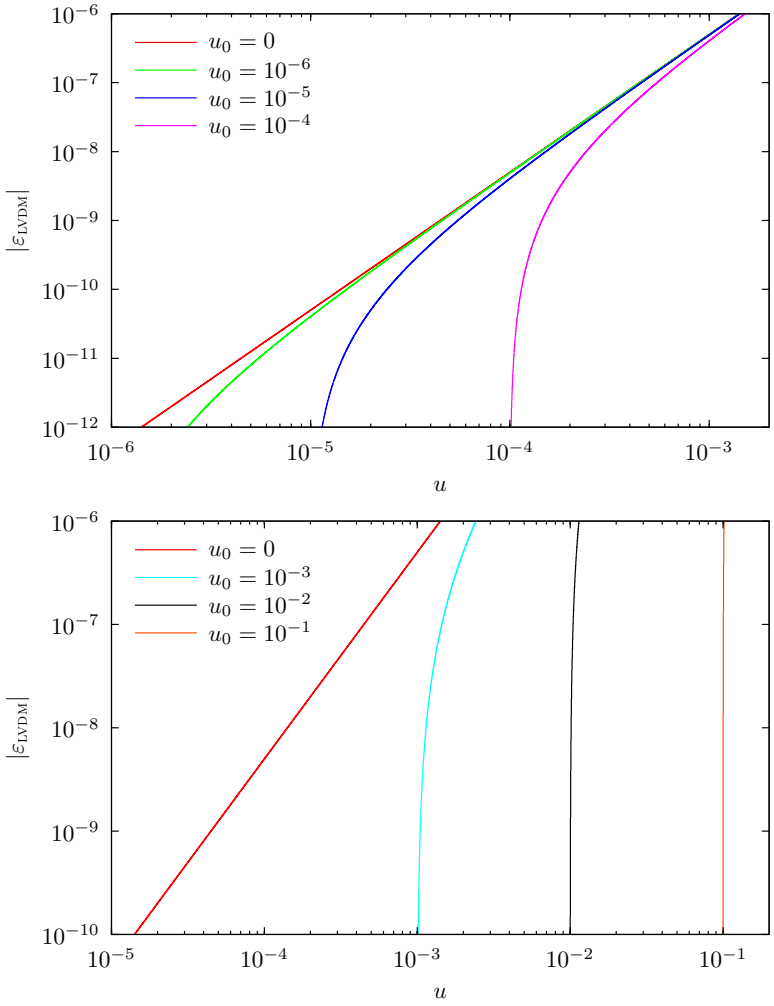

Fig. 15. Binding energy for LVDM particles as a function of orbital speed in the central-mass model (6.3). Binding energies for LVDM are similar to those of CDM for small values of u_0 (upper panel). Although binding energies comparable to those of CDM are possible for larger values of u_0 (lower panel), such Lorentz-violating particles are unstable to the smallest change in speed. It is unlikely that a large system of particles, unstable to such small changes in speed, would remain bound on galactic scales. I.e., small perturbations would cause such particles to become unbound. This Lorentz-violating model is thus unviable unless u_0 is small, and $\overline{m}/m$ is therefore $\ll 1$, for the same reason that ordinary hot matter like neutrinos is not a viable candidate for the dark matter distributions in galaxies.

nearly the same as that of CDM. In this region we have $\phi_2 \gg \phi_1$, so that ϕ_1 may be neglected. The binding energy (6.8) reduces to the CDM result for vanishing u_0; that is, $\varepsilon_{\text{LVDM}} \to -\frac{1}{2}u^2$ as $u_0 \to 0$, as expected. The binding energy is plotted against orbital speeds for several values of u_0 in Fig. 15.

Consider the region defined by $u - u_0 \ll u_0$ (small $m/\overline{m}$), in which the LVDM binding energy is expected to show large deviations from that of CDM. In this region $\phi_1 \gg \phi_2$ so that ϕ_2 may be neglected, resulting in:

$$\left.\begin{aligned} \varepsilon_{\text{LVDM}} + \frac{r_{\text{S}}}{r} &\approx \phi_1 \\ \frac{r_{\text{S}}}{r} &\approx \phi_1 \end{aligned}\right\} \implies \varepsilon_{\text{LVDM}} \approx 0. \tag{6.9}$$

In this region the LVDM particles are effectively unbound. This is also the result obtained from the more general expression for the binding energy (6.8) in the limit $u - u_0 \ll u_0$.

B. Binding Energy Radial Dependence

The binding energy may alternatively be expressed in terms of the radial coordinate and compared to that of CDM. The desired result is obtained by eliminating u from the following system of equations:

$$\varepsilon_{\text{LVDM}} \approx -\tfrac{1}{2}\phi_2 \tag{6.10}$$

$$\frac{r_{\text{S}}}{r} \approx \phi_1 + \phi_2. \tag{6.11}$$

If ϕ_1 is neglected, the binding energy can be expressed in terms of the radial coordinate:

$$\left.\begin{aligned} \varepsilon_{\text{LVDM}} &\approx -\tfrac{1}{2}\phi_2 \\ \frac{r_{\text{S}}}{r} &\approx \phi_2 \end{aligned}\right\} \implies \varepsilon_{\text{LVDM}} \approx -\frac{r_{\text{S}}}{2r}. \tag{6.12}$$

Again, the binding energy is the same as that for CDM. Instead neglect ϕ_2 in the equation of motion (6.11) to derive the binding energy in terms of the radial coordinate:

$$\left.\begin{aligned} \varepsilon_{\text{LVDM}} &\approx -\tfrac{1}{2}\phi_2 \\ \frac{r_{\text{S}}}{r} &\approx \phi_1 \end{aligned}\right\} \implies \varepsilon_{\text{LVDM}} \approx -2u_0^{-2}\left(\frac{r_{\text{S}}}{2r}\right)^2. \tag{6.13}$$

This is the same result as that obtained in (4.21) and earlier in (4.10), which provided much of the original motivation for this investigation. Although this binding energy has a $1/r^2$-dependence, rather than the usual $1/r$-dependence for standard CDM particles, it is not immediately obvious that this represents reduced binding compared to CDM. Recall that $r_{\text{S}} \approx 10^{-5}\,\text{kpc}$, and assume that LVDM particles have radial coordinates with $1\,\text{kpc} \leq r \leq 100\,\text{kpc}$, so that $10^5 \lesssim r/r_{\text{S}} \lesssim 10^7$. Correspondingly, $10^{-7} \lesssim r_{\text{S}}/r \lesssim 10^{-5}$, which is a measure of CDM binding energy. Choosing $u_0 \approx 10^{-3}$ it is found that $10^{-8} \lesssim u_0^{-2}\,(r_{\text{S}}/r)^2 \lesssim 10^{-4}$, which is a measure of LVDM binding energy. Compared to CDM binding, the LVDM binding is reduced by a factor of 10 on large (100 kpc) scales and increased by a factor of 10 on small (1 kpc) scales. Choosing $u_0 = 2 \times 10^{-3}$ it is found that $10^{-9} \lesssim u_0^{-2}\,(r_{\text{S}}/r)^2 \lesssim 10^{-5}$; The LVDM binding energy is smaller than that of CDM by a factor of 100 on large (100 kpc) scales, and the same as that of CDM on small (1 kpc) scales. Choosing $u_0 \approx 10^{-2}$ it is found that $10^{-10} \lesssim u_0^{-2}\,(r_{\text{S}}/r)^2 \lesssim 10^{-6}$; the LVDM binding is reduced by a factor of 10^3 on large (100 kpc) scales and reduced by a factor of 10 on small (1 kpc) scales. It is shown below that the approximation leading to this inverse-square binding energy depends critically on the value of u_0; In order that the approximation (6.13) be valid over the entire domain, $1\,\text{kpc} \leq r \leq 100\,\text{kpc}$, it is necessary that $u_0 \gg 10^{-3}$. However, as shown in the preceding analysis, LVDM particles with $u_0 \gg 10^{-3}$ are unlikely to be bound on galactic scales. (See Figs. 14 and 15.)

A careful characterization of the three regions defined by (1) $u_0 \ll u - u_0$, (2) $u_0 \sim u - u_0$, and (3) $u_0 \gg u - u_0$, was carried out in the context of the model density profile (following (5.26)) and is repeated here in the context of the central-mass model for completeness. The three regions are defined for purposes of further approximating the equation determining the motion, $\phi_1 + \phi_2 = r_{\rm s}/r$, and are distinguished by a crossover point defined by $2\phi_1(u_0^*) = 2\phi_2(u_0^*) = r_{\rm s}/r$. Thus, $u = 2u_0^*$, so that $2\left(u_0^*\right)^2 = r_{\rm s}/r$. Then, for a given radial distance, a crossover point is defined by $u_0^* = \sqrt{r_{\rm s}/\left(2r\right)}$. For example, $u_0^* \approx 2 \times 10^{-3}$ $(m/\overline{m} \approx 3 \times 10^2)$ for $r = 1\,{\rm kpc}$, and $u_0^* \approx 2 \times 10^{-4}$ $(m/\overline{m} \approx 3 \times 10^3)$ for $r = 100\,{\rm kpc}$. Let us choose a single crossover point that is consistent with an entire reasonably-chosen domain, $1\,{\rm kpc} \leq r \leq 100\,{\rm kpc}$. Then the three regions may be characterized as follows: (1) For the region in which $u_0 \ll u - u_0$, $u_0 \ll 10^{-4}$, and $\phi_1 \ll \phi_2$; (2) For the region in which $u_0 \gg u - u_0$, $u_0 \gg 10^{-3}$, and $\phi_1 \gg \phi_2$; and (3) For the region in which $u_0 \sim u - u_0$, $10^{-4} \leq u_0 \leq 10^{-3}$, and $\phi_1 \sim \phi_2$. It is interesting to note that the crossover-point minimum velocity has the same order of magnitude as the radius-dependent velocity of a CDM particle: $u_0^* \sim u_{\rm CDM}(r) = \sqrt{r_{\rm s}/r}$. LVDM particles are less likely to be bound if the minimum velocity is set much higher than CDM particle velocities, and more likely to be bound if set much lower.

The solution for all regions centered on $u_0 \sim u - u_0$ is found by solving the system of equations, (6.10) and (6.11), without further approximation. The solution is

$$\varepsilon_{\rm LVDM} \approx -\frac{r_{\rm s}}{2r} + \frac{u_0}{4}\left(u_0^2 + \frac{4r_{\rm s}}{r}\right)^{1/2} - \frac{u_0^2}{4}, \tag{6.14}$$

Figure 16 displays this binding energy for several values of u_0. A curve representing CDM binding energies (top, red) is included for reference. Small values of u_0 again result in binding energies similar to those of CDM, and a curve representing $u_0 = 10^{-6}$ would be indistinguishable from the CDM binding energy curve. Binding energies

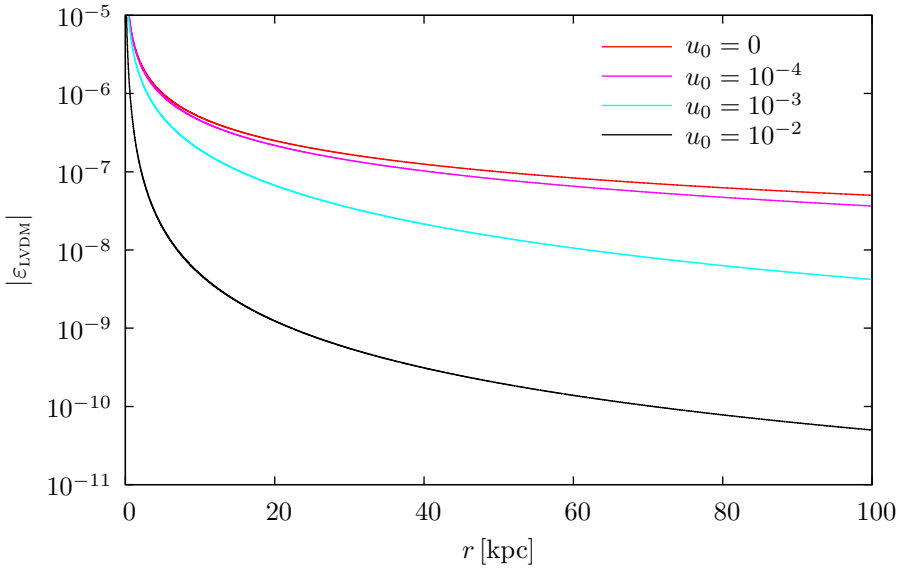

Fig. 16. Binding energy as a function of radial coordinate for LVDM particles in circular orbits (6.14) in the central-mass model. The $u_0 = 0$ curve (top, red) is the binding energy for CDM particles in an identical potential. Small values of u_0 result in binding similar to that of CDM. Large values of u_0 produce weak binding on all but the smallest scales. For the full range of r values, the binding is similar to that of CDM on small scales and weaker on large scales.

are similar on small scales, independent of u_0. Large values of u_0 result in much weaker binding, except on the smallest scales. Taking u_0 to be small, and expanding the root in (6.14), results in

$$\varepsilon_{\rm LVDM} \approx -\frac{r_{\rm s}}{2r} + \frac{u_0}{\sqrt{2}}\left(\frac{r_{\rm s}}{2r}\right)^{1/2} - \frac{u_0^2}{4}, \quad u_0 \ll 10^{-4}. \tag{6.15}$$

This approximation is subject to the condition: $u_0^2 < 4r_{\rm s}/r$, where $r_{\rm s} \approx 10^{-5}\,$kpc. Assume LVDM particles have radial coordinates $1\,{\rm kpc} < r < 100\,{\rm kpc}$, so that $10^5 < r/r_{\rm s} < 10^7$. The condition is satisfied as long as $u_0 \lesssim 10^{-4}$, or $m/\overline{m} \gtrsim 10^3$. This result reduces to that for CDM as $u_0 \to 0$, as expected. Taking u_0 to be large,

and expanding the root in (6.14) to second order, the inverse-square binding energy (6.13) is recovered:

$$\varepsilon_{\text{LVDM}} \approx -2u_0^{-2}\left(\frac{r_{\text{S}}}{2r}\right)^2, \quad u_0 \gg 10^{-3}. \tag{6.16}$$

This result – an original motivation for this investigation – is valid only for $u_0 \gg 10^{-3}$, but LVDM is not likely to be bound for such values. A more realistic prediction for the decreased binding is given by (6.15), for which $u_0 \ll 10^{-4}$. Although the validity of the small-scale behavior within the central-mass model is questionable, the result is similar to that using the more detailed model density profile of (5.4) and (5.34): When compared to CDM, LVDM is much less bound on large (100 kpc) scales, and slightly less bound on small (1 kpc) scales, for values of $u_0 \ll 10^{-4}$.

C. Effective Potential and Orbital Stability

An approximate effective potential for LVDM particles in the presence of a central mass will now be derived and compared to that for CDM. First considering the radial force equation, $F_r = \dot{p}_r - p_\varphi\dot{\varphi}$, where $F_r = mc^2 r_{\text{S}}/r^2$, and $r_{\text{S}} = 10^{-5}$ kpc is half the Schwarzschild radius of the central mass. Then, an effective force can be defined as

$$F_{\text{e}} \equiv \dot{p}_r = F_r + p_\varphi\dot{\varphi}, \tag{6.17}$$

and is expected to be different than that of CDM due to a non-standard momentum-velocity relation. The linear momentum is related to the velocity by

$$\mathbf{p} = \frac{\dot{\mathbf{r}}/c}{u}\,p(u,u_0) \quad \Rightarrow \quad p_\varphi\dot{\varphi} = \frac{r\dot{\varphi}/c}{u}\,p(u,u_0)\dot{\varphi}, \tag{6.18}$$

where $p(u,u_0) = mc(\gamma u - \gamma_0 u_0)$ is the linear momentum-velocity relation for LVDM particles. The conserved angular momentum is given by $\ell_\varphi \equiv \gamma^3 r^2\dot{\varphi}/c$, so that $\dot{\varphi}$ may

be eliminated in favor of r and $u(r)$

$$p_\varphi \dot{\varphi} = \frac{\ell_\varphi^2}{r^3} \gamma^{-6} u^{-1} pc, \tag{6.19}$$

as in (4.36)–(4.39). Substitution of the equation of motion (6.2) results in

$$p_\varphi \dot{\varphi} = \frac{\ell_\varphi^2 r_\mathrm{s}}{r^4} \gamma^{-6} u^{-2} mc^2. \tag{6.20}$$

If we were to take $\gamma = 1$ and $u^2 = r_\mathrm{s}/r$ we would be back to the standard centrifugal force equation in Newtonian dynamics,

$$p_\varphi \dot{\varphi} = \frac{\ell_\varphi^2 r_\mathrm{s}}{r^3} mc^2. \tag{6.21}$$

Taking u_0 to be small (large $m/\overline{m}$), we have $r_\mathrm{s}/r \approx (u - u_0)^2$, as in (6.12), so that the orbital speed as a function of radius may be approximated as

$$u^{-2} \approx \frac{r}{r_\mathrm{s}} \left(1 + u_0 \sqrt{\frac{r}{r_\mathrm{s}}} \right)^{-2}. \tag{6.22}$$

Substituting this into (6.20), and taking $\gamma^{-6} \approx 1$, then yields

$$p_\varphi \dot{\varphi} \approx \frac{\ell_\varphi^2}{r^3} \left(1 + u_0 \sqrt{\frac{r}{r_\mathrm{s}}} \right)^{-2} mc^2. \tag{6.23}$$

The effective force, $F_\mathrm{e} = F_r + p_\varphi \dot{\varphi}$, follows immediately:

$$(mc^2)^{-1} F_\mathrm{e} \approx -\frac{r_\mathrm{s}}{r^2} + \frac{\ell_\varphi^2}{r^3} \left(1 + u_0 \sqrt{\frac{r}{r_\mathrm{s}}} \right)^{-2} \tag{6.24}$$

$$\approx -\frac{r_\mathrm{s}}{r^2} + \frac{\ell_\varphi^2}{r^3} - u_0 \frac{2\ell_\varphi^2}{r_\mathrm{s}^{1/2} r^{5/2}} + u_0^2 \frac{3\ell_\varphi^2}{r_\mathrm{s} r^2} \tag{6.25}$$

The first two terms of (6.25) are identical to the effective force in classical dynamics (CDM), while the last two terms are corrections arising from the non-standard

dynamics of LVDM. The effective potential corresponding to (6.25) is:

$$(mc^2)^{-1}U_{\rm e} \approx -\frac{r_{\rm s}}{r} + \frac{\ell_\varphi^2}{2r^2} - u_0\frac{4\ell_\varphi^2}{3r_{\rm s}^{1/2}r^{3/2}} + u_0^2\frac{3\ell_\varphi^2}{r_{\rm s}r}, \tag{6.26}$$

Again, the first two terms of (6.26) are identical to the effective potential in standard dynamics (CDM), while the last two terms are corrections arising from the nonstandard dynamics of LVDM. The effective force (6.25) and effective potential (6.26) are plotted in Fig. 17 for small values of u_0. The angular momentum is chosen to be given by $\ell_\varphi^2 = r_{\rm s}r_0 = 4\times10^{-5}\,{\rm kpc}^2$, corresponding to a circular orbit of radius $r_0 = 4\,{\rm kpc}$. The curves representing $u_0 = 10^{-6}$ would be indistinguishable from those representing CDM on these scales. The radius of a circular orbit is found from $F_{\rm e}(r_0) = -\partial U_{\rm e}/\partial r|_{r_0} = 0$, and is shown to first decrease, and then increase, as u_0 is increased. The predicted radius is found to be less than that of CDM for $u_0 < 9\times10^{-4}$.

The radius of a circular orbit is found explicitly by setting (6.25) to zero, resulting in

$$\left(1 - 3u_0^2\pi_\varphi^2\right)\frac{r_0}{\ell_\varphi^2/r_{\rm s}} + 2u_0\pi_\varphi\left(\frac{r_0}{\ell_\varphi^2/r_{\rm s}}\right)^{1/2} - 1 = 0, \tag{6.27}$$

where $\pi_\varphi \equiv \ell_\varphi/r_{\rm s}$ so that $\pi_\varphi^2 \approx 4\times10^5$ is a dimensionless quantity. Notice that $r_0 \to \ell_\varphi^2/r_{\rm s} \approx 4\,{\rm kpc}$ as $u_0 \to 0$ is the result obtained for CDM for the chosen values of ℓ_φ and $r_{\rm s}$. In the region for which $1 - 3u_0^2\pi_\varphi^2 > 0$, we have $u_0 < 9.1\times10^{-4}$, and a single solution exists. For very small values of u_0, the solution to (6.27) may be expressed as

$$\frac{r_0}{\ell_\varphi^2/r_{\rm s}} \approx \frac{1}{1-3u_0^2\pi_\varphi^2} - \frac{2u_0\pi_\varphi}{\left(1-3u_0^2\pi_\varphi^2\right)^{3/2}}, \quad u_0^2 \ll \frac{1}{3\pi_\varphi^2}. \tag{6.28}$$

Orbital stability is determined by checking the sign of the negative of the derivative

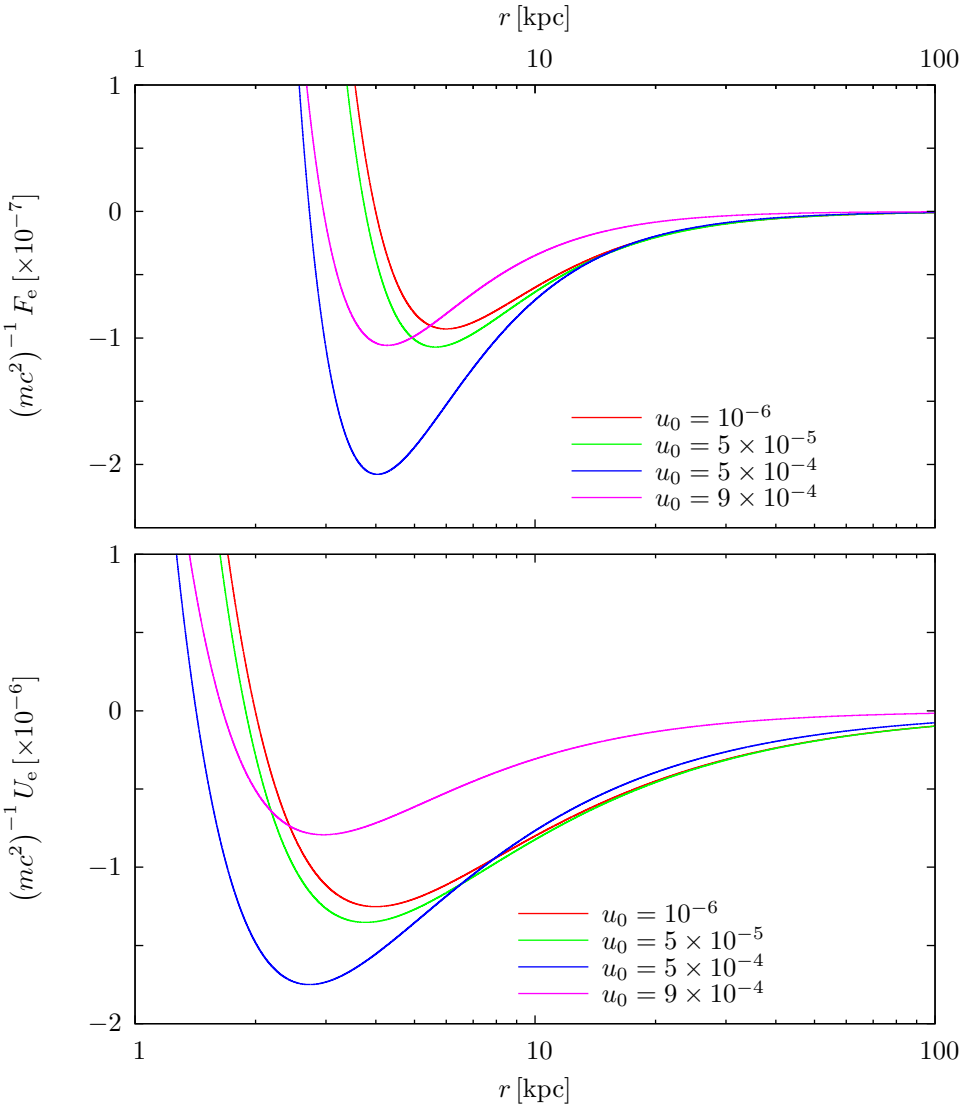

Fig. 17. Effective force (6.25) and effective potential (6.26) are plotted for small values of u_0. The values of u_0 are chosen so that adjacent curves are easily distinguishable. The curves representing $u_0 = 10^{-6}$ would be indistinguishable from those of CDM on these scales. As u_0 is increased, the radius r_0 corresponding to a circular orbit ($F_e(r_0) = -\partial U_e/\partial r|_{r_0} = 0$) first decreases, and then increases, but is always smaller than that of CDM.

of the effective force (6.25) evaluated at r_0. This leads directly to the condition

$$-\left.\frac{\partial F_{\rm e}}{\partial r}\right|_{r_0} > 0 \;\Rightarrow\; -2\left(\frac{r_0}{\ell_\varphi^2/r_{\rm s}}\right)+3-5u_0\pi_\varphi\left(\frac{r_0}{\ell_\varphi^2/r_{\rm s}}\right)^{1/2}+6u_0^2\pi_\varphi^2\left(\frac{r_0}{\ell_\varphi^2/r_{\rm s}}\right)>0. \quad (6.29)$$

Substitution of (6.28) into the above stability condition results in:

$$1-\frac{5u_0\pi_\varphi}{\left(1-3u_0^2\pi_\varphi^2\right)^{1/2}}+\frac{4u_0\pi_\varphi}{\left(1-3u_0^2\pi_\varphi^2\right)^{3/2}}>0, \quad u_0^2\ll\frac{1}{3\pi_\varphi^2}, \quad (6.30)$$

which holds true over the specified parameter space: $u_0 < 9.1\times10^{-4}$. The parameter space is extended using the exact solution to (6.27):

$$\frac{r_0}{\ell_\varphi^2/r_{\rm s}}=\frac{1}{1-3u_0^2\pi_\varphi^2}-2\left(\frac{u_0\pi_\varphi}{1-3u_0^2\pi_\varphi^2}\right)^2\left[\left(1+\frac{1-3u_0^2\pi_\varphi^2}{u_0^2\pi_\varphi^2}\right)^{1/2}-1\right],\; u_0^2<\frac{1}{3\pi_\varphi^2}. \quad (6.31)$$

The radius of a circular orbit (6.31) is plotted for small values of u_0 in Fig. 18 (top, red). The stability condition (6.29) is evaluated at each value of r_0 obtained from (6.31) and is also plotted in Fig. 18 (bottom, red). The curves end abruptly at $u_0 = 1/\sqrt{3\pi_\varphi^2} \approx 9.1\times10^{-4}$, beyond which the solutions are no longer valid. (See Appendix C for a discussion of the parameter space $u_0 > 9.1\times10^{-4}$ in this approximation.) The green (crisscrossed) curves are plots of orbital radius (6.28) and corresponding stability condition (6.30) for very small values of u_0; these approximations are valid for $u_0 < 10^{-4}$. Circular orbits are stable for small values of u_0.

A more accurate description of the effective potential for $u_0 > 10^{-4}$ can be achieved by taking $r_{\rm s}/r \approx (u-u_0)^2 + u_0(u-u_0)$, as in (6.11), so that the orbital speed as a function of radius may be approximated as

$$u^{-2}\approx\frac{r}{r_{\rm s}}\left[\left(1+u_0^2\frac{r}{4r_{\rm s}}\right)^{1/2}+u_0\frac{r^{1/2}}{2r_{\rm s}^{1/2}}\right]^{-2}. \quad (6.32)$$

If we substitute this into (6.20), and take $\gamma^{-6} \approx \gamma_0^{-6}$, the effective force follows

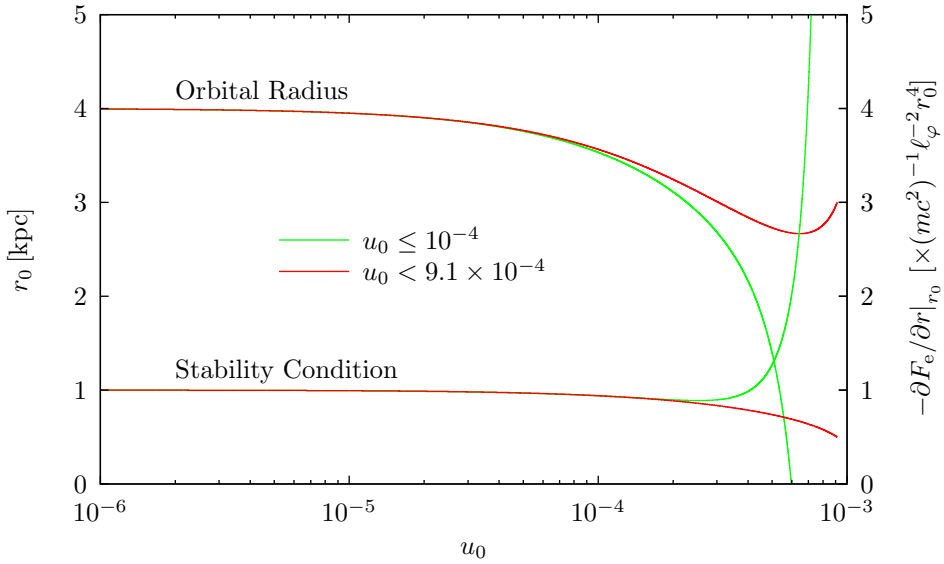

Fig. 18. The radius of a circular orbit and the stability condition are plotted for small values of u_0. The top red curve is a plot of the radius given by (6.31), and the bottom red curve the corresponding stability condition (6.29) evaluated at each value of r_0 obtained from (6.31). The curves end abruptly at $u_0 = 1/\sqrt{3\pi_\varphi^2} \approx 9.1 \times 10^{-4}$, beyond which the solutions are no longer valid. The green (crisscrossed) curves are plots of the orbital radius (6.28) and corresponding stability condition (6.30) for very small values of u_0; these approximations are valid for $u_0 < 10^{-4}$. Circular orbits are always stable for the values of u_0 shown, as indicated by the red lines.

immediately via the same argument that led to (6.24) earlier:

$$(mc^2)^{-1}F_{\rm e} \approx -\frac{r_{\rm s}}{r^2} + \frac{\ell_\varphi^2\gamma_0^{-6}}{r^3}\left[\left(1+u_0^2\frac{r}{4r_{\rm s}}\right)^{1/2} + u_0\frac{r^{1/2}}{2r_{\rm s}^{1/2}}\right]^{-2}. \tag{6.33}$$

The effective potential is then given by

$$\begin{aligned}(mc^2)^{-1}U_{\rm e} \approx \left(\tfrac{1}{2}u_0^2\pi_\varphi^2\gamma_0^{-6} - 1\right)\frac{r_{\rm s}}{r} + \pi_\varphi^2\gamma_0^{-6}\frac{r_{\rm s}^2}{2r^2} \\ - u_0\pi_\varphi^2\gamma_0^{-6}\frac{2r_{\rm s}^{3/2}}{3r^{3/2}}\left(1+u_0^2\frac{r}{2r_{\rm s}}\right)^{3/2} + (mc^2)^{-1}U_0,\end{aligned} \tag{6.34}$$

where $(mc^2)^{-1}U_0 \equiv \frac{1}{12}u_0^4\pi_\varphi^2\gamma_0^{-6}$ is added so that $U_{\rm e}(\infty) = 0$. This effective potential is valid over the entire range $0 \leq u_0 \leq 10^{-1}$, and is plotted for a large range of u_0 values in Fig. 19. The effect of increasing u_0 is to push the centrifugal barrier inward toward smaller values of r, and to deepen the potential wells. For a given binding energy, LVDM particles have larger kinetic energies than CDM particles. Orbits are predicted to be stable with larger values of u_0 forcing particles into tighter orbits.

Taking u_0 to be large (small $m/\overline{m}$), we have $r_{\rm s}/r \approx u_0(u - u_0)$, as in (6.12) so that the orbital speed as a function of radius may be approximated as

$$u^{-2} \approx u_0^2\frac{r_{\rm s}^2}{r^2}\left(1 + u_0^2\frac{r_{\rm s}}{r}\right)^{-2}. \tag{6.35}$$

Substituting this into (6.20) and taking $\gamma^{-6} \approx \gamma_0^{-6}$ yields

$$p_\varphi\dot{\varphi} = u_0^2\frac{\ell_\varphi^2\gamma_0^{-6}}{r_{\rm s}r^2}\left(1 + u_0^2\frac{r}{r_{\rm s}}\right)^{-2}mc^2. \tag{6.36}$$

The effective force and potential then follow immediately:

$$(mc^2)^{-1}F_{\rm e} \approx -\frac{r_{\rm s}}{r^2} + u_0^2\frac{\ell_\varphi^2\gamma_0^{-6}}{r_{\rm s}r^2}\left(1 + u_0^2\frac{r}{r_{\rm s}}\right)^{-2} \tag{6.37}$$

$$\begin{aligned}(mc^2)^{-1}U_{\rm e} \approx\ & \left(u_0^2\pi_\varphi^2\gamma_0^{-6} - 1\right)\frac{r_{\rm s}}{r}, \\ & + u_0^4\pi_\varphi^2\gamma_0^{-6}\left[\left(1 + u_0^2\frac{r}{r_{\rm s}}\right)^{-1} + 2\ln\frac{r}{r_{\rm s}}\left(1 + u_0^2\frac{r}{r_{\rm s}}\right)^{-1}\right] \\ & + \left(mc^2\right)^{-1}U_0,\end{aligned} \tag{6.38}$$

where $(mc^2)^{-1}U_0 \equiv -2u_0^4\pi_\varphi^2\gamma_0^{-6}\ln u_0^{-2}$ is added so that $U_{\rm e}(\infty) = 0$. This effective potential (6.38) is plotted for large values of u_0 in Fig. 20. As u_0 is increased to very large values, the radius of a stable circular orbit, r_0, continues to decrease, approaching the Schwarzschild radius, $r_{\rm s} \approx 10^{-5}$. The solution certainly is not valid for $r_0 < r_{\rm s}$; The value of u_0 corresponding to a circular orbit in this limiting case can

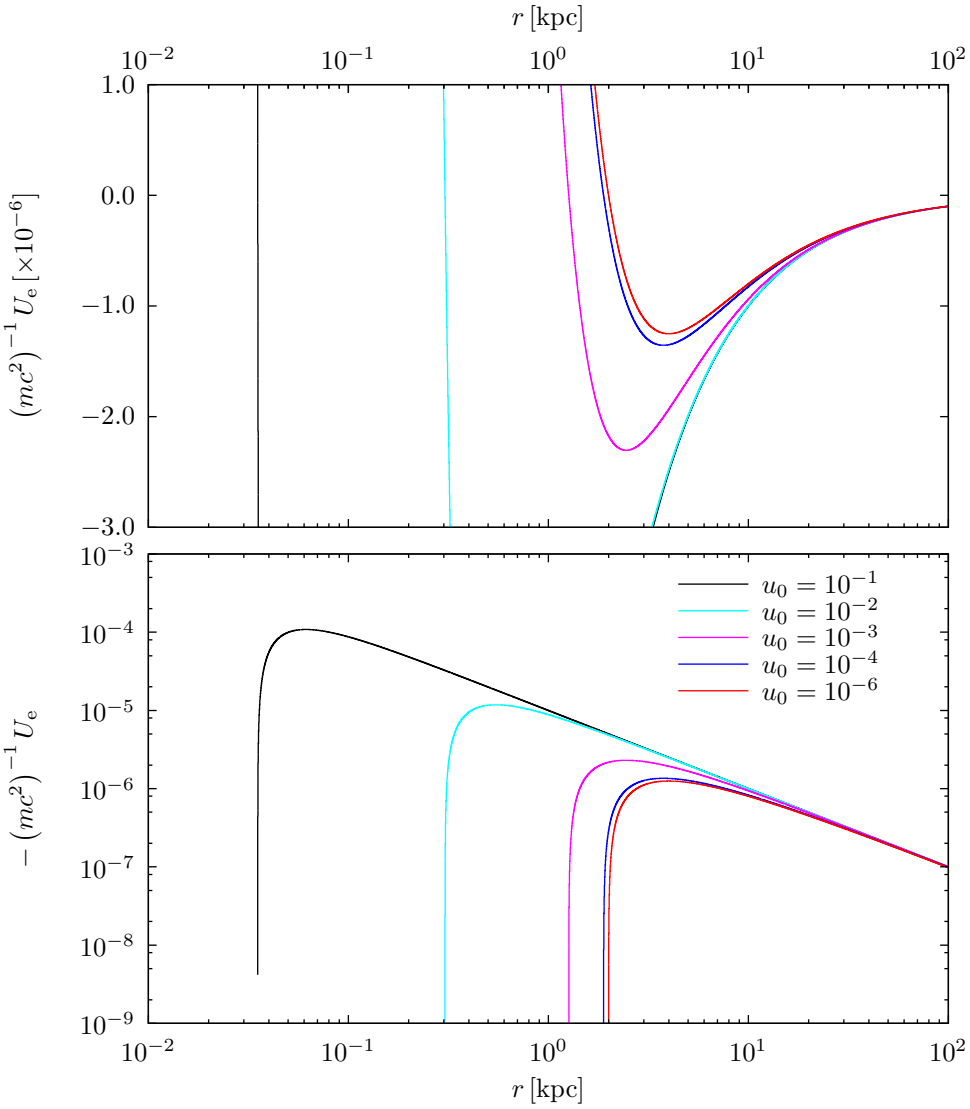

Fig. 19. LVDM effective potential (6.34) for a large range of u_0. The effect of increasing u_0 is to push the centrifugal barrier inward toward smaller values of r, and to deepen the potential wells. For a given binding energy, LVDM particles have larger kinetic energies than CDM particles. Orbits are predicted to be stable, with larger values of u_0 forcing particles into tighter orbits.

be calculated from $F_{\rm e}(r_{\rm s}) = 0$, resulting in $u_0^{\rm s} \approx \sqrt{1-(\pi_\varphi^2/2)^{-1/3}} \approx 0.991$. However, the solution is already clearly invalid when $U_{\rm e}(r_{\rm s}) = 0$, which yields

$u_0^{\max} \approx \sqrt{1 - [(3 - 4\ln 2)\pi_\varphi^2/2]^{-1/3}} \approx 0.986$. Therefore, the approximate effective force (6.37) and potential (6.38) are valid for $u_0 < 0.986$ and $u_0 \gg 10^{-3}$.

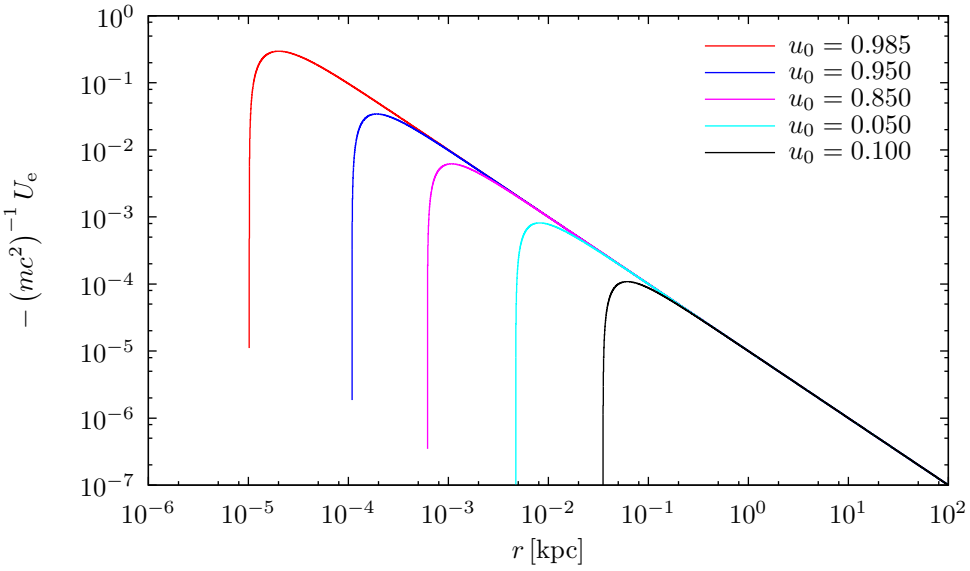

Fig. 20. The effective potential (6.38) is plotted for very large values of u_0. As u_0 is increased to very large values, the radius of a stable circular orbit, r_0, continues to decrease, approaching the Schwarzschild radius, $r_{\rm s} \approx 10^{-5}$.

CHAPTER VII

LAGRANGIAN FORMULATION

The Lagrangian for a standard relativistic (SR) particle under the influence of a central force is [189]

$$\mathcal{L}_{\text{SR}} = -\gamma^{-1}mc^2 - U(r). \tag{7.1}$$

The total energy is given by the Hamiltonian, $\mathcal{H} = pv - \mathcal{L}$, with $p = \partial\mathcal{L}/\partial v$ (where $\gamma^{-1} = \sqrt{1-(v/c)^2}$) so that

$$\mathcal{H}_{\text{SR}} = \gamma mc^2 + U(r) \tag{7.2}$$

$$= T_{\text{SR}} + U(r) + mc^2, \tag{7.3}$$

where $T_{\text{SR}} = (\gamma - 1)mc^2$ is the kinetic energy.

The Lagrangian for a LV particle (again under the influence of a central force) is

$$\mathcal{L}_{\text{LV}} = -\gamma^{-1}mc^2 - \gamma_0 m v_0 v - U(r). \tag{7.4}$$

The Hamiltonian $\mathcal{H} = pv - \mathcal{L}$, with $p = \partial\mathcal{L}/\partial v = \gamma mv - \gamma_0 m v_0$, is then

$$\mathcal{H}_{\text{LV}} = \gamma mc^2 + U(r) \tag{7.5}$$

$$= T_{\text{LV}} + U(r) + \gamma_0 mc^2, \tag{7.6}$$

where $T_{\text{LV}} = (\gamma - \gamma_0)mc^2$ is the kinetic energy of a LV particle, subject to the constraint $\gamma \geq \gamma_0 > 1$.

This procedure can be generalized to a large class of Lorentz-violating systems, for which $p = k(v, m)v$, by choosing

$$T^* \equiv \int_{v_0}^{v} k(v', m)v' \, \mathrm{d}v' - E_0, \tag{7.7}$$

where $E_0 = E_0(m)$ and $v_0 = v_0(m)$ are the zero-momentum energy and velocity, respectively. The usual expression for the kinetic energy may be obtained by integrating by parts,

$$T = \int_0^p v(p')\,\mathrm{d}p' = v^2 k(v,m) - \int_{v_0}^{v} k(v',m)v'\,\mathrm{d}v', \tag{7.8}$$

so that the Lagrangian may be expressed as $\mathcal{L} = v^2 k(v,m) - T - E_0 - U(r)$. Therefore, the Hamiltonian is $\mathcal{H} = T + U(r) + E_0$. Furthermore, the form of the resulting Hamiltonian is the same as that for standard relativity, with the implied constraint of a minimum velocity. (Compare (7.2) and (7.5).) Standard physics is, of course, recovered in the limit $v_0 \to 0$. It appears that this formalism may be applied to a large class of Lorentz-violating systems which reduce to standard relativity in the limit $v_0 \to 0$.

A. Angular Momentum and Effective Potential

The conserved angular momentum is found from the Lagrangian (7.4) to be

$$\tilde{\ell}_\varphi \equiv (k/m) r^2 \dot{\varphi}/c, \tag{7.9}$$

where k is given by

$$k(v,m) = (\gamma m v - \gamma_0 m v_0)/v \tag{7.10}$$

Then $\dot{\varphi}/c = \tilde{\ell}_\varphi (k/m)^{-1} r^{-2}$ so that

$$(mc^2)^{-1} p_\varphi \dot{\varphi} = (k/m) r \dot{\varphi}^2/c^2 \tag{7.11}$$

$$= \frac{\tilde{\ell}_\varphi^2}{(k/m) r^3}. \tag{7.12}$$

(See (6.17).) The results for a standard relativistic particle are recovered in the appropriate limit: $\tilde{\ell}_\varphi \to \gamma r^2\dot{\varphi}/c$ and $(mc^2)^{-1}p_\varphi\dot{\varphi} \to \tilde{\ell}_\varphi^2/(\gamma r^3)$, as $v_0 \to 0$. More generally, it is reasonable to take v/c to be small if v_0/c is small and particles are confined to galactic dimensions, so that (7.10) becomes

$$k/m = 1 - \frac{v_0}{v} + \frac{1}{2}\left(\frac{v}{c}\right)^2 - \frac{1}{2}\frac{v_0}{v}\left(\frac{v_0}{c}\right)^2 + \cdots \tag{7.13}$$

$$\approx 1 - \frac{v_0}{v}, \tag{7.14}$$

wherein it is also assumed that $(v/c)^2 \ll v_0/v \ll 1$, or equivalently, $(v/c)^3 \ll v_0/c$. Typical galactic speeds are $(v/c)^3 \sim 10^{-9}$, allowing for a large parameter space: $10^{-4} < v_0/c < 10^{-8}$. In this approximation (7.9) and (7.12) may be expressed as

$$\tilde{\ell}_\varphi \approx \left(1 - \frac{v_0}{v}\right) r^2\dot{\varphi}/c \tag{7.15}$$

$$(mc^2)^{-1}p_\varphi\dot{\varphi} \approx \frac{\tilde{\ell}_\varphi^2}{r^3}\left(1 - \frac{v_0}{v}\right)^{-1}. \tag{7.16}$$

The results for a standard particle are recovered in the appropriate limit: $\tilde{\ell}_\varphi \to r^2\dot{\varphi}/c$ and $(mc^2)^{-1}p_\varphi\dot{\varphi} \to \tilde{\ell}_\varphi^2/r^3$ as $v_0 \to 0$. On galactic scales it is possible to compare the Lorentz-violating particles to standard particles. A standard CDM particle represents the limit in which both relativistic and Lorentz-violating corrections are neglected. The angular momentum and centrifugal force are derived above, and may be interpreted as corrections to the standard particle description due to a small violation of Lorentz invariance. As v_0 is increased, the angular momentum is reduced, and the centrifugal force is thus also reduced. Particles are likely to occupy a smaller volume than standard particles. This is the obvious result that faster moving particles must have tighter orbits to remain bound. Alternatively, LVDM may be compared to CDM with the same value of angular momentum. As v_0 is increased, LVDM particles are likely to have larger orbits and experience a larger centrifugal force. (See (7.15)

and (7.16).)

An effective potential can also be derived. Equation (7.11) may be re-expressed, without approximation, as

$$(mc^2)^{-1}p_\varphi\dot{\varphi} = \frac{\tilde{\ell}_\varphi}{r}(\dot{\varphi}/c). \tag{7.17}$$

Assuming $r^2\dot{\varphi}^2 \gg \dot{r}^2$, we can solve (7.15) for $\dot{\varphi}$:

$$\dot{\varphi}/c \approx \frac{\bar{\ell}_\varphi}{r^2} + \frac{v_0/c}{r}, \tag{7.18}$$

where $\bar{\ell}_\varphi \equiv \ell_\varphi(1-u_0\ell_\varphi/r_\mathrm{s})$ is the conserved angular momentum in this approximation. (Recall that ℓ_φ is the angular momentum of a standard particle.) It is assumed that $u_0 < r_\mathrm{s}/\ell_\varphi$ so that $\tilde{\ell}_\varphi \approx \bar{\ell}_\varphi > 0$. Substituting this expression into (7.17) results in

$$(mc^2)^{-1}p_\varphi\dot{\varphi} \approx \frac{\tilde{\ell}_\varphi^2}{r^3}\left(1 + u_0\frac{r}{\tilde{\ell}_\varphi}\right), \tag{7.19}$$

wherein it is assumed that $\tilde{\ell}_\varphi\bar{\ell}_\varphi \approx \tilde{\ell}_\varphi^2$. The effective force (6.17) and corresponding effective potential follow immediately:

$$(mc^2)^{-1}F_\mathrm{e} = -\frac{r_\mathrm{s}}{r^2}\left(1 - u_0\frac{\tilde{\ell}_\varphi}{r_\mathrm{s}}\right) + \frac{\tilde{\ell}_\varphi^2}{r^3}, \tag{7.20}$$

$$(mc^2)^{-1}U_\mathrm{e} = -\frac{r_\mathrm{s}}{r}\left(1 - u_0\frac{\tilde{\ell}_\varphi}{r_\mathrm{s}}\right) + \frac{\tilde{\ell}_\varphi^2}{2r^2}. \tag{7.21}$$

The effective potential (7.21) is plotted in Fig. 21, for small values of u_0. The values $\ell_\varphi^2 = 4\times10^{-5}\,\mathrm{kpc}^2$ and $r_\mathrm{s} = 10^{-5}\,\mathrm{kpc}$ have been chosen (as in Fig. 17). Then the angular momentum is positive for $u_0 < 1.58\times10^{-3}$.

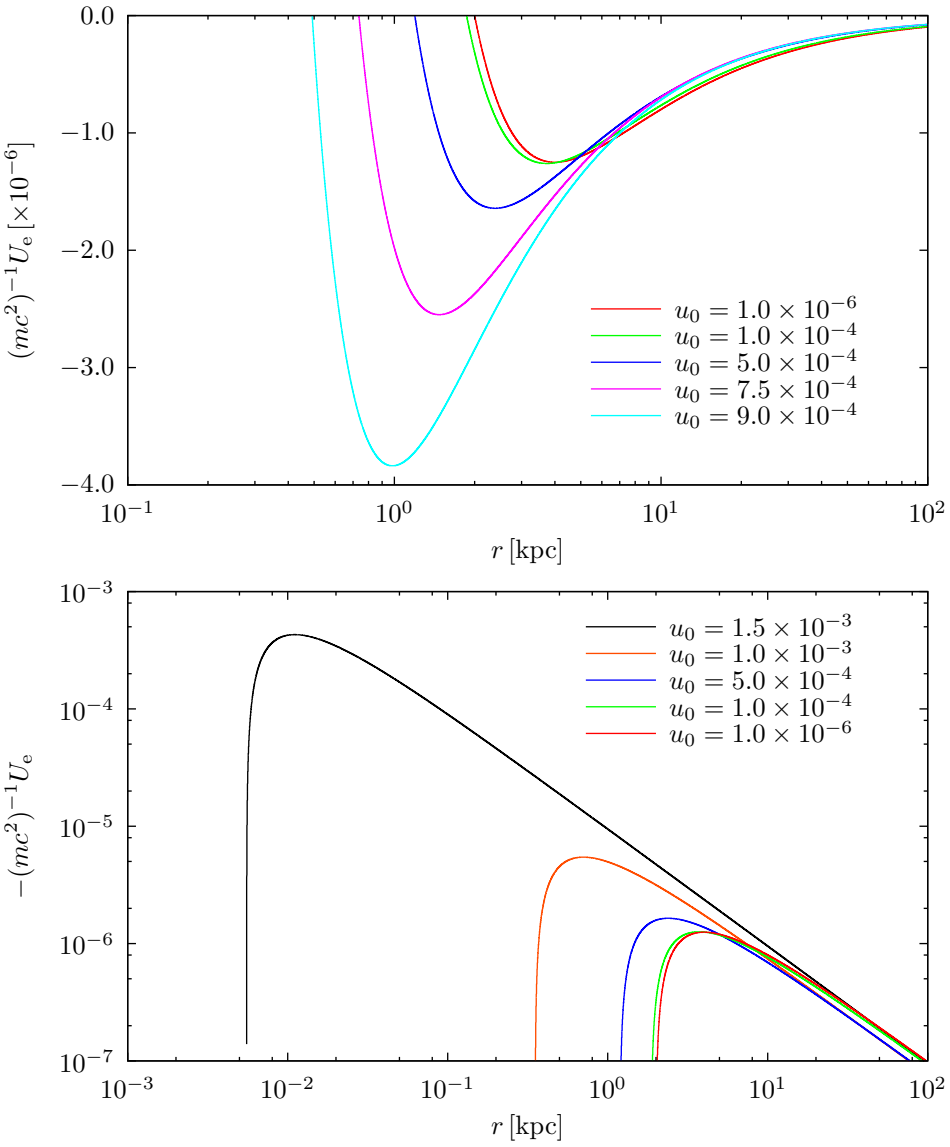

Fig. 21. The effective potential (7.21) is plotted for small values of u_0. The top panel displays curves which are similar to those for CDM. As u_0 is increased, the radius of a stable circular orbit, r_0, decreases. The bottom panel includes larger values of u_0 and emphasizes that the radius of a circular orbit decreases by several orders of magnitude, and that the potential well deepens by several orders of magnitude. The corresponding kinetic energy may be increased by several orders of magnitude.

B. Precession and other Orbital Features

1. Schwarzschild Geometry

Relativistic corrections to the central-mass problem are correctly described by the Schwarzschild geometry, which yields [25, 190–196]

$$\frac{\mathrm{d}^2}{\mathrm{d}\varphi^2}\left(\frac{\alpha}{r}\right)+\frac{\alpha}{r}=1+3\epsilon^2\left(\frac{\alpha}{r}\right)^2, \tag{7.22}$$

where $\alpha \equiv L^2/(GMm^2)$ and $L \equiv mr^2\dot{\varphi}$ as in the Newtonian description, and $\epsilon \equiv v_\alpha/c$, where $v_\alpha \equiv \sqrt{GM/\alpha}$ is the speed that a particle in a circular orbit of radius α would have in the Newtonian description. The conic-sections of the Newtonian description are recovered in the limit $\epsilon \to 0$ ($c \to \infty$):

$$\frac{\alpha}{r}=1+e\cos\varphi, \tag{7.23}$$

where $e \equiv [1+E/(\frac{1}{2}mv_\alpha^2)]^{1/2}$ is the eccentricity of the orbit, so that the term proportional to ϵ^2 in (7.22) may be treated as a small correction to the Newtonian description. The solution is usually found perturbatively, and limited to determining the apsidal precession per revolution of bound orbits:

$$\delta\varphi \approx 3\epsilon^2(2\pi). \tag{7.24}$$

Another common approach to the general relativistic problem is to define an equivalent effective potential using the Schwarzschild solution [190, 191, 197]:

$$\tilde{U}_{\text{eff}} \equiv mc^2\left(1-\frac{r_\text{s}}{r}\right)^{1/2}\left(1+\frac{\alpha r_\text{s}}{2r^2}\right)^{1/2}, \tag{7.25}$$

where $r_\text{s} \equiv 2GM/c^2$ is now the Schwarzschild radius. It is then determined that the radius of a stable circular orbit is smaller than that derived from the Newtonian

description: $r_c = \frac{1}{2}\alpha + \frac{1}{2}\alpha(1 - 12\epsilon^2)^{1/2} < \alpha$. Define $\delta r \equiv r_c - \alpha$ so that

$$\delta r \approx -3\epsilon^2\alpha. \tag{7.26}$$

(This result also holds if the equivalent effective potential is, instead, defined as $U_{\text{eff}} \equiv (\tilde{U}_{\text{eff}}^2 - m^2c^4)/(2mc^2)$, which results in an effective potential that is more easily compared to that derived from a Newtonian description.) Equations (7.24) and (7.26) serve as points for comparison to an alternative solution to the relativistic central-mass problem that follows.

Applying the change of variable $1/\rho \equiv \alpha/r - 1$ to (7.22) results in

$$\frac{\mathrm{d}^2}{\mathrm{d}\varphi^2}\left(\frac{1}{\rho}\right) + \frac{1}{\rho} = 3\epsilon^2\left(1 + \frac{1}{\rho}\right)^2. \tag{7.27}$$

Assume that $1/\rho \ll 1$ so that $(1 + 1/\rho)^2 \approx 1 + 2/\rho$; This is equivalent to restricting the solutions to nearly circular orbits. Then

$$\frac{\mathrm{d}^2}{\mathrm{d}\varphi^2}\left(\frac{1}{\rho}\right) + \kappa^2\left(\frac{1}{\rho}\right) \approx 3\epsilon^2, \tag{7.28}$$

where $\kappa^2 \equiv 1 - 6\epsilon^2$. Applying another change of variable $1/\bar{\rho} \equiv \kappa^2(1/\rho) - 3\epsilon^2$ results in

$$\frac{\mathrm{d}^2}{\mathrm{d}\varphi^2}\left(\frac{1}{\bar{\rho}}\right) + \kappa^2\left(\frac{1}{\bar{\rho}}\right) \approx 0, \tag{7.29}$$

the solution of which is a precessing ellipse:

$$\frac{\alpha}{r} \approx 1 + 3\epsilon^2 + (1 + 6\epsilon^2)e\cos(1 - 3\epsilon^2)\varphi, \tag{7.30}$$

where e is defined after (7.23). Corrections to the total energy are of order $(v/c)^4$ so that, for small speeds, e is approximately the same as that for a classical orbit. The approximation preceding (7.28) is now seen to be equivalent to the assumption of small eccentricity: $e \ll 1$. The solution (7.30) is verified by direct substitution into (7.22),

keeping terms only up to orders ϵ^2, e, and $\epsilon^2 e$. This closed-form solution lends itself to easy comparison with the orbital equation derived from the Newtonian description (7.23) and is similar to perturbative solutions in the following respects: The predicted rate of precession is identical to that derived using perturbative solutions (7.24); and circular orbits are predicted to be smaller than those derived from a Newtonian description by a measure identical to that derived from the equivalent effective potential (7.26). In addition, nearly circular relativistic orbits are predicted to be more eccentric than Keplerian orbits: $\delta e \approx 6\epsilon^2 e$. The success of this solution (7.30) in correctly describing general relativistic effects provides incentive for the application of this approximation scheme to the problem defined by the classical relativistic Lagrangian, which results in a similar equation of motion, and describes corrections due only to special relativity.

2. Classical Relativistic Lagrangian

As already discussed above in more general context, a classical relativistic particle under the influence of a central gravitational force is described by the Lagrangian [189, 198, 199]

$$\mathcal{L} = -\gamma^{-1} mc^2 - U(r), \tag{7.31}$$

where $\gamma^{-1} \equiv \sqrt{1-(v/c)^2}$ and $U(r) = -GMm/r$. The resulting equation of motion is

$$-\frac{\partial U}{\partial r} = \gamma m\ddot{r} + \dot{\gamma} m\dot{r} - \gamma m r\dot{\varphi}^2 \tag{7.32}$$

$$L = \gamma m r^2 \dot{\varphi}, \tag{7.33}$$

where L is the conserved angular momentum. In the interest of deriving an equation for the orbit, $r(\varphi)$, the following quantities are calculated:

$$\frac{\mathrm{d}^2}{\mathrm{d}\varphi^2}\left(\frac{1}{r}\right) = -\frac{m}{L^2}\gamma r^2\left(\gamma m\ddot{r} + \dot{\gamma} m\dot{r}\right), \tag{7.34}$$

$$\frac{L^2}{m}\gamma^{-1}r^{-3} = \gamma m r\dot{\varphi}^2, \tag{7.35}$$

wherein (7.33) is used repeatedly. The right-hand sides of these expressions are recognized as parts of the equation of motion (7.32) which may now be expressed as

$$\frac{\mathrm{d}^2}{\mathrm{d}\varphi^2}\left(\frac{\alpha}{r}\right) + \frac{\alpha}{r} \approx 1 + \frac{1}{2}\left(\frac{v}{c}\right)^2, \tag{7.36}$$

in the limit of small velocities so that $\gamma \approx 1 + \frac{1}{2}(v/c)^2$. (This is reminiscent of velocity-dependent forces [200, 201] that were introduced immediately after the inception of special relativity in 1905.) The conic sections of the Newtonian description (7.23) are recovered in the limit $c \to \infty$, so that the term $\frac{1}{2}(v/c)^2$ may be treated as a small correction to the Newtonian description. With nearly circular orbits in mind, a zeroth-order correction to the Newtonian description is to determine $(v/c)^2$ from the classical virial theorem: $-\frac{1}{2}U \approx T$, where $T \equiv (\gamma - 1)mc^2$. Then

$$\frac{GMm/c^2}{2r} = \tfrac{1}{2}mv^2/c^2 + O(1/c^4), \tag{7.37}$$

or

$$\left(\frac{v_\alpha}{c}\right)^2\frac{\alpha}{r} \approx \left(\frac{v}{c}\right)^2. \tag{7.38}$$

(Recall the definitions of α and v_α after (7.22).) The orbital equation (7.36) may now be expressed as

$$\frac{\mathrm{d}^2}{\mathrm{d}\varphi^2}\left(\frac{\alpha}{r}\right) + \bar{\kappa}^2\left(\frac{\alpha}{r}\right) \approx 1, \tag{7.39}$$

where $\bar{\kappa}^2 \equiv 1 - \frac{1}{2}(v_\alpha/c)^2$. Apply the change of variable $1/\rho \equiv \bar{\kappa}^2(\alpha/r) - 1$ so that

$$\frac{\mathrm{d}^2}{\mathrm{d}\varphi^2}\left(\frac{1}{\rho}\right) + \bar{\kappa}^2\left(\frac{1}{\rho}\right) \approx 0, \tag{7.40}$$

the solution of which is a precessing ellipse:

$$\frac{\alpha}{r} \approx 1 + \tfrac{1}{2}\epsilon^2 + (1 + \tfrac{1}{2}\epsilon^2)e\cos(1 - \tfrac{1}{4}\epsilon^2)\varphi, \tag{7.41}$$

where $\epsilon \equiv v_\alpha/c$ is the same parameter defined in the general relativistic solution (7.30) and e is defined after (7.23). Corrections to the total energy are of order $(v/c)^4$ so that, for small speeds, e is approximately the same as for a classical orbit. Although the assumption of small eccentricty is not explicit in this solution, the assumption of small speeds, $\gamma \approx 1 + \frac{1}{2}(v/c)^2$, and the approximate virial theorem (7.38) may not hold at the periapsis of a highly eccentric orbit. The solution (7.41) is verified by direct substitution into (7.39), keeping only terms up to orders ϵ^2 and $\epsilon^2 e$. This closed-form solution lends itself to easy comparison with the orbital equation derived from the Newtonian description (7.23), and has the same general features as that derived from the general relativistic description (7.30). Relativistic orbits are predicted to exhibit forward precession; (7.41) predicts the forward apsidal precession per revolution to be $\delta\varphi \approx \frac{1}{4}\epsilon^2(2\pi)$. The standard approach to incorporating special relativity predicts twice this value [189, 202–204], which is still in error by a factor of one-sixth when compared to the general relativistic result (7.24). (As much as two-thirds of the correct rate of precession may be calculated using special relativity together with the equivalence principle [205, 206]. This approach is avoided here in order to have a model to compare with Lorentz violation, for which it is not clear at present how to incorporate the equivalence principle.) The radius of a circular orbit is predicted to be smaller than that derived from a Newtonian description; (7.41) predicts a difference in radius of $\delta r \approx -\frac{1}{2}\epsilon^2\alpha$,

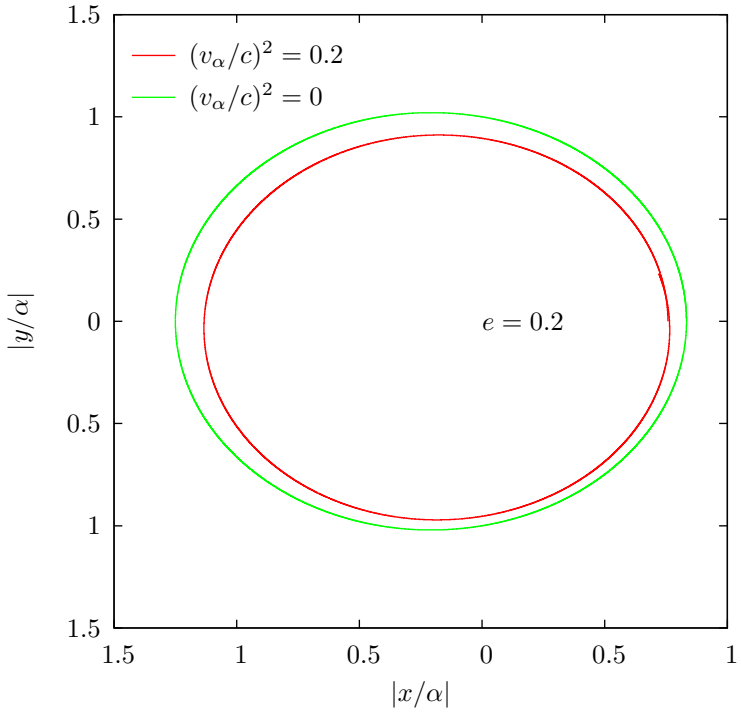

Fig. 22. Orbit of a relativistic particle (7.41) compared to that of a classical particle (7.23) (with relativistic corrections ignored). Relativistic corrections result in orbits which are reduced in size and more eccentric when compared to classical orbits. A single period is displayed in order to isolate the effect of reduction of the orbit. The effect is exaggerated by the choice of parameters (for purposes of illustration). Relativistic corrections also result in precession, which is not featured in this figure.

which is one-sixth of that derived from the general relativistic description [191, 194] (7.26). In addition, nearly circular orbits are predicted to be more eccentric than Keplerian orbits; (7.41) predicts a difference of $\delta e \approx \frac{1}{2}\epsilon^2 e$, which is one-third of that derived from the general relativistic description (7.30). The relativistic effect of reduction in the overall size of the orbit is illustrated in Fig. 22. It should be noted that, although the angular momentum is defined differently in the description which considers effects due only to special relativity, it is taken to be a parameter in the

resulting orbital equation (7.41), so that comparisons with the Newtonian and general relativistic descriptions may be made for a fixed value of angular momentum. This approximation scheme yields a closed-form solution that exhibits several features of relativistic orbits at once. The resulting equation of orbit (7.41) serves as a point for comparison to that derived for a Lorentz-violating particle in the next section.

3. Lorentz Violation

As discussed earlier, a classical Lorentz-violating particle under the influence of a central gravitational force is described by the Lagrangian,

$$\mathcal{L} = -\gamma^{-1}mc^2 - \gamma_0 m v_0 v - U(r). \tag{7.42}$$

The resulting equation of motion is

$$-\frac{\partial U}{\partial r} = km\ddot{r} + \dot{k}m\dot{r} - kr\dot{\varphi}^2 \tag{7.43}$$

$$L = kmr^2\dot{\varphi}, \tag{7.44}$$

where $k \equiv (\gamma v - \gamma_0 v_0)/v$. In order to derive an equation for the orbit, $r(\varphi)$, the following quantities are calculated:

$$\frac{\mathrm{d}^2}{\mathrm{d}\varphi^2}\left(\frac{1}{r}\right) = -\frac{m}{L^2}kr^2(m\ddot{r} + \dot{k}m\dot{r}) \tag{7.45}$$

$$\frac{L^2}{m}k^{-1}r^{-3} = kmr\dot{\varphi}^2, \tag{7.46}$$

wherein (7.44) is used repeatedly. The right-hand sides of these expressions are recognized as parts of the equation of motion (7.43), which may now be expressed as

$$\frac{\mathrm{d}^2}{\mathrm{d}\varphi^2}\left(\frac{\alpha}{r}\right) + \frac{\alpha}{r} = k. \tag{7.47}$$

In the limit that both $v/c \ll 1$ and $v_0/v \ll 1$, k may be expressed as a Taylor series:

$$k = 1 + \frac{1}{2}\left(\frac{v}{c}\right)^2 - \frac{v_0}{v} + \frac{1}{8}\left(\frac{v}{c}\right)^4 - \frac{1}{2}\left(\frac{v}{c}\right)^2\left(\frac{v_0}{v}\right)^3 + \cdots . \tag{7.48}$$

The effects of Lorentz violation are isolated by taking

$$k \approx 1 - \frac{v_0}{v} \tag{7.49}$$

so that:

$$\frac{\mathrm{d}^2}{\mathrm{d}\varphi^2}\left(\frac{\alpha}{r}\right) + \frac{\alpha}{r} \approx 1 - \frac{v_0}{v}. \tag{7.50}$$

The conic sections of the Newtonian description (7.23) are recovered in the limit $v_0 \to 0$, so that the term v_0/v may be treated as a small correction to the Newtonian description. (Recall that $v \geq v_0$ so that (7.50) is well-behaved.) Having near-circular orbits in mind, a zeroth-order correction to the Newtonian description is to determine v_0/v from the classical virial theorem: $-\frac{1}{2}U \approx T$, where $T \equiv (\gamma - \gamma_0)mc^2$. Then,

$$\frac{GMm/c^2}{2r} = \tfrac{1}{2}mv^2/c^2 - \tfrac{1}{2}mv_0^2/c^2 + \cdots , \tag{7.51}$$

or

$$\frac{v_0}{v_\alpha}\left(\frac{\alpha}{r}\right)^{-1/2} \approx \frac{v_0}{v}. \tag{7.52}$$

(Recall the definitions of α and v_α after (7.22).) The orbital equation (7.43) may now be expressed as

$$\frac{\mathrm{d}^2}{\mathrm{d}\varphi^2}\left(\frac{\alpha}{r}\right) + \frac{\alpha}{r} \approx 1 - \frac{v_0}{v_\alpha}\left(\frac{\alpha}{r}\right)^{-1/2}, \tag{7.53}$$

Apply the change of variable $1/\rho \equiv \alpha/r - 1$ so that (7.53) may be expressed as

$$\frac{\mathrm{d}^2}{\mathrm{d}\varphi^2}\left(\frac{1}{\rho}\right) + \frac{1}{\rho} \approx -\frac{v_0}{v_\alpha}\left(1 + \frac{1}{\rho}\right)^{-1/2}. \tag{7.54}$$

Assume that $1/\rho \ll 1$ so that $(1+1/\rho)^{-1/2} \approx 1 - \frac{1}{2}(1/\rho)$; This is equivalent to restricting the solutions to near-circular orbits. Then

$$\frac{\mathrm{d}^2}{\mathrm{d}\varphi^2}\left(\frac{1}{\rho}\right) + \kappa_0^2\left(\frac{1}{\rho}\right) \approx -\frac{v_0}{v_\alpha}, \tag{7.55}$$

where $\kappa_0^2 \equiv 1 - \frac{1}{2}(v_0/v_\alpha)$. The solution is a precessing ellipse:

$$\frac{\alpha}{r} \approx 1 - \epsilon_0 + (1 + \tfrac{1}{2}\epsilon_0)e\cos(1 - \tfrac{1}{4}\epsilon_0)\varphi, \tag{7.56}$$

where $\epsilon_0 \equiv v_0/v_\alpha$ and e is defined after (7.23). Corrections to the total energy are of order $(v_0/c)^2$ so that e is approximately the same as that for a classical orbit. The approximation preceding (7.55) is now seen to be equivalent to the assumption of very small eccentricity: $e \ll 1$. The solution (7.56) can be verified by direct substitution into (7.53), keeping only terms up to orders ϵ_0, e, and $\epsilon_0 e$. The resulting orbit (7.56) is predicted to be larger in size and more eccentric than classical Keplerian orbits. In addition, forward apsidal precession per revolution is predicted to be $\delta\varphi \approx \frac{1}{4}\epsilon_0(2\pi)$.

The combined effects due to Lorentz violation and relativistic speeds are accounted for by keeping the first three terms of the Taylor series (7.48):

$$k \approx 1 + \frac{1}{2}\left(\frac{v}{c}\right)^2 - \frac{v_0}{v}. \tag{7.57}$$

Then (7.47) becomes

$$\frac{\mathrm{d}^2}{\mathrm{d}\varphi^2}\left(\frac{\alpha}{r}\right) + \frac{\alpha}{r} \approx 1 + \frac{1}{2}\left(\frac{v}{c}\right)^2 - \frac{v_0}{v}. \tag{7.58}$$

The velocity dependence is removed using both (7.38) and (7.52), so that the orbital equation (7.58) may now be expressed as

$$\frac{\mathrm{d}^2}{\mathrm{d}\varphi^2}\left(\frac{\alpha}{r}\right) + \bar{\kappa}^2\left(\frac{\alpha}{r}\right) \approx 1 - \epsilon_0\left(\frac{\alpha}{r}\right)^{-1/2}, \tag{7.59}$$

where $\bar{\kappa}^2 \equiv 1 - \frac{1}{2}\epsilon^2$, $\epsilon \equiv v_\alpha/c$, and $\epsilon_0 \equiv v_0/v_\alpha$. (Recall the definitions of α and

v_α after (7.22).) The orbital equation describing near-circular, classical relativistic orbits (7.39) is recovered in the limit $\epsilon_0 \to 0$ ($v_0 \to 0$). Apply the change of variable $1/\rho \equiv \bar{\kappa}^2(\alpha/r) - 1$ and assume that $(1 + 1/\rho)^{-1/2} \approx 1 - \frac{1}{2}(1/\rho)$. Then

$$\frac{\mathrm{d}^2}{\mathrm{d}\varphi^2}\left(\frac{1}{\rho}\right) + \bar{\kappa}_0^2\left(\frac{1}{\rho}\right) \approx -\epsilon_0, \tag{7.60}$$

where $\bar{\kappa}_0^2 \equiv \bar{\kappa}^2 - \frac{1}{2}\epsilon_0 = 1 - \frac{1}{2}\epsilon^2 - \frac{1}{2}\epsilon_0$. The solution is a precessing ellipse:

$$\frac{\alpha}{r} \approx 1 + \tfrac{1}{2}\epsilon^2 - \epsilon_0 + (1 + \epsilon^2 + \tfrac{1}{2}\epsilon_0)e\cos(1 - \tfrac{1}{4}\epsilon^2 - \tfrac{1}{4}\epsilon_0)\varphi. \tag{7.61}$$

The approximation preceding (7.60) is now seen to be equivalent to the assumption of very small eccentricity: $e \ll 1$. The solution (7.61) can be verified by direct substitution into (7.59), keeping only terms up to orders ϵ^2, ϵ_0, e, $\epsilon^2 e$, and $\epsilon_0 e$. The combined effects of Lorentz violation and relativistic speeds (at fixed angular momentum) may be summarized as follows: (1) The reduction in the overall size of the orbit predicted by relativity is offset by an enlargement of the orbit predicted by Lorentz violation. (2) The increased eccentricity predicted by relativity is augmented by a contribution due to Lorentz violation. (3) The rate of precession predicted by relativity is augmented by a contribution due to Lorentz violation.

C. Observational Tests of Lorentz-Violation

It is interesting to consider a circular orbit for a LVDM particle in order to quantify the effects of Lorentz violation. A nonrelativisitic Lorentz-violating particle in circular orbit is described by (7.56) with $e = 0$ so that

$$\frac{r}{\alpha} \approx 1 + \frac{v_0}{v_\alpha}. \tag{7.62}$$

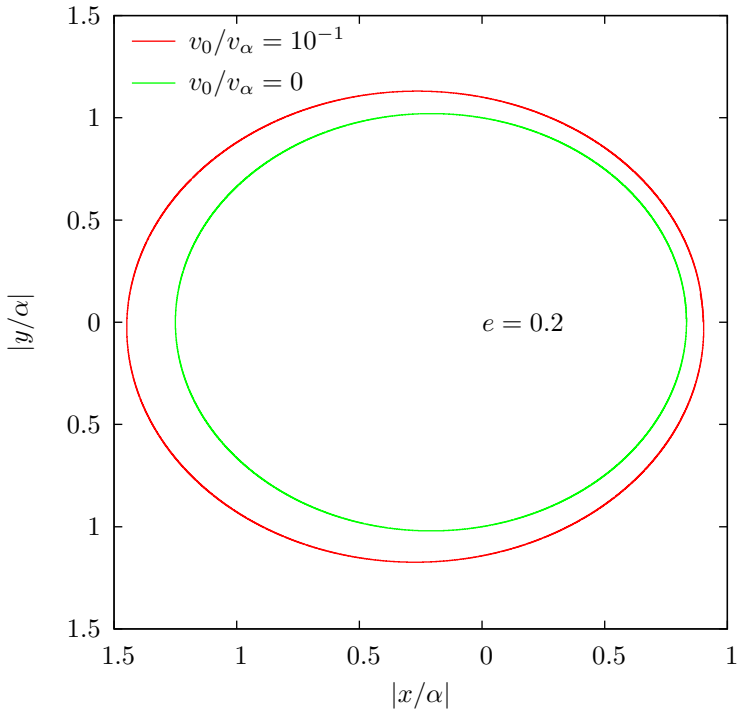

Fig. 23. Orbit of a Lorentz-violating particle (7.56) compared to that of a classical particle (7.23). Small violations of Lorentz invariance result in orbits which are enlarged and more eccentric when compared to classical orbits. A single period is displayed in order to isolate the effect of enlargement of the orbit. The effect is exaggerated by the choice of parameters, for purposes of illustration. Lorentz violation also results in precession, which is not featured in this figure.

A particle orbiting a galaxy of $10^{11} M_\odot$ at radius 100 kpc corresponds to $v_\alpha/c \approx 10^{-4}$ so that effects of Lorentz violation would be dramatic on this scale unless $v_0/c \ll 10^{-4}$. Although this is consistent with constraints derived in Chaps. V and VI, it is unlikely that the these orbital features are observable on this scale via gravitational dynamics.

The effect of enlargement of near-circular orbits – due to Lorentz-violation – is illustrated in Fig. 23, where (7.56) is plotted for a single period. The exaggerated values $e = 0.2$ and $v_0/v_\alpha = 10^{-1}$ are chosen for purposes of illustration. Lorentz violation also results in precession, which is not featured in this figure (since only one period is displayed). These effects might be observable in galactic clusters. For

example, a cluster of galaxies may be considered (as a reasonable approximation) to be composed entirely of dark matter, and each galaxy treated as a dark matter particle. The properties of the orbits of single galaxies in a cluster may be observed and compared to the predictions for Lorentz-violating particles. The effect of enlarged orbits is of order $\delta r \sim \epsilon_0 \alpha = GMv_0/v_\alpha^3$ and may be observable near a massive galaxy cluster. A cluster consisting of 100 giant spiral galaxies may be described by $M \sim 100 \times 10^{12} M_\odot \sim 10^{44}\,\mathrm{kg}$ and $v_\alpha/c \sim 10^{-2}$, so that $\delta r \approx 1\,\mathrm{Mpc} \times v_0/c$. An outlying cluster member galaxy with a larger orbital radius than that predicted by standard classical dynamics could be an indication of a small violation of Lorentz invariance. Equivalently, an outlying cluster member galaxy may have an orbital speed larger than that predicted by classical dynamics. The effect of large eccentricity may also be observed. For example, Bosch et al. [207] find galaxy and cluster substructure eccentricity distributions to be strongly skewed toward high eccentricity. Additionally, the properties of the orbits of field (isolated) binary galaxies may be observed. A binary system with larger separation than predicted by standard classical dynamics could be an indication of a small violation of Lorentz invariance. The total mass of an isolated binary galaxy system is known to be a function of eccentricity [208].

In principle, cluster galaxies are relativistic so that (7.61) applies. It is expected that $\epsilon_0 < \epsilon$, but it is not obvious that $\epsilon_0 < \epsilon^2$. It is possible that effects of Lorentz violation are responsible for an equal part of an observed precession, and that orbits are not as small as those predicted by relativity alone due to the canceling effect of Lorentz violation. For example, taking $\epsilon_0 \sim \epsilon^2$, the combined effects of Lorentz violation and relativistic speeds are orbits that differ in size by $\delta r \sim \frac{1}{2}\epsilon_0 \alpha \sim \frac{1}{2}\epsilon^2 \alpha$, and with twice the rate of precession, when compared to classical Keplerian orbits. This correction is equal in magnitude to that predicted by relativity alone, but the

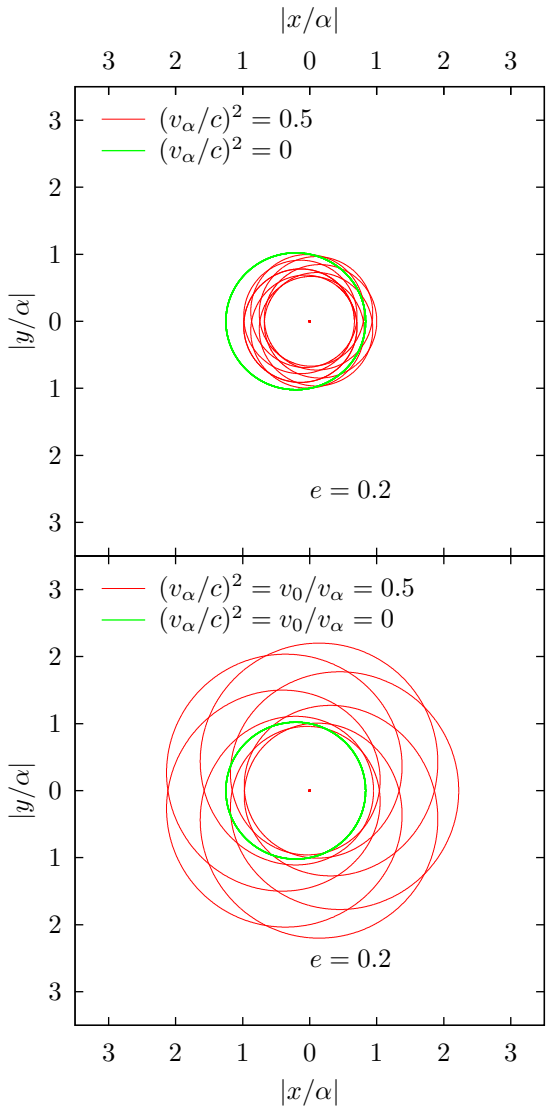

Fig. 24. Orbit of a particle including only relativistic corrections (7.41) (top) compared to that including corrections due to both relativity and Lorentz violation (7.61) (bottom). (The nonprecessing orbit of a classical particle is also included in each figure for reference.) Lorentz violation results in an enlarged, more eccentric orbit when compared to an orbit with relativistic corrections alone. Lorentz violation also results in an orbit with a larger rate of precession than that predicted using relativistic corrections alone. The effects are exaggerated by the choice of parameters, for purposes of illustration.

orbit is predicted to be larger instead of smaller. The correction to the eccentricity is three times that predicted by relativity alone.

Corrections due to both relativity and Lorentz violation are illustrated in Fig. 24. The parameters are chosen to be $\epsilon_0 = \epsilon^2 = 0.5$ and $e = 0.2$. (These parameters are again exaggerated for purposes of illustration.) The top figure displays relativistic corrections alone (7.41), and the bottom figure displays corrections due to both relativity and Lorentz violation (7.61). Corrections due to both relativity and Lorentz violation result in an orbit that is larger and more eccentric, as well as having a larger rate of precession, than that due to relativistic corrections alone. Relativistic corrections alone result in an orbit which is reduced when compared to a classical orbit. The parameters are chosen so that corrections due to relativity and Lorentz violation result in an orbit which is enlarged when compared to a classical orbit.

CHAPTER VIII

CONCLUSIONS

Lorentz-violating dark matter (LVDM), as defined in the present thesis, is dark matter which has a lower limit on its velocity, as indicated in (4.1) and (4.2). As this lower limit v_0 goes to zero, one recovers standard relativistic dynamics. But if v_0 is an appreciable fraction of the speed of light, the binding energy of such a particle in a galaxy becomes substantially smaller than that of standard cold dark matter (CDM). In the limit $v_0 \to c$, where c is the speed of light, the binding energy is zero, and the dynamics is in fact the same as that for a massless particle in standard relativistic dynamics. In this sense, LVDM can thus be regarded as interpolating between CDM and hot dark matter.

However, the detailed studies presented here lead to the conclusion that LVDM does not lead to a solution of the conflict between CDM simulations, which predict a great deal of structure on sub-galactic scales, and the observations, which do not exhibit such structure. The basic reason is that LVDM particles would not be bound in a galaxy unless $v_0/c \ll 10^{-4}$, and for such low values of v_0 the results for LVDM are not much different from those of CDM. These results were determined from a detailed analysis of the binding energy and by constructing an effective potential, which leads to the conclusion that stable orbits are possible only for small values of v_0/c.

On the other hand, the present calculations have provided a substantial amount of insight into the consequences of Lorentz-violating dynamics, as one can see by perusing the results of the preceding chapter. These results were obtained by constructing an effective classical Lagrangian, and they include the following qualitative conclusions:

(1) The effect of Lorentz violation (LV) is to increase the size of the orbit, when

compared to an orbit in standard dynamics. The contribution of LV is thus opposite to that produced by relativistic corrections.

(2) Another effect of Lorentz violation is to increase the eccentricity of the orbit, again when compared to an orbit in standard dynamics. This contribution is in addition to that produced by relativistic corrections.

(3) Still another effect of Lorentz violation is precession of the orbit, which is again in addition to that produced by relativistic corrections.

These effects are discussed quantitatively and in detail in the preceding chapter, and are exhibited in the figures. As discussed near the end of this chapter, the effects would in principle be observable in galactic clusters. For example, if such matter were present in galaxies in large proportions, it would lead to galactic motion that is different from that predicted for standard relativistic matter.

REFERENCES

[1] H. S. Leavitt, Harvard College Obs. Circ. 173 (1912) 1.

[2] H. Shapley, Harvard College Obs. Circ. 280 (1925) 1.

[3] E. P. Hubble, Astrophys. J. 62 (1925) 409.

[4] E. P. Hubble, Astrophys. J. 63 (1926) 236.

[5] A. Einstein, Preuss. Akad. Wiss. Berlin, Sitzber. (1915) 844.

[6] E. P. Hubble, Proc. Nat. Acad. Sci. U.S. 15 (1929) 169.

[7] E. P. Hubble and M. L. Humason, Astrophys. J. 74 (1931) 43.

[8] R. A. Alpher, H. Bethe, and G. Gamow, Phys. Rev. 73 (1948) 803.

[9] A. A. Penzias and R. W. Wilson, Astrophys. J. 142 (1965) 419.

[10] A. Sandage, Astrophys. J. 133 (1961) 355.

[11] R. B. Tully and J. R. Fisher, Astrophys. J. 54 (1961) 661.

[12] A. Dressler, D. Lyndon-Bell, D. Burstein, R. L. Davies, S. M. Faber, R. Terlevich, and G. Wegner, Astrophys. J. 313 (1987) 37.

[13] G. Djorgovski and M. Davies, Astrophys. J. 313 (1987) 59.

[14] I. Jorgensen, M. Franx, and P. Kjaergaard, Mon. Not. R. Astron. Soc. 280 (1996) 167.

[15] D. N. Schramm and M. S. Turner, Rev. Mod. Phys. 70 (1998) 303, astro-ph/9706069.

[16] M. S. Turner, Cosmology 1996, astro-ph/9704024.

[17] A. Kosowsky, M. Kamionkowski, G. Jungman, and D. N. Spergel, Nuc. Phys. B (Proc. Suppl.) 51B (1996) 49.

[18] S. Perlmutter, B. Boyle, P. Bunclarck, D. Carter, W. Couch, S. Deustua, M. Dopita, R. Ellis, A. V. Fillipenko, S. Gabi, K. Glazebrook, G. Goldhaber, A. Goobar, D. Groom, I. Hook, M. Irwin, A. Kim, M. Kim, J. Lee, T. Matheson, R. McMahon, H. Newberg, R. Pain, C. Pennypacker, and I. Small, Nuc. Phys. B (Proc. Suppl.) 51B (1996) 20.

[19] M. Tegmark, D. J. Eisenstein, and W. Hu, in: J. T. Thanh and Y. Giraud-Heraud (Eds.), Fundamental Parameters in Cosmology, Proceedings of the XXXIIIrd Rencontres de Moriond, Éditions Frontiers, 1998, p. 355, astro-ph/9804168.

[20] A. Einstein and W. de Sitter, Proc. N.A.S. 18 (1932) 213.

[21] A. G. Riess, A. V. Filippenko, P. Challis, A. Clocchiatti, A. Diercks, P. M. Garnavich, R. L. Gilliland, C. J. Hogan, S. Jha, R. P. Kirshner, B. Leibundgut, M. M. Phillips, D. Riess, B. P. Schmidt, R. A. Schommer, R. C. Smith, J. Spyromilio, C. Stubbs, N. B. Suntzeff, and J. Tonry, Astron. J. 116 (1998) 1009, astro-ph/9805201.

[22] S. Perlmutter, G. Aldering, G. Goldhaber, R. A. Knop, P. Nugent, P. G. Castro, S. Deustua, S. Fabbro, A. Goobar, D. E. Groom, I. M. Hook, A. G. Kim, M. Y. Kim, J. C. Lee, N. J. Nunes, R. Pain, C. R. Pennypacker, R. Quimby, C. Lidman, R. S. Ellis, M. Irwin, R. G. McMahon, P. Ruiz-Lapuente, N. Walton, B. Schaefer, B. J. Boyle, A. V. Filippenko, T. Matheson, A. S. Fruchter, N.

Panagia, H. J. M. Newberg, and W. J. Couch, Astrophys. J. 517 (1999) 565, astro-ph/9812133.

[23] E. W. Kolb and M. S. Turner, The Early Universe, Addison-Wesley, Redwood City, California, 1990.

[24] P. J. E. Peebles, Principles of Physical Cosmology, Princeton University Press, Princeton, 1993.

[25] S. Weinberg, Gravitation and Cosmology, Wiley, New York, 1972.

[26] M. S. Turner, in: N. Turok (Ed.), Critical Dialogues In Cosmology, World Scientific, 1997, astro-ph/9703161.

[27] M. S. Turner, in: M. Livio, M. Donahue, and N. Panagia (Eds.), The Extragalactic Distance Scale, Cambridge University Press, 1997, astro-ph/9703174.

[28] P. J. Steinhardt, Nature 382 (1996) 768.

[29] I. M. Hook, D. A. Howell, G. Aldering, R. Amanullah, M. S. Burns, A. Conley, S. E. Deustua, R. Ellis, S. Fabbro, V. Fadeyev, G. Folatelli, G. Garavini, R. Gibbons, G. Goldhaber, A. Goobar, D. E. Groom, A. G. Kim, R. A. Knop, M. Kowalski, C. Lidman, S. Nobili, P. E. Nugent, R. Pain, C. R. Pennypacker, S. Perlmutter, P. Ruiz-Lapuente, G. Sainton, B. E. Schaefer, E. Smith, A. L. Spadafora, V. Stanishev, R. C. Thomas, N. A. Walton, L. Wang, and W. M. Wood-Vasey, Astron. J. 130 (2005) 2788.

[30] K. Sharon, A. Gal-Yam, D. Maoz, M. Donahue, H. Ebeling, R. Ellis, A. Filippenko, R. Foley, W. Freedman, R. Kirshner, J.-P. Kneib, T. Matheson, J. Mulchaey, V. Sarajedini, and M. Voit, to be published in: L. Burderi, et al.

(Eds.), The Multicoloured Landscape of Compact Objects and their Explosive Origins, AIP, 2006, astro-ph/0611920.

[31] V. Trimble, Publ. Astron. Soc. Pac. 108 (1996) 1073.

[32] J. D. Fernie, Publ. Astron. Soc. Pac. 81 (1969) 707.

[33] R. C. Kennicutt, W. L. Freedman, and J. R. Mould, Astron. J. 110 (1995) 1476.

[34] V. Trimble, Nuc. Phys. B (Proc. Suppl.) 51B (1996) 5.

[35] V. Trimble, in: M. Livio, M. Donahue, N. Panagia (Eds.), The Extragalactic Distance Scale, Cambridge University press, Cambridge, 1997, p. 313.

[36] R. Tripp, Astron. & Astrophys. 331 (1998) 815.

[37] W. L. Freedman, B. F. Madore, and R. C. Kennicutt, in: M. Livio, M. Donahue, N. Panagia (Eds.), The Extragalactic Distance Scale, Cambridge University press, Cambridge, 1997, p. 171.

[38] A. G. Kim, S. Gabi, G. Goldhaber, D. E. Groom, I. M. Hook, M. Y. Kim, J. C. Lee, C. R. Pennypacker, S. Perlmutter, I. A. Small, A. Goobar, R. Pain, R. S. Ellis, R. G. McMahon, B. J. Boyle, P. S. Bunclark, D. Carter, M. J. Irwin, K. Glazebrook, H. J. M. Newberg, A. V. Filippenko, T. Matheson, M. Dopita, and W. J. Couch (The Supernova Cosmology Project), Astrophys. J. 476 (1997) L63.

[39] A. Saha, A. Sandage, L. Labhardt, G. A. Tammann, F. D. Macchetto, and N. Panagia, Astrophys. J. 486 (1997) 1.

[40] R. Tripp, Astron. & Astrophys. 325 (1997) 871.

[41] D. Branch, W. Romanishin, and E. Baron, Astrophys. J. 465 (1996) 73.

[42] M. Hamuy, M. M. Phillips, N. B. Suntzeff, R. A. Schommer, J. Maza, and R. Avilés, Astron. J. 112 (1996) 2398.

[43] A. G. Riess, W. H. Press, and R. P. Kirshner, Astrophys. J. 473 (1996) 88.

[44] B. E. Schaefer, Astrophys. J. 460 (1996) L19.

[45] D. Branch, Annu. Rev. Astron. Astrophys. 36 (1998) 17, astro-ph/9801065.

[46] P. Höflich and A. Khokhlov, Astrophys. J. 457 (1996) 500.

[47] G. A. Tammann, in: T. Piran (Ed.), Proceedings of the 8^{th} Marcel Grossman Symposium, World Scientific, Singapore, 1998, astro-ph/9805013.

[48] W. L. Freedman, J. R. Mould, R. C. Kennicutt, Jr., and B. F. Madore, IAU Symposium 183, astro-ph/9801080.

[49] W. L. Freedman, B. F. Madore, B. K. Gibson, L. Ferrarese, D. D. Kelson, S. Sakai, J. R. Mould, R. C. Kennicutt, H. C. Ford, J. A. Graham, J. P. Huchra, S. M. G. Hughes, G. D. Illingworth, L. M. Macri, and P. B. Stetson, Astrophys. J. 553 (2001) 47.

[50] W. L. Freedman, Phys. Rep. 333 (2000) 13, astro-ph/9909076.

[51] L. Ferrarese, B. K. Gibson, D. D. Kelson, S. Sakai, J. R. Mould, W. L. Freedman, R. C. Kennicutt, Jr., H. C. Ford, J. A. Graham, J. Huchra, S. M. Hughes, G. D. Illingworth, L. Macri, B. F. Madore, K. Sebo, N. A. Silbermann, and P. B. Stetson, The Hubble Constant from the HST Key Project on the Extragalactic Distance Scale, astro-ph/9909134.

[52] D. N. Spergel, R. Bean, O. Dore', M. R. Nolta, C. L. Bennett, G. Hinshaw, N. Jarosik, E. Komatsu, L. Page, H. V. Peiris, L. Verde, C. Barnes, M. Halpern, R. S. Hill, A. Kogut, M. Limon, S. S. Meyer, N. Odegard, G. S. Tucker, J. L. Weiland, E. Wollack, and E. L. Wright, Wilkinson Microwave Anisotropy Probe (WMAP) Three Year Results: Implications for Cosmology, astro-ph/0603449.

[53] D. N. Spergel, L. Verde, H. V. Peiris, E. Komatsu, M. R. Nolta, C. L. Bennett, M. Halpern, G. Hinshaw, N. Jarosik, A. Kogut, M. Limon, S. S. Meyer, L. Page, G. S. Tucker, J. L. Weiland, E. Wollack, and E. L. Wright, Astrophys. J. Suppl. 148 (2003) 175, astro-ph/0302209.

[54] P. Schneider, J. Ehlers, and E. E. Falco, Gravitational Lenses, Springer-Verlag, New York, 1992.

[55] S. Refsdal, Mon. Not. R. Astron. Soc. 128 (1964) 307.

[56] S. Refsdal, Mon. Not. R. Astron. Soc. 132 (1966) 101.

[57] D. Walsh, R. F. Carswell, and R. J. Weymann, Nature 279 (1979) 381.

[58] C. R. Keeton, E. E. Falco, C. D. Impey, C. S. Kochanek, J. Lehár, B. A. McLeod, H.-W. Rix, J. A. Muñoz, and C. Y. Peng, Astrophys. J. 542 (2000) 74.

[59] C. S. Kochanek and P. L. Schechter, in: W. L. Freedman (Ed.), Carnegie Observatories Astrophysics Series, Vol. 2: Measuring and Modeling the Universe, Carnegie Observatories, Pasadena, 2003.

[60] V. F. Cardone, S. Capozziello, V. Re, and E. Piedipalumbo, Astron. & Astrophys. 382 (2002) 792.

[61] T. Kundic, E. L. Turner, W. N. Colley, J. R. Gott, III, J. E. Rhoads, Y. Wang, L. E. Bergeron, K. A. Gloria, D. C. Long, S. Malhotra, and J. Wambsganss, Astrophys. J. 482 (1997) 75.

[62] G. Bernstein and P. Fischer, Astron. J. 118 (1999) 14.

[63] K.-H. Chae, Astrophys. J. 524 (1999) 582.

[64] T. Kundic, J. G. Cohen, R. D. Blanford, and L. M. Lubin, Astrophys. J. 114 (1997) 507.

[65] P. L. Schechter, C. D. Bailyn, R. Barr, R. Barvainis, C. M. Becker, G. M. Bernstein, J. P. Blakeslee, S. J. Bus, A. Dressler, E. E. Falco, R. A. Fesen, P. Fischer, K. Gebhardt, D. Harmer, J. N. Hewitt, J. Hjorth, T. Hurt, A. O. Jaunsen, M. Mateo, D. Mehlert, D. O. Richstone, L. S. Sparke, J. R. Thorstensen, J. L. Tonry, G. Wegner, D. W. Willmarth, and G. Worthey, Astrophys. J. 475 (1997) L85.

[66] C. R. Keeton and C. S. Kochanek, Astrophys. J. 487 (1997) 42.

[67] S. Nair, in: C. S. Kochanek and N. Hewitt (Eds.), Astrophysical Applications of Gravitational Lensing, Kluwer Academic Publishers, Dordrecht, Netherlands, 1996, p. 197.

[68] T. York, N. Jackson, I. W. A. Browne, O. Wucknitz, and J. E. Skelton, Astrophys. J. 572 (2002) L11.

[69] J. Hjorth, I. Burud, A. O. Jaunsen, P. L. Schechter, J.-P. Kneib, M. I. Andersen, H. Korhonen, J. W. Clasen, A. A. Kaas, R. Østensen, J. Pelt, and F. P. Pijpers, Astrophys. J. 572 (2002) L11.

[70] C. S. Kochanek, Gravitational Lenses, the Distance Ladder and the Hubble Constant: A New Dark Matter Problem, astro-ph/0204043.

[71] C. D. Fassnacht, E. Xanthopoulos, L. V. E. Koopmans, and D. Rusin, Astrophys. J. 581 (2002) 823.

[72] P. Jakobsson, J. Hjorth, I. Burud, G. Letawe, C. Lidman, and F. Courbin, Astron. Astrophys. 431 (2005) 103, astro-ph/0409444.

[73] CASTLeS website: `http://cfa-www.harvard.edu/glensdata`.

[74] A. Eigenbrod, F. Courbin, C. Vuissoz, G. Meylan, P. Saha, and S. Dye, Astron. Astrophys. 436 (2005) 25.

[75] P. Saha, F. Courbin, D. Sluse, S. Dye, and G. Meylan, COSMOGRAIL: the COSmological MOnitoring of GRAvItational Lenses IV. Models of Prospective Time-Delay Lenses, astro-ph/0601370.

[76] C. S. Kochanek, N. D. Morgan, E. E. Falco, B. A. McLeod, J. N Winn, J. Dembicky, and B. Ketzeback, Astrophys. J. 640 (2006) 47, astro-ph/0508070.

[77] B. M. Dobke and L. J. King, Astron. & Astrophys. 460 (2006) 647, astro-ph/0609293.

[78] D. B. Guenther and P. Demarque, Astrophys. J. 484 (1997) 937.

[79] S. K. Leggett, M. T. Ruiz, and P. Bergeron, Astrophys. J. 497 (1998) 294.

[80] T. D. Oswalt, J. A. Smith, M. A. Wood, and P. M. Hintzen, Nature 382 (1996) 692.

[81] B. Chaboyer, P. Demarque, P. J. Kernan, and L. M. Krauss, Astrophys. J. 494 (1998) 96, astro-ph/9706128.

[82] R. G. Gratton, F. F. Pecci, E. Carretta, G. Clementini, C. E. Corsi, and M. Lattanzi, Astrophys. J. 491 (1997) 749.

[83] F. Grundahl, D. A. Vandenberg, and M. I. Andersen, Astrophys. J. Lett. 500 (1998) L179, astro-ph/9806081.

[84] J. W. Truran, in: M. Livio, M. Donahue, and N. Panagia (Eds.), The Extragalactic Distance Scale, Cambridge University Press, Cambridge, 1997, p. 18.

[85] J. J. Cowan, A. McWilliam, C. Sneden, and D. L. Burris, Astrophys. J. 480 (1997) 246.

[86] L. Z. Fang, T. Kiang, F. H. Cheng, and F. X. Hu, Q. Jl. Astr. Soc. 23 (1982) 363.

[87] S. Perlmutter, C. R. Pennypacker, G. Goldhaber, A. Goobar, R. A. Muller, H. J. M. Newberg, J. Desai, A. G. Kim, M. Y. Kim, I. A. Small, B. J. Boyle, C. S. Crawford, R. G. McMahon, P. S. Bunclark, D. Carter, M. J. Irwin, R. J. Terlevich, R. S. Ellis, K. Glazebrook, W. J. Couch, J. R. Mould, T. A. Small, and R. G. Abraham, Astrophys. J. 440 (1995) L41.

[88] P. Schuecker, H. A. Ott, W. C. Seitter, R. Ungruhe, H. W. Duerbeck, B. Cunow, G. Spiekermann, and R. Duemmler, Astrophys. J. 496 (1998) 635.

[89] M. G. Park and J. R. Gott, III, Astrophys. J. 489 (1997) 476.

[90] U. L. Pen, New Astron. 2 (1997) 309.

[91] A. H. Guth, Phys. Rev. D 23 (1981) 347.

[92] R. G. Carlberg, H. K. C. Yee, E. Ellingson, S. L. Morris, H. Lin, M. Sawicki, D. Patton, G. Wirth, R. Abraham, P. Gravel, C. J. Pritchet, T. Smecker-Hane, D. Schade, F. D. A. Hartwick, J. E. Hesser, J. B. Hutchings, and J. B. Oke, in: J. T. Thanh and Y. Giraud-Heraud (Eds.), Fundamental Parameters in Cosmology, Proceedings of the XXXIIIrd Rencontres de Moriond, Éditions Frontiers, 1998, p. 279, astro-ph/9804312.

[93] G. Efstathiou, S. L. Bridle, A. N. Lasenby, M. P. Hobson, and R. S. Ellis, Mon. Not. R. Astron. Soc. 303 (1998) L47, astro-ph/9812226.

[94] S. Cole, W. J. Percival, J. A. Peacock, P. Norberg, C. M. Baugh, C. S. Frenk, I. Baldry, J. Bland-Hawthorn, T. Bridges, R. Cannon, M. Colless, C. Collins, W. Couch, N. J. G. Cross, G. Dalton, V. R. Eke, R. De Propris, S. P. Driver, G. Efstathiou, R. S. Ellis, K. Glazebrook, C. Jackson, A. Jenkins, O. Lahav, I. Lewis, S. Lumsden, S. Maddox, D. Madgwick, B. A. Peterson, W. Sutherland, and K. Taylor, Mon. Not. R. Astron. Soc. 362 (2005) 505, astro-ph/0501174.

[95] M. Chiba and Y. Yoshii, Astrophys. J. 510 (1998) 42, astro-ph/9808321.

[96] C. S. Kochanek, Astrophys. J. 466 (1996) 638.

[97] M. Tegmark, M. A. Strauss, M. R. Blanton, K. Abazajian,S. Dodelson, H. Sandvik, X. Wang, D. H. Weinberg, I. Zehavi, N. A. Bahcall, F. Hoyle, A. Berlind, T. Budavari, A. Connolly, D. J. Eisenstein, D. Finkbeiner, J. A. Frieman, J. E. Gunn, L. Hui, B. Jain, D. Johnston, S. Kent, H. Lin, R.Nakajima, A. Pope, R. Scranton, U. Seljak, R. K. Sheth, A. Stebbins, A. S. Szalay, I. Szapudi, J. Annis, J. Brinkmann, S. Burles, F. J. Castander, I. Csabai, J. Loveday, M. Doi, M. Fukugita, B. Gillespie, G. Hennessy, D. W. Hogg, Ž. Ivezić, G. R. Knapp, D. Q. Lamb, B. C. Lee, R. H. Lupton, T. A. McKay, P.

Kunszt, J. A. Munn, L. O'Connell, J. Peoples, J. R. Pier, M. Richmond, C. Rockosi, D. P. Schneider, C. Stoughton, D. L. Tucker, D. E. vanden Berk, B. Yanny, and D. G. York, Phys. Rev. D 69 (2004) 103501, astro-ph/0310723.

[98] M. Bartelmann, in: A. Weiss, G. Raffelt, W. Hillebarndt, F. von Feilitzsch, and T. Buchert, Astro-Particle Physics, 1996, p. 193.

[99] M. Kramer, I. H. Stairs, R. N. Manchester, M. A. McLaughlin, A. G. Lyne, R. D. Ferdman, M. Burgay, D. R. Lorimer, A. Possenti, N. DAmico, J. M. Sarkissian, G. B. Hobbs, J. E. Reynolds, P. C. C. Freire, and F. Camilo, Science 314 (2006) 97, astro-ph/0609417.

[100] W. Hu, N. Sugiyama, and J. Silk, Nature 386 (1997) 37, astro-ph/9504057.

[101] F. Zwicky, Helv. Phys. Acta 6 (1933) 110.

[102] S. van den Bergh, Publ. Astron. Soc. Pac. 111 (1999) 657.

[103] S. Smith, Astrophys. J. 83 (1936) 23.

[104] E. Hubble, Astrophys. J. 79 (1934) 8.

[105] H. W. Babcock, Lick Obs. Bull. 498 (1939) 41.

[106] G. W. Preston, Publ. Astron. Soc. Pac. 116 (2004) 290.

[107] J. H. Oort, Astrophys. J. 91 (1940) 273.

[108] Y. Sofue and V. Rubin, Annu. Rev. Astron. Astrophys. 39 (2001) 137.

[109] V. C. Ruben and W. K. Ford, Jr., Astrophys. J. 159 (1970) 369.

[110] M. S. Roberts and R. N. Whitehurst, Astrophys. J. 201 (1975) 327.

[111] V. C. Ruben, W. K. Ford, Jr., and N. Thonnard, Astrophys. J. 238 (1980) 471.

[112] V. C. Ruben, D. Burstein, W. K. Ford, Jr., and N. Thonnard, Astrophys. J. 289 (1985) 81.

[113] D. Burstein and V. C. Ruben, Astrophys. J. 297 (1985) 423.

[114] R. H. Dicke, P. J. E. Peebles, P. G. Roll, and D. T. Wilkinson, Astrophys. J. 142 (1965) 414.

[115] G. Gamow, Nature 162 (1948) 680.

[116] R. A. Alpher and R. C. Herman, Nature 162 (1948) 774.

[117] R. A. Alpher and R. C. Herman, Phys. Rev. 75 (1949) 1089.

[118] R. A. Stokes, R. B. Partridge, and D. T. Wilkinson, Phys. Rev. Lett. 19 (1967) 1199.

[119] D. T. Wilkinson, Phys. Rev. Lett. 19 (1967) 1195.

[120] D. T. Wilkinson, Phys. Rev. Lett. 19 (1967) 1360.

[121] R. V. Wagoner, W. A. Fowler, and F. Hoyle, Astrophys. J. 148 (1967) 3.

[122] R. A. Alpher, J. W. Follin, and R. C. Herman, Phys. Rev. 92 (1953) 1347.

[123] P. J. E. Peebles, Phys. Rev. Lett. 16 (1966) 410.

[124] G. Danby, J. M. Gaillard, K. Goulianos, L. M. Lederman, N. B. Mistry, M. Schwartz, and J. Steinberger, Phys. Rev. Lett. 9 (1962) 36.

[125] R. K. Sachs and A. M. Wolfe, Astrophys. J. 147 (1967) 73, astro-ph/0010389.

[126] M. White and W. Hu, Astron. Astrophys. 321 (1997) 8, astro-ph/9609105.

[127] S. D. M. White and M. J. Rees, Mon. Not. R. Astron. Soc. 183 (1978) 341.

[128] V. A. Lyubimov et al., Phys. Lett. B94 (1980) 266.

[129] Ya. B. Zeldovich, J. Einasto, and S. F. Shandarin, Nature 300 (1982) 407.

[130] P. Bode, J. P. Ostriker, and N. Turok, Astrophys. J. 556 (2001) 93, astro-ph/0010389.

[131] S. Colombi, S. Dodelson, and L. M. Widrow, Astrophys. J. 1 (1996) 458, astro-ph/9505029.

[132] A. Kogut, D. N. Spergel, C. Barnes, C. L. Bennett, M. Halpern, G. Hinshaw, N. Jarosik, M. Limon, S. S. Meyer, L. Page, G. S. Tucker, E. Wollack, and E. L. Wright, Astrophys. J. Suppl. 148 (2003) 161, astro-ph/0302213.

[133] N. Yoshida, A. Sokasian, L. Hernquist, and V. Springel, Astrophys. J. Lett. 591 (2003) L1, astro-ph/0303622.

[134] J. F. Navarro, C. S. Frenk, and S. D. M. White, Astrophys. J. 462 (1996) 563, astro-ph/9508025.

[135] J. F. Navarro, C. S. Frenk, and S. D. M. White, Astrophys. J. 490 (1997) 493, astro-ph/9611107.

[136] J. A. Sellwood and A. Kosowsky, in: J. E. Hibbard, M. P. Rupen, and J. H. van Gorkom (Eds.), Gas and Galaxy Evolution, ASP Conference Series Vol. 240, 2001, astro-ph/0009074.

[137] H. Goldberg, Phys. Rev. Lett. 50 (1983) 1419.

[138] J. Ellis, J. S. Hagelin, D. V. Nanopoulos, K. A. Olive, and M. Srednicki, Nucl. Phys. B 238 (1984) 453.

[139] R. Arnowitt and B. Dutta, Proceedings of DARK 2002, Cape Town, South Africa, February, 2002, hep-ph/0204187.

[140] R. W. Hockney and J. W. Eastwood, Computer Simulation Using Particles, McGraw-Hill, New York, 1981.

[141] H. M. P. Couchman, Astrophys. J. 368 (1991) 23.

[142] A. V. Kravtsov, A. Klypin, and A. Khokhlov, Astrophys. J. Suppl. 111 (1997) 73, astro-ph/9701195.

[143] B. Moore, Nature 370 (1994) 629, astro-ph/9402009.

[144] R. A. Flores and J. R. Primack, Astrophys. J. 427 (1994) L1, astro-ph/9402004.

[145] G. Kauffmann, S. D. M. White, and B. Guiderdoni, Mon. Not. R. Astron. Soc. 264 (1993) 201.

[146] R. E. Allen and S. Yokoo, Nuclear Physics B (Proc. Suppl.) 134 (2004) 139.

[147] R. E. Allen, Int. J. Mod. Phys. A 12 (1997) 2385, hep-th/9612041.

[148] S. Coleman and S. L. Glashow, Phys. Lett. B 405 (1997) 249; Phys. Rev. D 59 (1999) 116008, hep-ph/9812418.

[149] R. Bluhm, V. A. Kostelecký, and N. Russell, Phys. Rev. D 57 (1998) 3932, hep-ph/9809543.

[150] D. Colladay and V. A. Kostelecký, Phys. Rev. D 58 (1998) 116002, hep-ph/9809521.

[151] D. F. Phillips, M. A. Humphrey, E. M. Mattison, R. E. Stoner, R. F. C. Vessot, and R. L. Walsworth, Phys. Rev. D 63 (2001) 111101, physics/0008230.

[152] V. W. Hughes, M. G. Perdekamp, D. Kawall, W. Liu, K. Jungmann, and G. zu Putlitz, Phys. Rev. Lett. 87 (2001) 111804, hep-ex/0106103.

[153] P. Wolf, S. Bize, A. Clairon, A. N. Luiten, G. Santarelli, and M. E. Tobar, Phys. Rev. Lett. 90 (2003) 060402, gr-qc/0210049.

[154] J. A. Lipa, J. A. Nissen, S. Wang, D. A. Stricker, and D. Avaloff, Phys. Rev. Lett. 90 (2003) 060403, physics/0302093.

[155] V. A. Kostelecký and C. Lane, Phys. Rev. D 60 (1999) 116010, hep-ph/9908504.

[156] R. Bluhm, V. A. Kostelecký, and C. Lane, Phys. Rev. Lett. 84 (2000) 1098, hep-ph/9912451.

[157] R. Bluhm and V. A. Kostelecký, Phys. Rev. Lett. 84 (2000) 1381, hep-ph/9912542.

[158] D. Bear, R. E. Stoner, R. L. Walsworth, V. A. Kostelecký, and C. Lane, Phys. Rev. Lett. 85 (2000) 5038, physics/0007049.

[159] V. A. Kostelecký, Phys. Rev. D 64 (2001) 076001, hep-ph/0104120.

[160] R. Bluhm, Theoretical Analysis of CPT and Lorentz Tests in Penning Traps, hep-ph/9904508; Probing the Planck Scale in Low-Energy Atomic Physics, hep-ph/0111323.

[161] R. Bluhm, V. A. Kostelecký, C. Lane, and N. Russell, Phys. Rev. Lett. 88 (2002) 090801, hep-ph/0111141.

[162] V. A. Kostelecký and M. Mewes, Phys. Rev. D 66 (2002) 056005, hep-ph/0205211.

[163] R. Bluhm, V. A. Kostelecký, C. Lane, and N. Russell, Phys. Rev. D 68 (2003) 125008, hep-ph/0306190.

[164] N. Russell, CPT and Lorentz Tests with Clocks in Space, hep-ph/0111320; Space-Based Searches for Lorentz and CPT Violation, hep-ph/0208065.

[165] G. Amelino-Camelia, Gen. Rel. Grav. 36 (2004) 539, astro-ph/0309174; Phys. Rev. D 62 (2000) 024015, gr-qc/9903080.

[166] V. A. Kostelecký and M. Mewes, Phys. Rev. Lett. 87 (2001) 251304, hep-ph/0111026.

[167] T. Jacobson, S. Liberati, and D. Mattingly, Phys. Rev. D 67 (2003) 124011, hep-ph/0209264; Nature 424 (2003) 1019, astro-ph/0212190.

[168] T. Jacobson, S. Liberati, D. Mattingly, and F. W. Stecker, New limits on Planck scale Lorentz violation in QED, astro-ph/0309681.

[169] F. W. Stecker and S. L. Glashow, Astropart. Phys. 16 (2001) 97, astro-ph/0102226.

[170] F. W. Stecker, Probing Supersymmetry with Neutral Current Scattering Experiments, astro-ph/0309027.

[171] G. Amelino-Camelia, J. Ellis, N. E. Mavromatos, D. V. Nanopoulos, and S. Sarkar, Nature 393 (1998) 763.

[172] B. Altschul, Phys. Rev. Lett. 98 (2007) 041603, hep-th/0609030.

[173] V. A. Kostelecký, Recent results in Lorentz and CPT tests, hep-ph/0005280.

[174] R. E. Allen, to be published.

[175] R. E. Allen, in: H. V. Klapdor-Kleingrothaus, Proceedings of Beyond the Desert 2002, IOP, London, 2003, hep-th/0008032.

[176] R. E. Allen, in: H. V. Klapdor-Kleingrothaus, Proceedings of Beyond the Desert 2003, hep-th/0310039.

[177] M. E. Peskin and D. V. Schroeder, Introduction to Quantum Field Theory, Addison-Wesley, Reading, Massachusetts, 1995, p. 44.

[178] P. Ramond, Field Theory: A Modern Primer, Addison-Wesley, Redwood City, California, 1990, pp. 16–20.

[179] G. G. Ross, Grand Unified Theories, Benjamin, Menlo Park, 1984.

[180] K. Greisen, Phys. Rev. Lett. 16 (1966) 748; G. T. Zatsepin and V. A. Kuz'min, JETP Lett. 41 (1966) 78; Pisma Zh. Eksp. Teor. Fiz. 4 (1966) 114.

[181] M. Nagano and A. A. Watson, Rev. Mod. Phys. 72 (2000) 689.

[182] P. Bhattacharjee and G. Sigl, Phys. Rept. 327 (2000) 109.

[183] J. N. Bahcall and E. Waxman, Phys. Lett. B 556 (2003) 1, hep-ph/0206217.

[184] L. Anchordoqui, T. Paul, S. Reucroft, and J. Swain, Ultrahigh Energy Cosmic Rays: The state of the art before the Auger Observatory, hep-ph/0206072.

[185] T. J. Weiler, AIP Conf. Proc. 579 (2001) 58, hep-ph/0103023.

[186] M. S. Berger and V. A. Kostelecký, Phys. Rev. D 65 (2002) 091701, hep-th/0112243.

[187] A. R. Mondragon and R. E. Allen, in: P. H. Frampton (Ed.), Proceedings of PASCOS 2001, Rinton Press, Princeton, 2001, astro-ph/0106296.

[188] R. E. Allen, in: V. A. Kostelecký (Ed.), Proceedings of the Second Meeting on CPT and Lorentz Symmetry, World Scientific, Singapore, 2002, hep-th/0110208.

[189] H. Goldstein, Classical Mechanics, Addison-Wesley, Reading, Massachusetts, 1959.

[190] S. M. Carroll, Lecture Notes on General Relativity, 1997, gr-qc/9712019.

[191] C. W. Misner, K. S. Thorne, and J. A. Wheeler, Gravitation, Freeman, San Francisco, California, 1973.

[192] G. Ovanesyan, Am. J. Phys. 71 (2002) 912.

[193] A. Schild, Am. J. Phys. 28 (1960) 778.

[194] D. Brouwer and G. M. Clemence, in: G. P. Kuiper and B. M. Middlehurst (Eds.), Planets and Satellites, The Solar System Volume III, University of Chicago Press, Chicago, Illinois, 1961.

[195] D. R. Stump, Am. J. Phys. 56 (1988) 1097.

[196] K. Doggett, Am. J. Phys. 59 (1991) 851.

[197] M. Blau, Lecture Notes on General Relativity, 2006, `http://www.unine.ch/phys/string/Lecturenotes.html`.

[198] J. B. Marion and S. T. Thornton, Classical Dynamics of Particles and Systems, Harcourt Brace & Company, 1995.

[199] J. B. Marion, Classical Dynamics of Particles and Systems, Academic Press, New York, 1970.

[200] A. Harvey, Am. J. Phys. 46 (1978) 928.

[201] G. J. Whitrow and G. E. Morduch, in: A. Beer (Ed.), Vistas in Astronomy, Volume 6, 1965, p. 1.

[202] P. C. Peters, Am. J. Phys. 55 (1987) 757.

[203] T. Phipps, Jr., Am. J. Phys. 55 (1987) 758.

[204] T. Phipps, Jr., Am. J. Phys. 54 (1986) 851.

[205] A. Einstein, Annals der Physik 35 (1911) 898.

[206] A. Einstein, A. Beck, and D. Howard, The Collected Papers of Albert Einstein, Volume 3: The Swiss Years: Writings, 1909–1911. (English translation supplement), Princeton University Press, Princeton, New Jersey, 1994.

[207] F. C. Bosch, G. F. Lewis, G. Lake, and J. Stadel, Astrophys. J. 515 (1999) 50, astro-ph/9811229.

[208] R. Chan and S. Junqueira, Astron. & Astrophys. 366 (2001) 418.

APPENDIX A

EXACT NUMERICAL SOLUTIONS TO LVDM ROTATION CURVES

```
program exact_LVDM_rotation_curves

  implicit none

  INTEGER,  PARAMETER :: r8=SELECTED_REAL_KIND(15, 307)

  REAL(r8), PARAMETER :: one=1.0E0_r8, two=2.0E0_r8
  REAL(r8), PARAMETER :: three=3.0E0_r8, four=4.0E0_r8
  REAL(r8), PARAMETER :: five=5.0E0_r8, six=6.0E0_r8
  REAL(r8), PARAMETER :: seven=7.0E0_r8, eight=8.0E0_r8
  REAL(r8), PARAMETER :: nine=9.0E0_r8, ten=1.0E1_r8
  REAL(r8), PARAMETER :: eleven=11.0E0_r8, twelve=12.0E0_r8
  REAL(r8), PARAMETER :: thirteen=13.0E0_r8

  REAL(r8), PARAMETER :: b=2000_r8 ! b = 2m/mbar
  REAL(r8), PARAMETER :: vh=2.25E5_r8, c=3.0E8_r8

  REAL(r8) :: uh2, u0, k, r, rg, u, du, tol, dr
  REAL(r8) :: gamma, gamma0, phibar, d_phi, err_u

      !!!!!!!!!!!!!!!!!!!!!!!!!!!!!!!!!!!!!!!!!!!!!!!!!!!!!!!!!!!

  uh2 = (vh/c)**two
  u0  = one/(one + b**two)**(one/two)
  k   = (one/ten)**three
  tol = one/(ten**two)
  du  = u0/(ten**nine)      ! u-step
  dr  = r + one/ten**three  ! r-step

      !!!!!!!!!!!!!!!!!!!!!!!!!!!!!!!!!!!!!!!!!!!!!!!!!!!!!!!!!!!

  r   = one
  OPEN(unit = 10, file = 'b2E3v2.d', status = "new")

  u = u0
  do while (r <= ten)

    rg = one - one/r + k*(r**two)

    gamma0 = one/sqrt(one-(u0**two))
    gamma  = one/sqrt(one-(u**two))
    phibar = (gamma*u-gamma0*u0)*u/uh2
    d_phi  = abs(rg - phibar) ! error
```

```
      err_u  = d_phi/(u*(two*u-u0))

      do while (err_u > tol)

         u  = u + du

         gamma0 = one/sqrt(one-(u0**two))
         gamma  = one/sqrt(one-(u**two))
         phibar = (gamma*u-gamma0*u0)*u/uh2
         d_phi  = abs(rg - phibar) ! error
         err_u  = d_phi/(u*(two*u-u0))

      end do

      write(10, 120) r, u0, u, rg, phibar, d_phi, err_u
      r  = r + dr

    end do

    close(10)

        !!!!!!!!!!!!!!!!!!!!!!!!!!!!!!!!!!!!!!!!!!!!!!!!!!!!!!!!

  120  format(7E17.8)

end program exact_LVDM_rotation_curves
```

APPENDIX B

APPROXIMATE ANALYTICAL SOLUTIONS TO LVDM ROTATION CURVES

```
program approx_LVDM_rotation_curves

implicit none

  INTEGER,  PARAMETER :: r8=SELECTED_REAL_KIND(15, 307)

  REAL(r8), PARAMETER :: one=1.0E0_r8, two=2.0E0_r8
  REAL(r8), PARAMETER :: three=3.0E0_r8, four=4.0E0_r8
  REAL(r8), PARAMETER :: five=5.0E0_r8, six=6.0E0_r8
  REAL(r8), PARAMETER :: seven=7.0E0_r8, eight=8.0E0_r8
  REAL(r8), PARAMETER :: nine=9.0E0_r8, ten=1.0E1_r8
  REAL(r8), PARAMETER :: eleven=11.0E0_r8, twelve=12.0E0_r8
  REAL(r8), PARAMETER :: thirteen=13.0E0_r8

  REAL(r8), PARAMETER :: b=20000_r8 ! b = 2m/mbar
  REAL(r8), PARAMETER :: vh=2.25E5_r8, c=3.0E8_r8

  REAL(r8) :: uh2, u0, k, r, rg, u, du, er, tol
  REAL(r8) :: phi, phi1, phi2

      !!!!!!!!!!!!!!!!!!!!!!!!!!!!!!!!!!!!!!!!!!!!!!!!!!!!!!!!

  uh2 = (vh/c)**two
  u0  = one/(one + b**two)**(one/two)
  k   = (one/ten)**three
  tol = one/(ten**four)
  du  = u0/(ten**four)      ! u-step

      !!!!!!!!!!!!!!!!!!!!!!!!!!!!!!!!!!!!!!!!!!!!!!!!!!!!!!!!

  r    = ten
  rg   = one - one/r + k*(r**two)
  u    = u0
  phi1 = u0*(u - u0)/uh2
  phi2 = ((u - u0)**two)/uh2
  phi  = phi1 + phi2
  er   = abs((rg - phi)/rg)     ! error

    do while (er > tol)

       u    = u + du
       phi1 = u0*(u - u0)/uh2
       phi2 = ((u - u0)**two)/uh2
```

```
        phi  = phi1 + phi2
        er   = abs((rg - phi)/rg) ! error

    end do

    print 120, u, u0, phi1, phi2, er

      !!!!!!!!!!!!!!!!!!!!!!!!!!!!!!!!!!!!!!!!!!!!!!!!!!!!!!!!

 120  format(5E20.11)

end program approx_LVDM_rotation_curves
```

APPENDIX C

EFFECTIVE POTENTIAL IN CENTRAL MASS MODEL: REMAINING PARAMETER SPACE

Here we investigate the effective potential (6.26) and orbital stability condition (6.29) for the remaining parameter space, defined by taking $1 - 3u_0^2\pi_\varphi^2 < 0$ in (6.27), corresponding to $u_0 > 9.1 \times 10^{-4}$.

In the region for which $1-3u_0^2\pi_\varphi^2 < 0$, we have $u_0 > 9.1\times10^{-4}$, and the condition for a circular orbit (6.27) may be written as

$$\left(3u_0^2\pi_\varphi^2 - 1\right)\frac{r_0}{\ell_\varphi^2/r_\mathrm{s}} - 2u_0\pi_\varphi\left(\frac{r_0}{\ell_\varphi^2/r_\mathrm{s}}\right)^{1/2} + 1 = 0, \tag{C.1}$$

for which there are two solutions,

$$\frac{r_0^\pm}{\ell_\varphi^2/r_\mathrm{s}} = \left(\frac{u_0\pi_\varphi}{3u_0^2\pi_\varphi^2 - 1}\right)^2\left[1 \pm \left(1 - \frac{3u_0^2\pi_\varphi^2 - 1}{u_0^2\pi_\varphi^2}\right)^{1/2}\right]^2. \tag{C.2}$$

The solutions are limited to a narrow parameter space defined by $1/3 < u_0^2\pi_\varphi^2 < 1/2$, corresponding to $9.13 \times 10^{-4} < u_0 < 1.12 \times 10^{-3}$, beyond which the argument of the root in (C.2) becomes negative. The radii of circular orbits, r_0^+ and r_0^-, described by (C.2) are plotted in Fig. 25 for values of $u_0^2\pi_\varphi^2$ within this narrow range. The stability condition (6.29) is evaluated at each value of $r_0^\pm$ obtained from (C.2), and is also plotted in Fig. 25. The solutions r_0^+ (top, red) are found to describe unstable (bottom, red) circular orbits over the entire parameter space. The solutions r_0^- (top, blue) are stable (bottom, blue) over the entire parameter space, and describe circular orbits having radii of the same order of magnitude as that predicted for CDM: $r_0^{\mathrm{CDM}} \approx 4\,\mathrm{kpc}$. For example, $r_0^-(1/3) = 3\,\mathrm{kpc}$, and $r_0^-(1/2) = 8\,\mathrm{kpc}$. (See (C.1) and

(C.2), respectively.) An interesting value of u_0 is that for which $r_0^- = r_0^{\rm CDM}$, and is found from (C.1), assuming $r_0 = \ell_\varphi^2/r_{\rm s}$, to be given by $u_0^2\pi_\varphi^2 = 4/9$, or $u_0 = 1.05\times10^{-3}$.

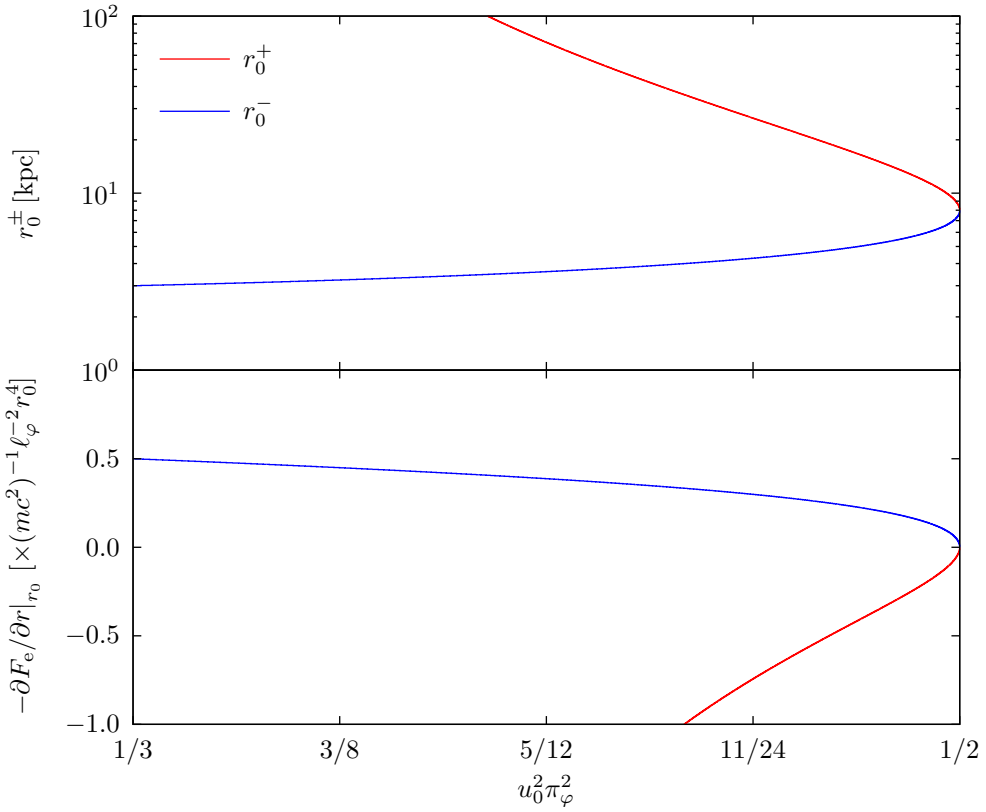

Fig. 25. The radius of a circular orbit (top panel) and the corresponding stability condition (bottom panel) are plotted for values in the narrow range $1/3 < u_0^2\pi_\varphi^2 < 1/2$, corresponding to $9.13\times10^{-4} < u_0 < 1.12\times10^{-3}$. There are two solutions r_0^+ and r_0^- described by (C.2). The stability condition (6.29) is evaluated for each. The solution r_0^+ describes unstable orbits (red). The solutions r_0^- describe stable circular orbits having radii of the same order of magnitude as those predicted for CDM: $r_0^{\rm CDM} \approx 4\,{\rm kpc}$.

We may express the effective potential (6.26) in terms of the parameter $u_0^2\pi_\varphi^2$:

$$(mc^2)^{-1}U_{\rm e} \approx \left(3u_0^2\pi_\varphi^2 - 1\right)\frac{r_{\rm s}}{r} + \pi_\varphi^2\frac{r_{\rm s}^2}{2r^2} - u_0\pi_\varphi^2\frac{4r_{\rm s}^{3/2}}{3r^{3/2}} \tag{C.3}$$

This effective potential is plotted in Fig. 26 for values of u_0 in the narrow range

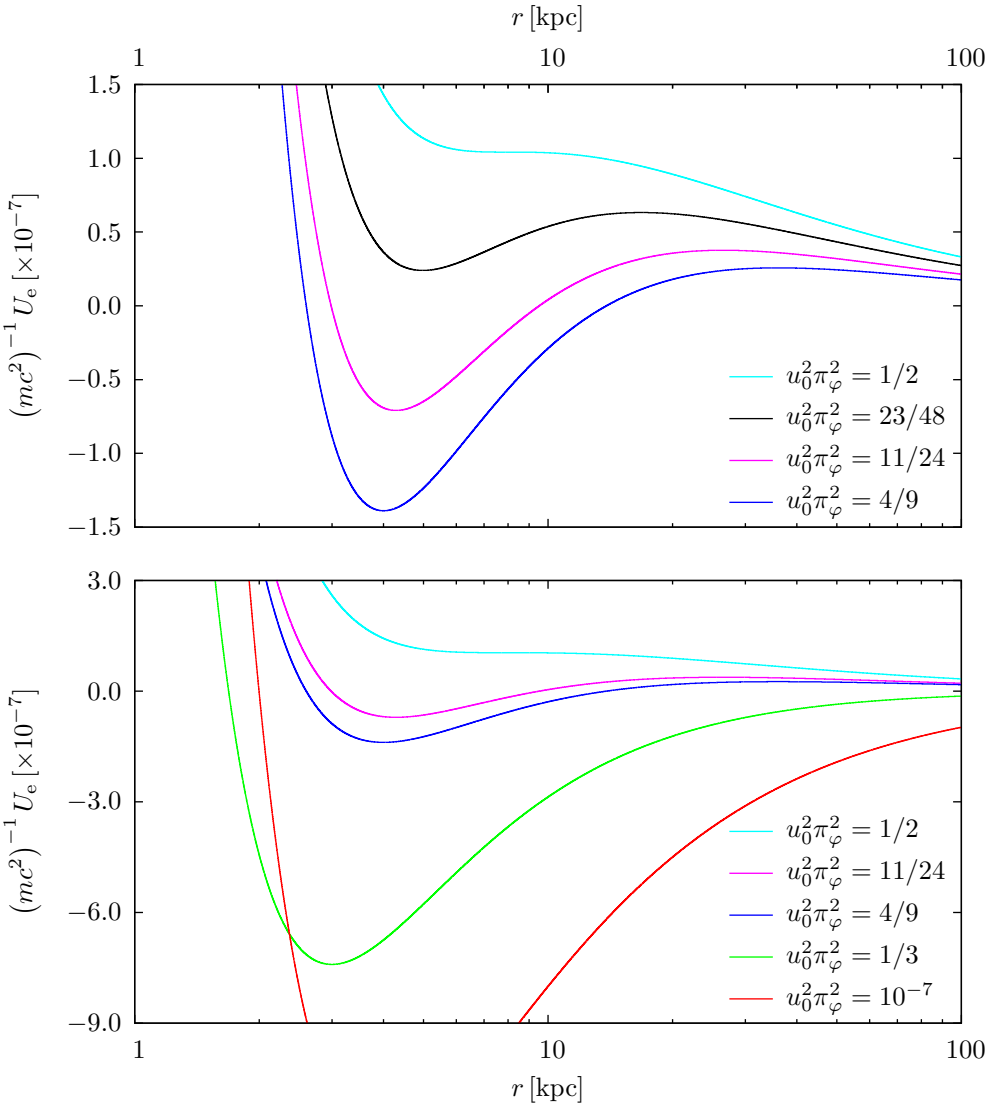

Fig. 26. The LVDM effective potential (C.3) is plotted for several values of u_0 in the narrow range $1/3 < u_0^2\pi_\varphi^2 < 1/2$, again corresponding to $9.13 \times 10^{-4} < u_0 < 1.12 \times 10^{-3}$. Values of $u_0^2\pi_\varphi^2 > 1/3$ result in two circular orbits; one stable, and one unstable. These curves suggest the existence of stable, circular orbits with positive total energy, calling into question the validity of the approximation (6.25), for $u_0^2\pi_\varphi^2 > 1/3$.

$1/3 < u_0^2\pi_\varphi^2 < 1/2$, again corresponding to $9.13 \times 10^{-4} < u_0 < 1.12 \times 10^{-3}$. Values of $u_0^2\pi_\varphi^2 > 1/3$ result in two circular orbits, $r_0^- = 3\,\mathrm{kpc}$ (stable) and $r_0^+ = \infty\,\mathrm{kpc}$ (unstable). As $u_0^2\pi_\varphi^2$ is increased, the two solutions approach each other until $r_0^- = r_0^+ = 8\,\mathrm{kpc}$, when $u_0^2\pi_\varphi^2 = 1/2$. Curves corresponding to $u_0^2\pi_\varphi^2 > 1/3$ suggest the existence of stable, circular orbits with positive total energy, calling into question the validity of the approximation (6.25) for $u_0^2\pi_\varphi^2 > 1/3$. In this approximation closed orbits do not exist for $u_0^2\pi_\varphi^2 > 1/2$.

VITA

Antonio R. Mondragon was born in Redondo Beach, California. He received his B.S. degree in physics from Northwestern State University of Louisiana in 1993. That same year he joined the graduate school at Texas A&M University where he received an M.S. in physics in December 1996. He enrolled in the Ph.D. program in January 1997 and received his Ph.D. degree in May 2007. He can be reached at the Department of Physics, Texas A&M University, College Station, TX 77843-4242.